Thesis Report

Design of a Direct Numerical Simulation of Flow and Heat Transfer in a T-junction

Aniketh Ajay Kumar

Student Number: 5027195
MSc Aerospace Engineering

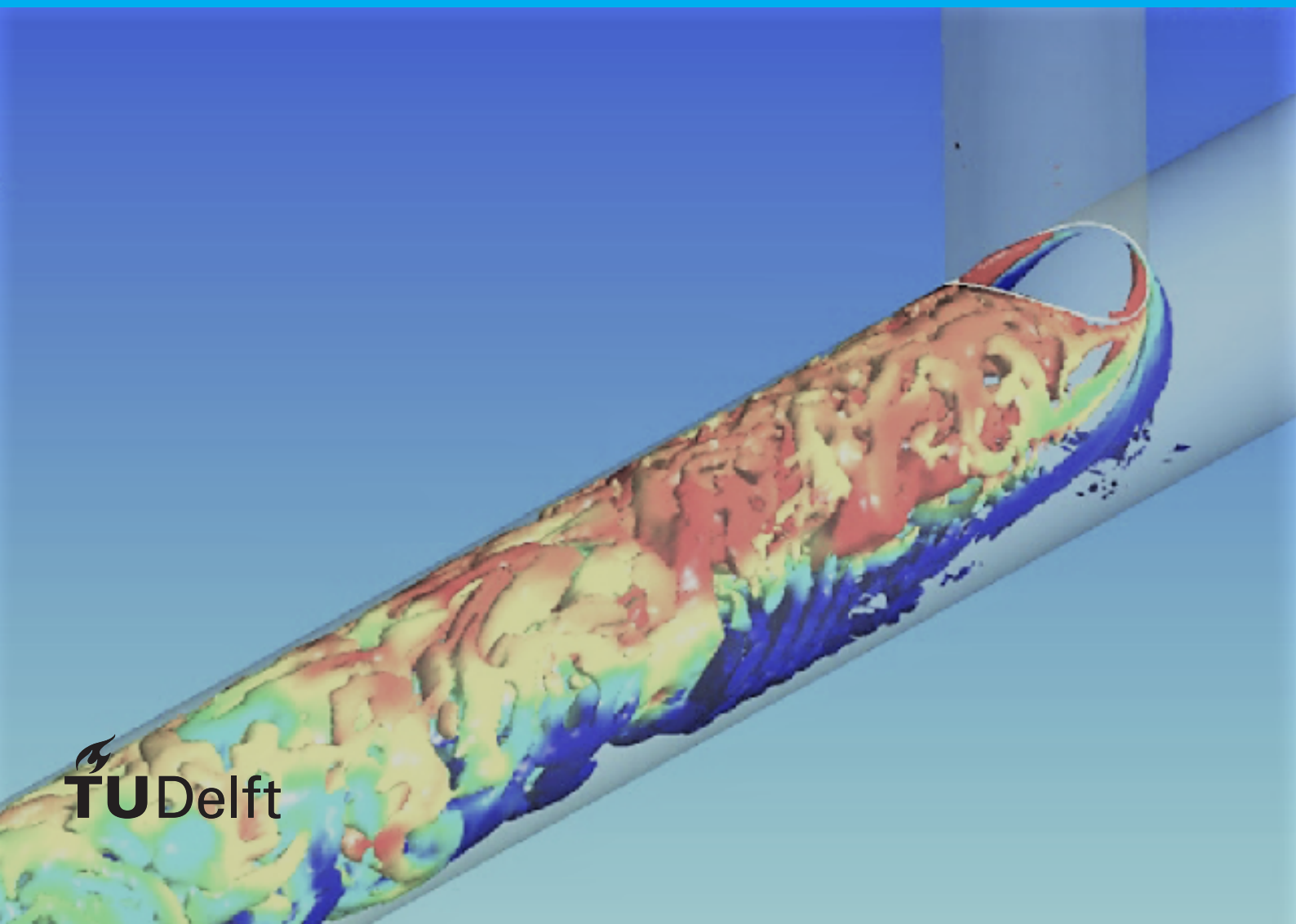

TU Delft

Thesis Report

Design of a Direct Numerical Simulation of Flow and Heat Transfer in a T-junction

by

Aniketh Ajay Kumar

to obtain the degree of Master of Science
at the Delft University of Technology,
to be defended publicly on Tuesday November, 30 2021 at 2:00 PM.

Student number:	5027195	
Project duration:	August 1, 2020 – May 30, 2021	
Thesis Committee:	Prof. Dr. ir. M.I. Gerritsma,	Aerodynamics, LR Faculty, TU Delft
	Dr. A. Mathur,	Nuclear Research and Consultancy Group
	Dr. ir. A.H. van Zuijlen,	Aerodynamics, LR Faculty, TU Delft
	Dr. A. Bombelli,	Air Transport and Operations, LR Faculty, TU Delft

TU Delft

NRG
Nuclear. For life.

Abstract

Several investigations have been undertaken to study the velocity and temperature fields associated with the thermal mixing of fluids, and resulting thermal striping in a T-junction. The T-junction thermal mixing and fatigue phenomenon is a major area of study for the purposes of safety, maintenance and operational life in the nuclear industry, in which fluid mixing occurs in cooling circuits for the nuclear reactor. The existing body of work on T-junctions mainly comprises of experimental references performed at high values of Reynolds numbers. However, these available experimental databases are not sufficient to describe the involved physics in adequate detail, and, due to experimental limitations, accurate data on velocity and temperature fluctuations in regions close to the wall are not accessible. Computational Fluid Dynamics (CFD) can play an important role in predicting such complex flow features. However, predicting complex thermal fatigue phenomena is a challenge for the available momentum and heat flux turbulence models, which also require extensive validation.

It was realised that a comprehensive Direct Numerical Simulation (DNS) of a T-junction was required as a benchmark for validation purposes, but also to better understand the underlying physical phenomena of thermal mixing in the fluid and thermal fatigue in the solid walls. The aim of the thesis is to thus design such a reference DNS experiment of a thermal fatigue scenario calibrated using Reynolds-Averaged Navier-Stokes (RANS) simulations. The feasibility of scaling down the Reynolds number from experimental cases to a computationally-feasible range is investigated. The junction corner shape is also modified to a slightly rounded corner, ensuring that the underlying fundamental physical phenomena of turbulence and thermal mixing flow features were preserved. The pipe lengths of the model were calibrated to ensure there would be no interference of the upstream developing region on the thermal mixing at the junction, and the outlet boundary conditions. A sample proof-of-concept under-resolved DNS (UDNS) case, with high- and low-Prandtl number passive temperature scalars, with iso-temperature, iso-flux and mixed (Robin) wall boundary conditions, is simulated and presented. This proof-of-concept simulation contributes to the finalization of the fully-resolved DNS in computational grid size selection, transient characteristics, computational costs, and additionally, the implementation of the Robin boundary condition in the fully-resolved DNS.

Acknowledgements

This report is the documentation of the work done during my tenure as a master thesis student at Nuclear Research and Consultancy Group (NRG, Petten, The Netherlands), for the fulfilment of the Master Thesis project requirement at TU Delft, The Netherlands. The work done in this thesis would not have been possible without the constant guidance and patience of my project supervisor at NRG, Dr. Akshat Mathur. I would also like to show my appreciation to my TU Delft supervisor, Prof. Dr. ir. Marc Gerritsma, whose support and understanding have helped me immensely. My gratitude also extends to ir. Ed Komen and the entire team of the Reactor Analysis & operational Support (RAS) group at NRG, for making me comfortable at work and for the knowledge and experience I have gained from them this past year.

Under the circumstances that the world has had to endure over the past 20 months, my time in Alkmaar would not have been as enjoyable had it not been for the company of my flatmates - Fabian, Vadim, Prakash and Bose - along with my office-mate and honorary flatmate in Muaaz, and Siddharth. Thank you, Brian and Sahu, for being my TU Delft support and motivation crew, which also extends to Parv, Uttam, Abhyuday, and the Volendam IP group. To my cabals of friends from back home in India, your support is always appreciated. Finally, to my strongest pillar of support that is my family, words can't express the gratitude I have for your unwavering faith in me, and I hope one day to repay that faith and make you proud!

Aniketh Ajay Kumar
Delft, November 2021

Contents

List of Figures

List of Tables

Nomenclature

List of Abbreviations

CFD	Computational Fluid Dynamics
DNS	Direct Numerical Simulation
RANS	Reynolds-Averaged Navier-Stokes
UDNS	Under-resolved Direct Numerical Simulation
CHT	Conjugate Heat Transfer
CFL	Courant-Friedrichs-Lewy
EVM	Eddy Viscosity Models
RSM	Reynolds Stress Models
PDE	Partial Differential Equation
SST	Shear Stress Transport
MOTHER	MOdelling T-junction HEat Transfer
LES	Large Eddy Simulation
OECD	Organisation for Economic Co-operation and Development
NEA	Nuclear Energy Agency
URANS	Unsteady Reynolds-Averaged Navier-Stokes
DES	Detached Eddy Simulation
SSM	Standard Smagorinsky Model
SAS	Scale Adaptive Simulation
RSM-EB	RSM-Elliptic Blending
OIFS	Operator Integration Factor Schemes
FFT	Flow Through Times
TKE	Turbulence Kinetic Energy
PS	Passive Scalar

List of Abbreviations

ρ	Density
u	Velocity
p	Pressure
u_τ	Wall friction velocity
T	Temperature
D	Diameter
μ	Dynamic viscosity
ν	Kinematic viscosity
Re	Reynolds number
Pr	Prandtl number
Re_τ	Friction Reynolds number
T_{ij}	Stress Tensor for a Newtonian fluid
δ_{ij}	Kronecker delta
τ_{ij}	Viscous stress tensor
$\langle\rangle$	Time-averaged value
$'$	Fluctuating value
τ_{ij}	Reynolds Stress Tensor
k	Turbulence kinetic energy
ϵ	Dissipation rate
ω	Specific dissipation rate
ν_t	Eddy viscosity
C_μ	Model coefficient
f_μ	Damping function
r_c	Radius of curvature
G_1	Ratio of thermal diffusivity of the fluid to the solid
G_2	Ratio of thermal conductivity of the solid to the fluid
α	Thermal diffusivity
λ	Thermal conductivity
T_∞	Ambient temperature
η_k	Kolmogorov length-scale
τ_k	Kolmogorov time-scale
η_k	Normalized Kolmogorov length-scale
τ_k	Normalized Kolmogorov time-scale
t^+	Non-dimensional time
t^+	Non-dimensional time (in wall units)
C_p	Specific Heat Capacity

1 Introduction

T-junction geometries are widely used in the nuclear industry, as well as other industries, where the mixing of fluids of different temperatures takes place in the cooling circuits of reactors and other machinery. Understanding and predicting the effects of thermal mixing which result in cyclical thermal stresses and ultimately thermal fatigue on the walls of T-junctions can lead to major advancements in the design of T-junction geometries, having significant positive implications on the safety, maintenance and operational life-cycle of these cooling components. Numerous experiments and projects have been undertaken to study the phenomena of thermal mixing between the fluids and thermal striping/fatigue on the wall of the geometry. However, these experiments are performed at high Reynolds numbers which are computationally too expensive to simulate. Furthermore, these experimental databases do not provide sufficient detail while describing the underlying turbulence and heat transfer physics, such as the velocity and temperature fluctuations in regions close to the wall, which are crucial to understanding the thermal fatigue on the wall.

The existing experimental databases indicate the necessity for numerical simulations to accurately predict the turbulent thermal mixing between the fluids, and as a result, the thermal fatigue in the solid walls. The validation of RANS modelling strategies also requires a high-quality reference database to further develop and calibrate these models. The thesis intends to generate a DNS database for thermal mixing in a T-junction. Reference experimental data sets in the literature employ geometries comprising of sharp corners at significantly high Reynolds numbers, which are computationally too expensive to reproduce in a DNS calculation.

A preliminary calibration exercise is conducted in order to set up a DNS case, using computationally less expensive RANS simulations. The turbulence model to be used for the RANS simulations is selected based on information from the literature as well as some additional simulation work and analysis. The corner shape required in the geometry is then identified, followed by the scaling down of the Reynolds number to a more computationally feasible value for a DNS, without significant loss in fundamental flow features. This is followed by a geometry optimization procedure to reduce the computational domain required. These simulations give estimates that help set up a sample UDNS calculation. The implementation of a mixed (Robin) boundary condition to mimic a Conjugate Heat Transfer (CHT) thermal condition between the fluid and the solid walls in a T-junction geometry is also analysed. The results of this UDNS are then used to finalize the simulation and mesh parameters for a fully-resolved DNS.

The project can serve as a precedent to other researchers on how to go about using relatively inexpensive RANS simulations to aid the setup of a UDNS calculation, whose results can in turn be used to set up in a fully-resolved DNS case of the thermal mixing in a T-junction. This fully-resolved DNS can act as a comprehensive database to study the fluctuations in the velocity and thermal fields of the T-junction thermal mixing, especially for regions close to the wall, while also aiding the calibration and validation of existing turbulence models.

2

Research Objective and Research Questions

The thesis aims to implement relatively computationally cheap RANS simulations to enable calibrations of benchmark reference simulations in the increasingly relevant field of interest of thermal mixing and fatigue in T-junction geometries. The RANS work acts as a precursory set of simulations to obtain information that can eventually lead to the set up of a fully-resolved DNS case, which can then act as a benchmark calculation with which existing turbulence momentum and heat flux models can be validated. The main research objective of this thesis can be stated as:

> "To achieve the design of a Direct Numerical Simulation of flow and heat transfer in a T-junction, calibrated using RANS simulations, thus providing a high-quality reference numerical experiment. The feasibility of the DNS calculation is also assessed with a preliminary under-resolved calculation."

The existing literature in the field of T-junction thermal mixing was surveyed and it was found that the implementation of RANS simulations as a tool to calibrate a DNS benchmark, specifically to study the phenomena of thermal mixing and fatigue in a T-junction geometry is unique. This leads to the formulation of the following research questions that drive this thesis:

1. **Can RANS simulations be used to calibrate and validate a fully-resolved DNS test case?**
   (a) What is the minimum radius of curvature of the corner shape in the T-junction geometry that can be used to replace a sharp corner geometry while accurately reproducing the fundamental turbulence and thermal mixing phenomena?
   (b) Can RANS simulations be used to scale down the Reynolds numbers from that of the experimental reference cases to a more computationally feasible value? Can the underlying turbulence and thermal mixing phenomena be reproduced adequately at this lower value?
   (c) What length of the inlet, branch, and outlet geometries will be needed to prevent any upstream or downstream effects on the mixing of the fluids in the T-junction regions of interest?
   (d) What is the sensitivity of the mesh cell size on the accuracy of the results? How coarse can the mesh be made without significantly affecting the results?
   (e) Can accurate estimates be made from the wall shear stress, friction velocity, wall Y+ from the results of the RANS simulations to fix on Kolmogorov Length scales and wall cell sizes for the required DNS case?
2. **How would the UDNS results aid in calibrating a final fully-resolved DNS case?**
   (a) What time-averaging strategy should be implemented to capture the transient features of the UDNS case?

(b) What additional information would the UDNS case give us in order to calculate the final Kolmogorov scales and wall friction values?

(c) Would the distribution of the Courant-Friedrichs-Lewy (CFL) number pose any problem to the final DNS case in regards to the maximum time-stepping allowed and therefore the computational time required?

(d) Can the UDNS case produce results that provide a foundation (initial condition) to implement a Robin boundary condition as a passive scalar in the fully-resolved DNS case?

- Would the proposed Robin boundary condition offer significant computational cost advantages over the widely used conjugate heat transfer boundary condition?

These research questions can be fulfilled through the completion of a sequence of simulations and the interpretations of their results. These simulations are listed into the following tasks:

1. Identifying the most suitable turbulence model by ascertaining the sensitivities to the different phenomena expected in the simulation.
2. Running preliminary 2D simulations to narrow down the range of the T-junction corner radius, followed by 3D simulations that will aid the decision on the final corner radius to be implemented.
3. Investigating the feasibility of scaling down the Reynolds number of the simulation without losing any of the underlying thermal mixing and fatigue phenomena.
4. Optimization of the required pipe lengths in the geometry inlet, branch and outlet regions, such that the lengths are sufficient to prevent any interference on the mixing in the T-junction.
5. Performing a mesh sensitivity analysis to reduce computational costs associated with the mesh cell size used, while ensuring minimization of uncertainties due to the mesh discretization.
6. Estimating Kolmogorov length scales and wall cell sizes from the RANS simulations to help aid the mesh creation for the UDNS case.
7. Perform the UDNS calculation, interpret the results and make recommendations that can be implemented for the fully-resolved DNS simulation.

The first few steps are aided by the literature survey which would help select the appropriate turbulence model, and determine the range to begin the corner shape calibration with . It is important to note that the mesh sensitivity study was carried out as multiple iterations along with the previous studies to ensure an optimum mesh scheme was used for all the simulations. However, only the final iteration is mentioned in the report.

3

Literature Survey

3.1. Theoretical Background: RANS Methodology

Fluid dynamics is a field categorized by the types of flow which are governed by equations depending on the properties of the flow. The properties of the flow can change whether the flow is compressible or incompressible, viscous or inviscid, laminar or turbulent and so on. An incompressible flow is one where the density of the fluid is constant, or if the velocity of the fluid is small compared to the speed of sound in that fluid (Mach number ≤ 0.3). Incompressible flows are are highly resistant to forces of compression. Inviscid flows are characterized by nearly negligible shear forces and thus low viscosity. Flows which display highly irregular flow patterns in space and time are called turbulent flows, characterized by the non-dimensional Reynolds number, which gives a threshold of transition between turbulent and laminar flows. The Reynolds number is governed by the ratio of the inertial forces to the viscous forces in the fluid, and incorporates the velocity, density, characteristic length scale and the viscosity of the fluid. The equations that govern fluid dynamics are given below in the form of the conservation of mass, momentum and energy relations [1].

Conservation of Mass: The total mass of fluid in a closed system is constant over time.

$$\frac{\partial \rho}{\partial t} + \frac{\partial \rho u_i}{\partial x_i} = 0 \tag{3.1}$$

ρ is the density of the fluid, u the velocity with the subscript giving the component of the velocity vector. For an incompressible fluid with constant density, this equation reduces to:

$$\frac{\partial u_i}{\partial x_i} = 0 \tag{3.2}$$

Conservation of Momentum: Derived from Newton's second law, the change in momentum of a system is due to an external force **F** acting on it.

$$\frac{\partial \rho u_j}{\partial t} + \frac{\partial \rho u_i u_j}{\partial x_i} = \frac{\partial T_{ij}}{\partial x_i} + \rho f_j \tag{3.3}$$

T_{ij} is the stress tensor for a Newtonian fluid, and is the sum of the pressure and viscous stress (Stokes hypothesis).

$$T_{ij} = -p\delta_{ij} + \tau_{ij} \tag{3.4}$$

where δ_{ij} is the Kronecker delta. The viscous stress tensor, τ_{ij}, can be written as:

$$\tau_{ij} = \mu\left(\frac{\partial u_i}{\partial x_j} + \frac{\partial u_j}{\partial x_i} - \frac{2}{3}\delta_{ij}\frac{\partial u_k}{\partial x_k}\right) \tag{3.5}$$

The conservation of total energy is given by the following equation:

$$\frac{\partial \rho E}{\partial t} + \frac{\partial \rho E u_i}{\partial x_i} = \frac{\partial T_{ij} u_j}{\partial x_i} - \frac{\partial q_i}{\partial x_i} + \rho f_j u_j \tag{3.6}$$

The equations of conservation of mass and momentum for fluids together form the Navier-Stokes equations, in the Eulerian frame of reference. These Navier-Stokes equations can be solved for the steady mean solution, by decomposing the velocity, u into its time-averaged value and fluctuating components.

$$u_i = \langle u_i \rangle + u_i' \tag{3.7}$$

where for a statistically stationary process, the time-averaged value is given by:

$$\langle u_i \rangle = \lim_{t \to \infty} \frac{1}{t} \int_0^t u_i \left(t'\right) dt' \tag{3.8}$$

Substituting the sum of the mean value and fluctuation component into the Navier-Stokes equations, followed by which the averaging operator is applied, and simplifying the resulting equation by removing non-contributing terms, gives the Reynolds-Averaged Navier-Stokes (RANS) equations. These equations for an incompressible fluid with constant density and constant viscosity with just the time-averaged terms can be written as:

$$\frac{\partial \langle u_i \rangle}{\partial t} + \langle u_j \rangle \frac{\partial \langle u_i \rangle}{\partial x_j} + \frac{1}{\rho} \frac{\partial \langle p \rangle}{\partial x_i} - \nu \frac{\partial^2 \langle u_i \rangle}{\partial x_j \partial x_j} = \frac{\partial \tau_{ij}}{\partial x_j} \tag{3.9}$$

$$\frac{\partial \langle u_i \rangle}{\partial x_i} = 0 \tag{3.10}$$

The term $\tau_{ij} = -\left\langle {u_i}' {u_j}' \right\rangle$ is referred to as the Reynolds Stress Tensor. A conservation law for the Reynolds Stress Transport equation can be derived by using the momentum equation and averaging operator to give [1]:

$$\frac{\partial \left\langle u_i' u_j' \right\rangle}{\partial t} + \underbrace{K_{ij}}_{\text{Advection}} = \underbrace{P_{ij}}_{\text{Production}} + \underbrace{T_{ij} + D_{ij}^{v} + D_{ij}^{p}}_{\text{Diffusion}} + \underbrace{\Phi_{ij}}_{\text{Pressure strain correlation}} - \underbrace{\epsilon_{ij}}_{\text{Dissipation}} \tag{3.11}$$

The terms mentioned in the above equation can be expanded and include additional unknown quantities, which might require modelling. The terms are:

- **Advection**: Mean flow transport.

$$K_{ij} = \langle u_k \rangle \frac{\partial \left\langle u_i' u_j' \right\rangle}{\partial x_k} \tag{3.12}$$

- **Turbulent Diffusion**: Turbulence transport.

$$T_{ij} = \frac{\partial \left\langle u_i' u_j' u_k' \right\rangle}{\partial x_k} \tag{3.13}$$

- **Production**: Source term, increases turbulence intensity through energy transfer from the mean flow.

$$P_{ij} = -\left(\left\langle u_i' u_k' \right\rangle \frac{\partial \left\langle u_j \right\rangle}{\partial x_k} + \left\langle u_j' u_k' \right\rangle \frac{\partial \left\langle u_i \right\rangle}{\partial x_k} \right) \tag{3.14}$$

- **Viscous diffusion**: Viscous stress transport.

$$D_{ij}^{v} = \nu \frac{\partial^2 \left\langle u_i' u_j' \right\rangle}{\partial x_k \partial x_k} \tag{3.15}$$

- **Pressure Diffusion**: Transport by pressure fluctuations.

$$D_{ij}^{p} = -\frac{1}{\rho}\left(\frac{\partial\left\langle u_j' p'\right\rangle}{\partial x_k} + \frac{\partial\left\langle u_i' p'\right\rangle}{\partial x_k}\right) \tag{3.16}$$

- **Pressure Strain correlation**: Pressure-rate-of-strain tensor, energy redistribution.

$$\Phi_{ij} = \left\langle \frac{p'}{\rho}\left(\frac{\partial u_j'}{\partial x_i} + \frac{\partial u_i'}{\partial x_j}\right)\right\rangle \tag{3.17}$$

- **Dissipation**: Sink term dissipating into thermal energy.

$$\epsilon_{ij} = 2\nu\left\langle \frac{\partial u_j'}{\partial x_k}\frac{\partial u_i'}{\partial x_k}\right\rangle \tag{3.18}$$

where ν is the kinematic viscosity. This Reynolds Stress Tensor equation contains many unknown correlations such as the third-order term in Equation 3.13 which could have their own similar conservation law derivation, which would however only give rise to more unknown quantities. Therefore, since the number of unknowns only increase with each further derivation, this closure problem of having more unknown quantities than equation to solve cannot be satisfied and thus requires modelling the unknown quantities using empirical approximations that give rise to what is known as Turbulence models.

Turbulence models for RANS equations are of two types - Eddy Viscosity Models (EVM), and Reynolds Stress Models (RSM). The Eddy Viscosity Models can be algebraic (0-equation models) like the Prandtl mixing length model (1925) or the Baldwin-Lomax model (1978) [2]. EVMs can also have one or more transport equations like the Spalart-Allmaras model (1992)[3], the Jones-Launder model (1972)[4], the Wilcox models (1988 [5], 2008 [6]), and the Menter model (1993) [7]. There are also non-linear Eddy Viscosity Models, followed by Reynolds Stress Models which can be algebraic, or contain the full Reynolds Stress Transport equation with additional transport equations for other unknowns. Keeping in mind the scope of the thesis, the non-linear Eddy Viscosity models and the Reynolds Stress Models are not implemented and thus not explained further. The thesis focuses on the two-equation Eddy Viscosity Models which contain transport equations for the turbulence kinetic energy, k and either the dissipation rate ϵ or the specific dissipation rate ω.

The Eddy Viscosity Models are based on the eddy viscosity hypothesis that the turbulence leads to momentum exchange between the elements of the fluid. Mathematically, this is translated to the model relation that the Reynolds Stress term is assumed proportional to the mean strain rate by a proportionality factor known as the eddy viscosity ν_t. This assumption results in the inability to distinguish the effects of the Reynolds stress tensor components, therefore failing to capture anisotropic effects, the likes of which include directional volume forces like gravity, and streamline curvature. The mathematical relation is given below:

$$-\left\langle u_i' u_j'\right\rangle \cong 2\nu_T S_{ij} - \frac{2}{3}\delta_{ij}k \tag{3.19}$$

where ν_t is the turbulent viscosity, k is the turbulent kinetic energy, and ϵ is the dissipation rate. δ_{ij} is the Kronecker delta, given by:

$$\delta_{ij} = \begin{cases} 1 & \text{, if } i = j \\ 0 & \text{, if } i \neq j \end{cases} \tag{3.20}$$

The strain rate is given as:

$$S_{ij} = \frac{1}{2}\left(\frac{\partial\left\langle u_i\right\rangle}{\partial x_j} + \frac{\partial\left\langle u_j\right\rangle}{\partial x_i}\right) - \frac{1}{3}\delta_{ij}\frac{\partial\left\langle u_k\right\rangle}{\partial x_k} \tag{3.21}$$

and the turbulence kinetic energy:

$$k = \frac{1}{2}\left\langle u_i' u_i' \right\rangle = \frac{1}{2}\sum_{i=1}^{3}\left\langle u_i' u_i' \right\rangle \tag{3.22}$$

The EVM hypothesis can now be placed into the RANS equation to yield:

$$\frac{\partial \left\langle u_{\mathrm{i}} \right\rangle}{\partial \mathrm{t}} + \left\langle u_j \right\rangle \frac{\partial \left\langle u_i \right\rangle}{\partial x_j} = -\frac{\partial}{\partial x_i}\left(\frac{\langle p \rangle}{\rho} + \frac{2}{3}k\right) + \frac{\partial}{\partial x_j}\left(2\left(\nu + \nu_{\mathrm{t}}\right) S_{ij}\right) \tag{3.23}$$

The Reynolds Stress Tensor is effectively reduced from the six individual components into a single scalar called the eddy viscosity, ν_t. Depending on the dimensional arguments, the eddy viscosity can be expressed as a function of the mean velocity field in multiple ways. This is what gives rise to the zero-equation, one-equation, and two-equation models. The number of equations correlates to the number of required transport equations for the model. The focus is only on the two-equation models hereafter, with the relationship for the eddy viscosity given as:

$$\nu_t \propto \frac{k^2}{\epsilon} \tag{3.24}$$

$$\nu_t \propto \frac{k}{\omega} \tag{3.25}$$

The first of the two-equation models is the Jones and Launder two-equation model (1972) [4]. This is also called the $k-\epsilon$ model, one of the most widely used models in RANS simulations, where an equilibrium between the turbulence production and dissipation is assumed. This gives rise to a partial differential equation (PDE) for the turbulence kinetic energy k and a transport equation that follows this PDE of k for the turbulence dissipation rate ϵ. The relation between k and ϵ is:

$$\nu_t = C_\mu \frac{k^2}{\epsilon} \tag{3.26}$$

where C_μ is a model parameter. The transport equation for k is:

$$\frac{\partial k}{\partial t} + \underbrace{\left\langle u_j \right\rangle \frac{\partial k}{\partial x_j}}_{\text{Advection}} = \underbrace{\tau_{ij}\frac{\partial \left\langle u_i \right\rangle}{\partial x_j}}_{\text{Production}} + \underbrace{\frac{\partial}{\partial x_j}\left(\left[\frac{1}{\mathrm{Re}} + \frac{\nu_t}{\mathrm{Pr}_k}\right]\frac{\partial k}{\partial x_j}\right)}_{\text{Diffusion}} - \underbrace{\epsilon}_{\text{Dissipation}} \tag{3.27}$$

and for the turbulence dissipation rate ϵ:

$$\frac{\partial \epsilon}{\partial t} + \underbrace{\left\langle u_j \right\rangle \frac{\partial \epsilon}{\partial x_j}}_{\text{Advection}} = \underbrace{C_{\epsilon 1}\frac{\epsilon}{k}\tau_{ij}\frac{\partial \left\langle u_i \right\rangle}{\partial x_j}}_{\text{Production}} + \underbrace{\frac{\partial}{\partial x_j}\left(\left[\frac{1}{\mathrm{Re}} + \frac{\nu_t}{\mathrm{Pr}_\epsilon}\right]\frac{\partial \epsilon}{\partial x_j}\right)}_{\text{Diffusion}} - \underbrace{C_{\epsilon 2}\frac{\epsilon^2}{k}}_{\text{Dissipation}} \tag{3.28}$$

The constants present in the equation have values that are derived from reference flow cases, which comes with the caveat that this model may not always be able to accurately predict complex flows. The $k-\epsilon$ turbulence model is known to give good predictions for external flows, and works well in the absence of strong pressure gradients, streamline curvature or flow separation.

Within the commercial software of Siemens Star-CCM+ [8], there is the additional option to choose a Linear low-Reynolds $k-\epsilon$ and a Cubic low-Reynolds $k-\epsilon$ turbulence model [9]. These are modifications of the standard high-Reynolds $k-\epsilon$ turbulence models to extend them to low-Reynolds number conditions found near the wall. The linear and cubic terms refer to the constitutive relation used to describe the relation between the Reynolds stress tensor and the mean strain rate. A linear constitutive relation implies the use of a Boussinesq approximation. Non-linear constitutive relations like the cubic relation are used when it is necessary to account for anisotropic turbulence, rotation and streamline curvature [10]. This is done by adding non-linear (cubic) terms to the relation between the mean strain rate and Reynolds stress tensor given by Equation 3.19, where the mean rate of the strain tensor S_{ij}

is given by Equation 3.20. In Star-CCM+, for the implementation of the cubic constitutive relation, a variable coefficient for C_μ is used instead of the constant value of C_μ in the relation for the turbulent viscosity ν_t [8].

$$\nu_t = \rho C_\mu f_\mu k T \tag{3.29}$$

where ρ is the density, C_μ is a model coefficient, f_μ is a damping function, k is the turbulence kinetic energy, and T is the turbulent time scale.

Another two-equation model is the Wilcox two-equation model, more commonly known as the $k-\omega$ turbulence model. Yet another commonly used model in RANS, this model differs from the previous one in the second transport equation, where the dissipation rate ϵ is replaced by the specific turbulence dissipation rate ω

$$\nu_t = \frac{k}{\omega}; \omega = \frac{1}{C_\mu}\frac{\epsilon}{k} \tag{3.30}$$

which gives for k and ω:

$$\frac{\partial k}{\partial t} + \underbrace{\langle u_j \rangle \frac{\partial k}{\partial x_j}}_{\text{Advection}} = \underbrace{\tau_{ij}\frac{\partial \langle u_i \rangle}{\partial x_j}}_{\text{Production}} + \underbrace{\frac{\partial}{\partial x_j}\left(\left[\frac{1}{\mathrm{Re}} + \frac{\nu_t}{\mathrm{Pr}_k}\right]\frac{\partial k}{\partial x_j}\right)}_{\text{Diffusion}} - \underbrace{C_\mu k \omega}_{\text{Dissipation}} \tag{3.31}$$

$$\frac{\partial \omega}{\partial t} + \underbrace{\langle u_j \rangle \frac{\partial \omega}{\partial x_j}}_{\text{Advection}} = \underbrace{\alpha\frac{\omega}{k}\tau_{ij}\frac{\partial \langle u_i \rangle}{\partial x_j}}_{\text{Production}} + \underbrace{\frac{\partial}{\partial x_j}\left(\left[\frac{1}{\mathrm{Re}} + \frac{\nu_t}{\mathrm{Pr}_\omega}\right]\frac{\partial \omega}{\partial x_j}\right)}_{\text{Diffusion}} - \underbrace{\beta\omega^2}_{\text{Dissipation}} \tag{3.32}$$

The $k-\omega$ turbulence model is found to work well with boundary layer flows, and in the presence of pressure gradients and flow separation. The model is however less suitable for external aerodynamics due to its sensitivity to the inflow and free-stream boundary conditions. The model also over-predicts the turbulence production in regions of stagnation.

Finally, there is the $k-\omega$ Shear Stress Transport (SST) model (also available in Star-CCM+) which is a combination of the $k-\epsilon$ and $k-\omega$ models [7]. This involves a modification to the eddy viscosity term based on the idea implemented in another model, called the Johnson-King model [11]. It follows that the prediction of severe adverse pressure gradient flows is highly reliant on the transport of the principal turbulent shear stress. The SST model shows a great improvement in the prediction of flows involving adverse pressure gradients and is thus strongly suited for external flow (aerodynamic) applications. The model has also displayed the capability to accurately predict pressure-induced separation and the resulting viscous-inviscid interaction.

The choice of two-equation Eddy Viscosity turbulence models needs to be carefully considered according to the type of underlying fluid phenomena in question, such as flow separation, strength of pressure gradients expected etc. The commercial CFD software Star-CCM+ does provide the option to choose between these common two-equation RANS turbulence models, with additional flexibility provided regarding the constitutive relations, empirically determined correction factors, as well as avenues for the modification of other constants involved in the transport equations.

3.2. Experimental Facilities

The literature review was conducted on the topic of T-junction simulations, the different types of simulations used and the reference cases that were checked and compared against as the benchmark, be it experimental cases or DNS cases. The literature involving T-junction simulations use reference experimental or simulation results as a benchmark for their comparisons or validations. These include experiments done with different T-junction geometries, at different Reynolds numbers. A table of the reference cases most commonly used in the different literature is presented below in Table 3.1, along with some of the important geometrical and flow parameters used in the models.

As can be seen in the table below, the most common geometries include a diameter ratio (ratio of the diameter of the branch inlet to the diameter of the main inlet) of either 1 or 0.33. It is also noticed that the first three reference cases, i.e. the Fatherino Facility experimental cases, and the MOTHER (MOdelling T-junction HEat Transfer) Project case are most frequently used in benchmarking simulations of T-junctions to compare the performance of different CFD approaches. It is noted that all the experimental cases are conducted at Reynolds numbers that are too high to be reproduced in DNS calculations. DNS benchmark cases are usually conducted for pipe flows in the region of friction Reynolds number $Re_\tau = 180, 360, 550$ which correspond to bulk Reynolds number values of $5000 - 12000$, much lower than what can be seen here in experimental cases. Sharp corner geometries may also pose a challenge while modelling the discretized computational domain for DNS cases.

Table 3.1: Reference Experimental Cases for T-junction simulations

Name	Main Inlet Diameter (m)	Branch Inlet Diameter (m)	Diameter Ratio	Main Inlet Reynolds Number	Branch Inlet Reynolds Number	Outlet Reynolds Number	Main Temperature (C)	Branch Temperature (C)	Δ T (C)	Corner Type
FATHERINO (1)	0.054	0.054	1	40000	40000	80000	15	30	15	Sharp, Round (R =18mm)
FATHERINO (2)	0.054	0.054	1	60000	60000	120000	15	30	15	Sharp, Round (R =18mm)
MOTHER PROJECT	0.054	0.054	1	19540	19540	39080	15	30	15	Round (R=18mm)
WALTON	0.15	0.05	0.33	191300	33200	202400	48	33	15	Sharp
	0.15	0.05	0.33	382600	66400	404800	48	33	15	Sharp
	0.15	0.05	0.33	571300	99700	604500	48	33	15	Sharp
	0.15	0.05	0.33	60300	66400	82400	48	33	15	Sharp
	0.15	0.05	0.33	120600	66400	142700	48	33	15	Sharp
VATTENFALL (1)	0.14	0.1	0.714	95700	95300	163000	15	30	15	Sharp
VATTENFALL (Jayaraju et al.[12])	0.14	0.1	0.714	24500	24500	42000	15	30	15	Sharp
VATTENFALL (Smith et al.[13])	0.14	0.1	0.714	79500	107700	156400	19	36	17	Sharp
T-cubic	0.15	0.05	0.33	170000	69500	193100	25.7	59.8	24.1	Sharp
M Aounallah et al. [14]	0.15	0.05	0.33	70000	137000	115700	15	50	35	Sharp
Paul Scherrer Institute or ETHZ	0.051	0.051	1	43860	43860	87720	25	25	0	Sharp

To design the geometry to be used in the RANS simulations in the thesis, the reference experimental case of the Fatherino facility can be chosen. The diameter ratio in this geometry is 1, and the velocities of the flow through both the pipes are equal. The temperature difference between the flows is $\Delta T = 15K$. The geometry involved uses both a sharp corner and a rounded corner with curvature $r_c = 18mm$. This geometry is used for Reynolds numbers of 40000, 60000, as well as close to 20000 (in the MOTHER Project).

3.3. Numerical Work

The turbulent mixing of fluids in a T-junction leads to a transient with high amplitude temperature fluctuations at the walls. These fluctuations require an accurate prediction in order to evaluate the thermal stresses formed at the pipe walls. The existing body of work on the topic of studying thermal fatigue in T-junction geometries is extensive with regards to the Large Eddy Simulation (LES) and RANS simulation solutions being checked for their performance against reference experimental and DNS cases. These include an OECD/NEA CFD benchmarking experiment to study the accuracy of CFD turbulence models in predicting the thermal fluctuations for the Vattenfall T-junction configuration [13]. LES, Hybrid (RANS/LES) and Unsteady-RANS (URANS) approaches were implemented here and compared to experimental measurements. The MOTHER project [15] was also another initiative between multiple parties to study this topic.

The work of Georgiou and Papalexandris [16] showed that the important features involved in the flow include the large recirculation bubble and the separation zone formed at the junction region, where the jet from the branch pipe enters the main pipe. It was concluded that the thermal mixing that is observed is a result of the shear layer between the mixing fluids, and additionally, the shear layer between the branch fluid jet and the recirculation bubble. The thermal mixing is also enhanced by the turbulence generated in the adverse pressure gradient regions downstream of the large recirculation bubble. This work also compared the DNS of the heat transfer in a T-junction to the performance of a wall-resolved LES and concluded that the LES performed satisfactorily.

It is found that the focus of the CFD simulations should be on the velocity profile close to the wall immediately downstream of the junction, as this is the region with the maximum fluctuations in velocity values observed. These frequent fluctuations in velocity directly affect the temperature field on the surface of the wall and influence the phenomena of thermal fatigue. Heat transfer takes place through the walls of the T-junction. Computationally, this could be implemented either by using an iso-thermal condition, i.e. keeping the wall temperature fixed while allowing heat-flux to pass through the boundary, or by making the walls adiabatic in nature, using a constant heat flux value on the walls and a varying wall temperature [12]. The effect of the solid walls can be established using conjugate heat transfer boundary conditions as well, however, this wasn't considered in the RANS simulations.

The effect of the Prandtl number needs to be considered as well. The Prandtl number acts to provide information on the sensitivity of the different fields to diffusion. A Prandtl number greater than 1 implies lesser sensitivity between the thermal field to thermal diffusion, in comparison to the sensitivity between the velocity and molecular viscosity [17]. The Prandtl number can thus be defined as the ratio of the momentum to thermal diffusivity.

The selection of the geometric parameters and flow parameters in the T-junction also governs the thermal mixing taking place in the junction. Mixing phenomena in a T-junction can be classified into three patterns depending on the direction of the jet exiting from the branch pipe into a wall jet flow, impinging jet flow and a deflecting jet pattern. The temperature fields and its fluctuation intensity depended on these patterns. The flow patterns could be predicted by a momentum ratio of the flows in the main to branch pipes. The momentum ratio is given by:

$$M_R = \frac{M_m}{M_b} \tag{3.33}$$

$$M_m = D_m D_b \rho_m V_m^2; \quad M_b = \frac{\pi}{4} m D_b^2 \rho_b V_b^2 \tag{3.34}$$

of the two inlet pipe flows. D is the diameter of the pipe, ρ the density of the fluid, and V is the velocity

of the fluid in the pipe. The suffix m refers to the main pipe, b is the branch pipe, and R implies the ratio. This is mentioned in Kamide et al.(2009) [18].

1. Wall jet: Due to the higher main pipe flow velocity, attached flow (to the wall) is expected downstream of the junction. ($M_R > 1.35$)
2. Deflecting jet: Flow takes place through the middle of the pipe. ($0.35 < M_R < 1.35$)
3. Impinging jet: The high flow velocity in the branch pipe causes the jet to fall on the opposite half of the main pipe. ($M_R < 0.35$)

The experimental images of the three patterns are shown below in Figure 3.1, decided by the momentum ratio of the flows as mentioned above.

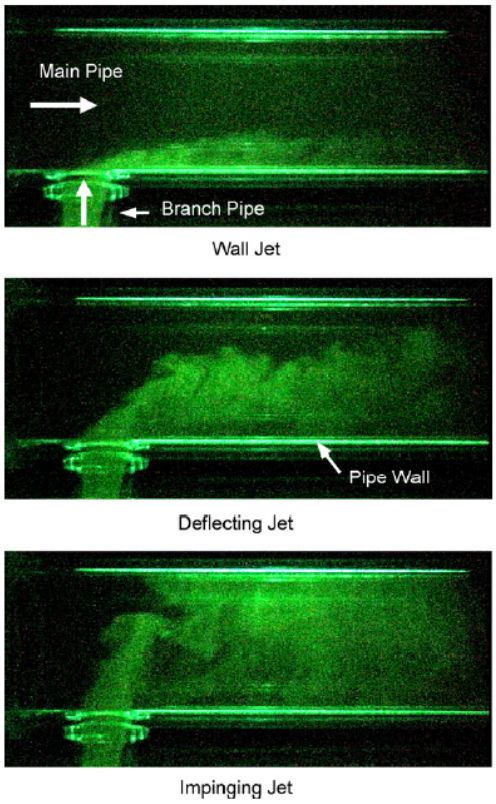

Figure 3.1: Classification of flow patterns taken from Kamide et al.(2009) [18]

The results of these cases were also presented in [18]. In the wall jet case, temperature fluctuation intensities were high at the boundary region around the cold fluid flow, while the deflecting jet case displayed insignificant intensity of fluctuations near the pipe wall. In the impinging jet case, the cold jet from the branch pipe reached the opposite side of the pipe, but fluctuations were seen immediately downstream of the T-junction in the upper half of the main pipe. The collapse of the jet at the pipe wall increased the mixing of the flows.
Considering the types of experimental cases found in literature, and the need to be able to replace these with a high quality DNS database, the implementation of a geometrical domain similar to that seen in the Fatherino facility (Table 3.1), results in a momentum ratio that causes the jet pattern to become a deflecting jet type.
CFD simulations of fluid flow and temperature fields at a T-junction were performed using different turbulence models, using both LES and RANS simulations. De Santis and Shams (2018)[19] worked on LES solutions for the T-junction problem. They concluded that the fluctuations in the temperature fields were most accurately predicted by LES. However, LES based on the Detached Eddy Simulation (DES) and Standard Smagorinsky Model (SSM) was found unable to resolve the temperature fluctuations well

[20]. LES is also computationally very expensive, with costs scaling rapidly with the Reynolds number and therefore remaining far from a widespread industrial use [13].

Unsteady-state turbulence models, such as LES, URANS or Scale Adaptive Simulations (SAS), are adept at resolving the fluctuations of the temperature field in a T-junction. The wall-resolved URANS simulations yielded favourable results for the transient features of temperature in the near-wall region [19]. It was however, unable to predict the unsteadiness of the flow upstream of the junction which was observed in the experimental measurements. URANS simulations predict near wall effects well, but deviate from the expected values in the separation region with an over-prediction of values (k-ϵ cubic model). These types of simulations consume a lot of time. This brings the need to use steady-state turbulence models for T-junction simulations, which can also predict accurately to capture the time-averaging thermal–hydraulic characteristics involved [21]. An analysis of both RANS and LES simulations was performed on the T-junction of a Phoenix reactor as well [22]. It was concluded that RANS models can produce viable results using less computational time, while LES is needed to partially resolve scales, at increased computational costs.

3.3.1. Turbulence Modelling

Using RANS based turbulence models like the Shear Stress Transport (SST) and Reynolds Stress Model (RSM) unsteady temperature fluctuations were not reproducible for the evaluation of thermal fatigue in a T-junction [23]. However, this is not a major concern as the mean thermal characteristics are able to be captured satisfactorily by steady-state RANS simulations. RANS simulations offer the flexibility of choice with respect to the turbulence model to be implemented, and therefore, selecting a suitable model which preserves the fundamental phenomena of turbulence and thermal mixing in a T-junction is relatively easy[14]. The two-equation Eddy Viscosity Models (EVM), the $k-\epsilon$ and $k-\omega$ turbulence model are the most commonly used RANS models. They are computationally less expensive in comparison to non-linear EVMs or Reynolds Stress Models, due to the presence of only two additional transport equations that are required to be solved. The $k-\omega$ turbulence model should be better equipped for the T-junction mixing flow, due to its ability to better handle flow separation and streamline curvature.

T-junction mixing involves non-equilibrium flows which would require the implementation of advanced wall functions to capture its effects. It was noticed that, generally, the wall-function models systematically under-predict the fluctuations near the boundaries. In contrast, the wall-resolved models predict a high value of the gradients in the stream-wise region near the walls [24]. This is explained due to the existence of the largest gradients within the viscous sub-layer (y+ range < 30), the resolution which is below that of the first grid point in a wall-function approach (y+ around 30). This implies that resolving these small-scale structures in the near wall regions is crucial to accurately predict the quantities. Mean quantities of the flow can be well captured using wall-function models, on the condition that the flow is fully developed, which however, depends on the Reynolds number. The heat transfer that takes place through the walls of the T-junction thus have a significant dependency on the predictions of the temperature by the model used.

The separation point is not fixed in curved corner simulations, and is sensitive to the turbulence model implemented. The resolution of the mesh in this separation region is also required to be appropriately considered for the T-junction simulation. The curved corner simulations show an under-prediction of velocity values in the zone of recirculation while using wall-function models, while wall-resolved models show an over-prediction of velocities[25].
The linear k-ϵ and the RSM-Elliptic Blending (RSM-EB) are less equipped to handle the fluctuations of the flow field compared to the cubic k-ϵ model [19]. Moreover, the RSM-EB under-predicts the velocity values within the recirculating region compared to the other two eddy viscosity models. It is also seen that the k-ω model showed better results as opposed to the cubic k-ϵ model [25], due to the ability of the k-ω model to better handle near-wall physical phenomena.

For the case of the k-ϵ model, modifying the turbulence model coefficients can impact accuracy of the solutions. Increasing the model coefficient C_μ enhances the turbulent momentum transfer. This leads

to improved prediction of the velocity profiles and an increased accuracy of the transport scalar profiles. However, increasing model coefficients may not be the best approach to fixing these associated issues. Model coefficients have to be based on direct estimations of turbulence parameters, while also being justified from a fundamental point of view. Validation can be done by checking the steady-state profiles, and then adjusting to improve the accuracy, as done in Walker et al.(2010)[26]. The manipulation of the turbulent Schmidt number proposed in literature [27] has less fundamental basis, since it is more of a specific quick fix than a complete solution [26]. As such, modification of these coefficients were not considered for the RANS simulations required in the thesis.

To summarise, the (wall-resolved) $k-\omega$ turbulence model is the best choice when requiring prediction of fields within the viscous sub-layer of the boundary layer. This model, unlike other two-equation models, does not involve damping functions, and thus due to its simplicity, the $k-\omega$ model shows superior numerical stability as well. Furthermore, the model is as accurate as the others in mean flow profile predictions, while also managing flow separation and streamline curvature better. Additionally, the $k-\omega$ SST model has also been tested for complex 3D flows with the results showing very favorably compared to that of a full Reynolds-stress model [7]. The $k-\omega$ and $k-\omega$ SST models therefore seem to be the best choices available within Star-CCM+ to carry out the RANS phase of the thesis with.

3.4. The Robin Boundary Condition

In DNS conducted before, the thermal boundary conditions imposed on the wall of internal flow geometries were usually of the iso-temperature (constant temperature - Dirichlet) boundary condition or the iso-flux (constant heat flux - Neumann) boundary condition. It is accepted that these boundary conditions do provide a useful investigation into the physical mechanisms responsible for heat transfer in the geometries, however, it is also widely recognised that neither of these conditions can mimic the actual heat transfer realistically, especially in cases where the thermal diffusivity of the fluid and the solid are within the same order of magnitude. These cases lead to a significant interaction thermally between the fluid and the solid at the interface and govern the thermal stressing and fatigue phenomena in the solid pipe walls in the T-junction case. A coupling between the two continua can be made using the conjugate heat transfer (CHT) boundary condition.

Conjugate heat transfer simulations are thus useful in industry based experiments where fluctuating thermal stresses are a concern like in the T-junction case. Investigations have also been made into the influence of the CHT boundary condition by comparing the results with the iso-temperature boundary condition [28]. The wall-modelling approach used in RANS and LES simulations for high Reynolds cases results in an unresolved viscous sub-layer. Therefore, DNS can provide a detailed insight into the flow physics of such complex phenomena which can lead to improvements in RANS and LES modelling.

However, the inclusion of a CHT condition with solid walls in a DNS requires an extremely high computational effort due to the large computational costs associated with the slow statistical convergence of the thermal fields in the solid region. To alleviate these costs, it was shown that a Robin (mixed) wall boundary condition can be implemented to mimic CHT [29]. The mixed boundary condition may be represented at the wall using the relation:

$$AT + B\partial_y T = C \tag{3.35}$$

where A, B and C are coefficients. $B = 0$ corresponds to a Dirichlet boundary condition, $A = 0$ a Neumann boundary condition, and $AB \neq 0$ is a Robin boundary condition. If B is equal to the thermal conductivity of the fluid, the parameter A becomes the heat exchange coefficient. For conjugate heat transfer cases, the equation of evolution of the passive scalar reads [30]:

$$\partial_t T + \partial_j \left(T u_j\right) = \alpha_f \partial^2_{jj} T \text{ in the fluid} \tag{3.36}$$

$$\partial_t T_s = \frac{\alpha_f}{G_1} \partial^2_{jj} T_s \text{ in the solid} \tag{3.37}$$

$$T_f = T_s \text{ and } \partial_y T_f = G_2 \partial_y T_s \text{ at the interface} \tag{3.38}$$

where G_1 is the ratio of thermal diffusivity of the fluid to the solid α_f/α_s, and G_2 is the ratio of thermal

conductivity of the solid to the fluid λ_s/λ_f. Using Equation 3.35 and multiplying Equation 3.37 by T' and $\partial_y T'$ directly leads to the linear system given below:

$$\begin{pmatrix} \overline{T} & \partial_y \overline{T} & -1 \\ \overline{T'^2} & \frac{1}{2}\partial_y \overline{T'^2} & 0 \\ \frac{1}{2}\partial_y \overline{T'^2} & \overline{\partial_y T' \partial_y T'} & 0 \end{pmatrix} \begin{pmatrix} A \\ B \\ C \end{pmatrix} = \begin{pmatrix} 0 \\ 0 \\ 0 \end{pmatrix} \tag{3.39}$$

where $\overline{T}$ and T' are the mean and fluctuating components of the instantaneous temperature T, respectively. Physically, the thermal conductivity and heat transfer coefficient cannot be zero. Therefore, the determinant of the first matrix must vanish to satisfy the linear system, giving rise to the following compatibility condition:

$$\overline{T'^2} \times \overline{\partial_y T' \partial_y T'} = \left(\frac{1}{2} \partial_y \overline{T'^2} \right)^2 \tag{3.40}$$

This equation gives a relation between the temperature variance at the wall, the derivative of the temperature variance at the wall, and the wall-normal component of the dissipation rate of the temperature variance. Looking at the relation given in 3.39 the coefficient C does not directly influence the statistics of the fluctuating temperature field. This leaves behind only one degree of freedom which is the ratio of A/B, given by:

$$\frac{A^2}{B^2} = \frac{\overline{T'^2}}{\overline{\partial_y T' \partial_y T'}} \tag{3.41}$$

where the numerator represents the temperature variance at the wall which may be obtained from an iso-flux condition since the Neumann boundary condition imposes the lack of wall fluctuations for the heat flux. Likewise, the denominator represents the wall-normal component of the dissipation of temperature variance, which can be found from an iso-temperature condition since the Dirichlet boundary condition imposes the lack of wall fluctuations for the temperature. The selection of the parameter set (A, B) governs the modelling strategy.

It was concluded in [29] that the case of conjugate heat-transfer implemented and compared to the Robin boundary condition simulation produced statistics that were close to each other for the turbulent heat fluxes, temperature variance and their budgets. However, analysis also shows that the conjugate heat-transfer case produces very large scale thermal structures that cannot be mimicked by the Robin boundary condition simulation but there is some uncertainty regarding the source of these large thermal structures observed. A Robin boundary condition with constant coefficients also faces difficulty in mimicking the non-local aspects of conjugate heat-transfer which were obtained from the analytical analysis. Additionally, the results of simulations carried out using different fluid and solid properties need to be studied.

In order to make a selection for the parameters A and B to be set in a DNS calculation with this implementation of the Robin boundary condition to replace a conjugate heat-transfer simulation, separate DNS calculations, for example, using channel flow cases, at relevant Reynolds numbers can be performed with iso-flux and iso-temperature boundary conditions. It was decided that this approach would be used in the UDNS calculations of the thesis which is to be carried out on Nek5000 [31]. To implement this Robin boundary condition in the architecture of Nek5000, the boundary condition can be written as:

$$-k\partial_y T = h(T - T_\infty) \tag{3.42}$$

with the coefficients being

$$B = k \tag{3.43}$$

$$A = h \tag{3.44}$$

$$C = A \times T_\infty \tag{3.45}$$

where k and h are the thermal conductivity and heat transfer coefficient respectively.
In-house UDNS calculations (A. Mathur, personal communication, February 21, 2021) were conducted on a turbulent channel flow case, in a geometry of $\frac{4}{3}\pi\delta \times 2\delta \times 4\pi\delta$, where $\delta = 1$ is the channel half-height and the Reynolds numbers for the channel flow are Re = 2800 and 6400, corresponding to Re_τ = 180 and 360. Table 3.2 gives the channel mesh statistics.

Table 3.2: Channel flow discretization statistics

	Re_τ **= 180**	Re_τ **= 360**
Grid	20 x 20 x 26	26 x 33 x 26
Macro-elements	10400	22308
Poly order	N = 5	N = 5
Wall-normal spacing, ($\Delta y+$)	0.36 – 9.3	0.5 – 14.4
Streamwise spacing, ($\Delta z+$)	17.4	27.5
Spanwise spacing, ($\Delta x+$)	7.6	11.6

The simulation was run with a time-stepping order, N_T = 3, solver tolerances of 1×10^{-5}, CFL = 2.0 (OIFS) [32] and for an averaging time of $\Delta t^* = 5000$, which is ≈400 Flow Through Times (FTTs). The simulation for the two Reynolds numbers were run at multiple different Prandtl numbers. The ratio of Equation 3.41 was calculated for every calculation from iso-flux and iso-temperature boundary condition passive scalars. The value of B is the same for all the simulations and is equal to B = k (= μ = 1/Re). Values of h and T_∞ were then computed for each calculation as per Equations 3.43 - 3.45. It is noted that the value of C was kept as unity to compute T_∞. This, however, is not of concern as C does not directly affect the temperature fluctuation statistics, as can be seen in Equation 3.39. Figure 3.2 below shows the trend of A with the Prandtl number for the two simulations run.

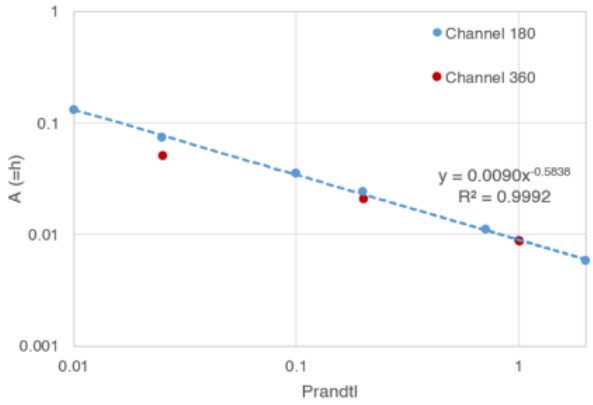

Figure 3.2: Channel Flow based Robin boundary condition coefficients

4

Calibration of the DNS Case using RANS Simulations

4.1. Turbulence Model Sensitivity

The literature survey highlighted that the two-equation Eddy Viscosity Models like the $k-\epsilon$ and $k-\omega$ turbulence models were the most commonly used, fast, robust and accurate models for steady-state RANS Simulations of the thermal mixing in T-junctions. Additionally, within Star-CCM+, there is the option to choose the $k-\omega$ SST-Menter turbulence model developed by Menter [7]. As mentioned in the literature survey, this model is a combination of the $k-\epsilon$ and $k-\omega$ turbulence models, and is known to provide good prediction capabilities in the presence of adverse pressure gradients. This model is therefore considered as well since the separation zone found in the thermal mixing problem in a T-junction is of great importance [16].

To analyse the performance of the turbulence models in Star-CCM+, the work of De Santis and Shams (2018) [19], was considered. Their work included testing the performance of a Linear low-Reynolds $k-\epsilon$ and a Cubic low-Reynolds $k-\epsilon$ turbulence model mentioned in Section 3.1. The work done by De Santis and Shams was validated with the experimental reference database of the WALTON facility (Table 3.1). The geometry used also represents the T-junction of the WALTON facility. The inner diameter of the main pipe is, $D_m = 0.15m$ and the branch diameter is $D_b = 0.05m$. Both inlet pipes have the same length upstream of the junction, equal to $3D_m$. The outlet pipe downstream of the junction has a length of $7D_m$ which is enough to prevent flow reversal at the outlet section. The geometry is shown below in Figure 4.1.
Adiabatic no-slip walls are set as the boundary condition, and a pressure outlet is defined on the outlet face. The main and branch inlets have fully developed profiles for velocity and turbulence, which were obtained through supplementary periodic pipe flow simulations. The values of the velocity and temperature prescribed for the inlets are: Main pipe, $V_m = 1.46m/s$, $T_m = 321.15K$, and branch pipe, $V_b = 1m/s$, $T_b = 306.15K$ giving a temperature difference of $\Delta T = 15K$ for the mixing of the flows. The

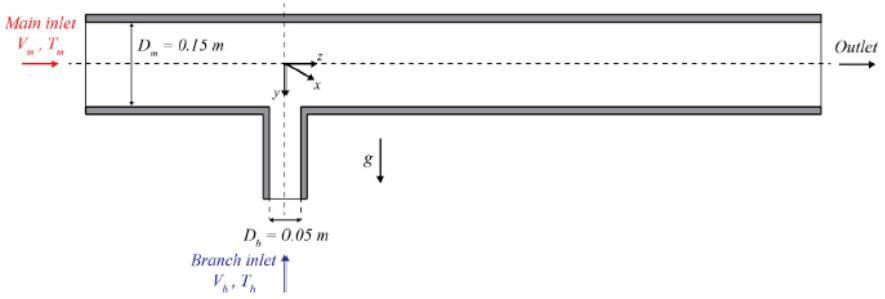

Figure 4.1: Geometry of the T-junction configuration used in the WALTON experimental facility

Reynolds number in the main pipe works out to be 326000.

The meshing implemented in the geometry uses unstructured polyhedral cells in the junction area, which are then extruded through the inlets and the outlet. The bulk polyhedral size is 0.003m. A boundary layer mesh is also implemented (prism layer mesher in Star-CCM+) to capture the large gradients expected within the boundary layer properly, while also giving a satisfactory resolution of the momentum and heat transfer close to the wall. The resulting mesh is shown below in Figure 4.2.

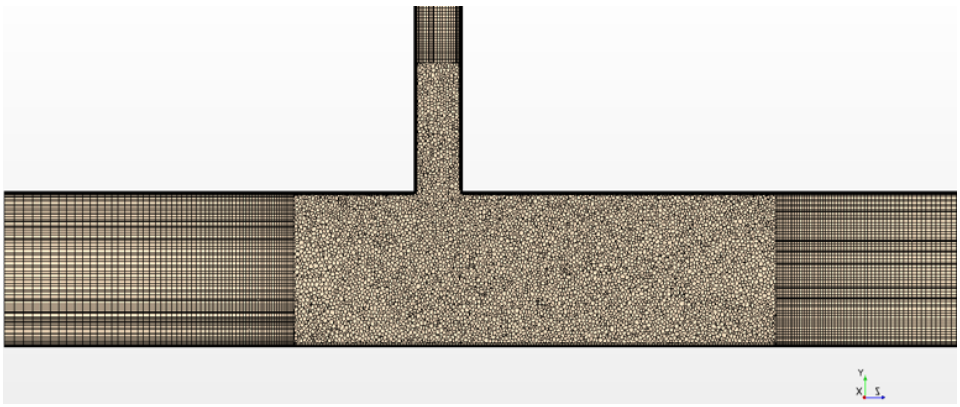

Figure 4.2: Mesh of the T-junction geometry according to [19]

For the validation work, it was decided to run simulations on Star-CCM+ using the Lien Linear low-Reynolds standard $k-\epsilon$ model, Lien Cubic low-Reynolds standard $k-\epsilon$ model, Linear $k-\omega$ SST-Menter model, and the Realizable $k-\epsilon$ model using both a wall-resolved and wall-function mesh. The mesh statistics for the boundary layer mesh for both these cases is given below in Table 4.1. The Lien Cubic low-Reynolds standard $k-\epsilon$ model is implemented in a URANS simulation with a second-order time-stepping scheme, a time step of 0.001s giving an average CFL ≈ 0.41.

Table 4.1: Mesh statistics of the boundary layer mesh implemented according to [19]

	Number of Layers	**Prism Layer Stretching**	**First Layer Size**	**Last Layer Size**	**Total Thickness**	**Average Wall y+**
Wall-resolved boundary layer	30	1.4	4.96e-08	0.000857	0.003	0.09
Wall-function boundary layer	7	1.125	0.001	0.002	0.01	47.75

The contour plots for the streamwise velocity (v_z) field are displayed below in Figure 4.3 for the five simulations run.

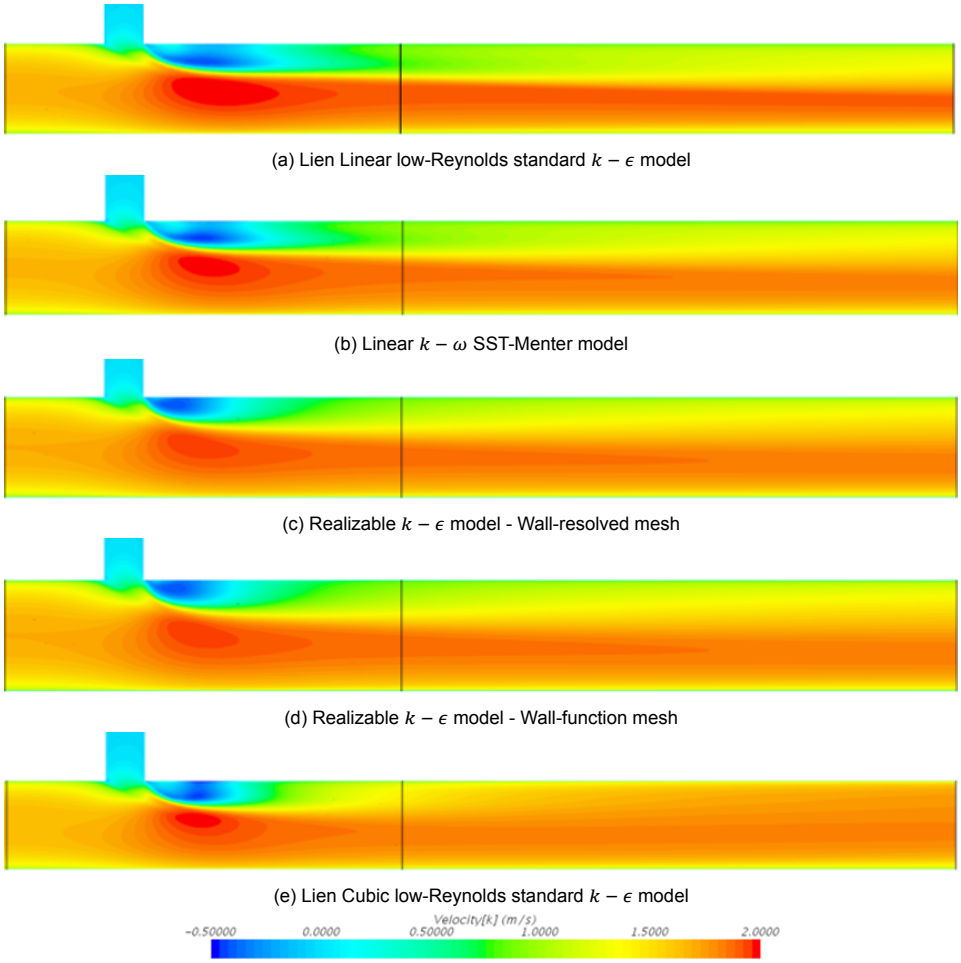

(a) Lien Linear low-Reynolds standard $k-\epsilon$ model

(b) Linear $k-\omega$ SST-Menter model

(c) Realizable $k-\epsilon$ model - Wall-resolved mesh

(d) Realizable $k-\epsilon$ model - Wall-function mesh

(e) Lien Cubic low-Reynolds standard $k-\epsilon$ model

Figure 4.3: Streamwise velocity (v_z) contours

Most of the models show a recirculation zone up to z = $1D_m$ in the near wake region downstream of the junction, which is consistent with experimental findings. The linear $k-\epsilon$ model shows a greater streamwise extent of this recirculation than the other models, followed by the linear $k-\omega$ SST model. The strength of mixing also seems to be diminished for the linear $k-\epsilon$ model, shown by higher streamwise velocity values in the middle of the pipe downstream of the junction. This may be due to the inability of the linear constitutive relation to predict the expected anisotropic turbulence in the region caused by the 3D mixing phenomenon. Conversely, for the cubic $k-\epsilon$ model, the mixing seems strongest due to the lower streamwise velocity values, highlighting the cubic constitutive relationship's strength in predicting the turbulence in the mixing region. The recirculation zone in the cubic $k-\epsilon$ model seems to be weaker and smaller in downstream extent. The realizable $k-\epsilon$ model for both the wall-resolved and wall-function mesh cases show good similarity to each other. The temperature contours of the five simulations are shown below in Figure 4.4.

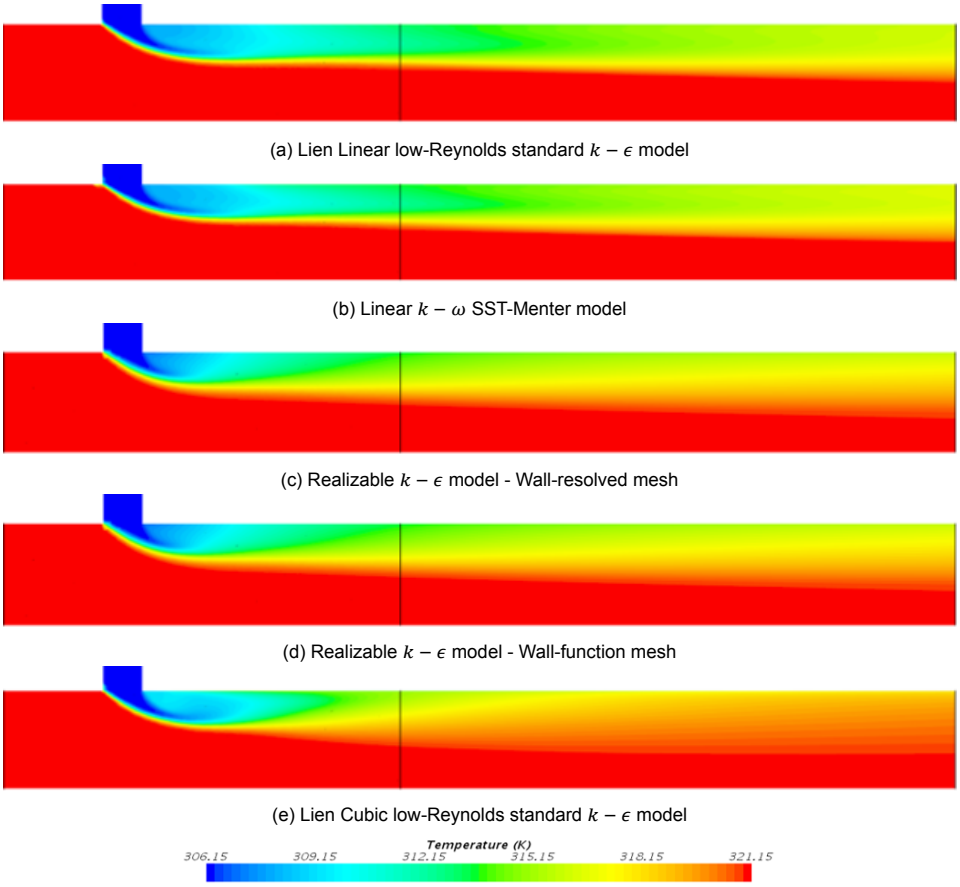

(a) Lien Linear low-Reynolds standard $k-\epsilon$ model

(b) Linear $k-\omega$ SST-Menter model

(c) Realizable $k-\epsilon$ model - Wall-resolved mesh

(d) Realizable $k-\epsilon$ model - Wall-function mesh

(e) Lien Cubic low-Reynolds standard $k-\epsilon$ model

Figure 4.4: Temperature (T) contours

The temperature contours corroborate what was seen in the streamwise velocity contours, where the cubic $k-\epsilon$ model shows greater mixing, and hence a larger area of higher temperature fluid downstream of the recirculation region, and as a result, higher temperatures closer to the upper wall of the pipe. The realizable $k-\epsilon$ model also shows good mixing judging by the higher values in the temperature contours in the middle of the pipe. The linear $k-\epsilon$ model predicts less mixing, and therefore a qualitatively lower temperature region near the upper wall in the wake of the recirculation region is observed. The effect of the longer recirculation bubble seen in the velocity contours is also observed in these lower temperature values.

Comparative plots with the experimental data and the results of the simulations run here are made for the streamwise velocity and temperature fields, at two downstream locations, $z = 0.5D_m$ and $z = 1D_m$. The streamwise velocity v_z is normalized with the value of the velocity in the main pipe ($V_m = 1.46m/s$). The temperature is normalized as $(T - T_b)/(T_m - T_b)$, where T_m = 321.15K and T_b = 306.15K are the fluid temperatures at the main and branch inlet pipes respectively.

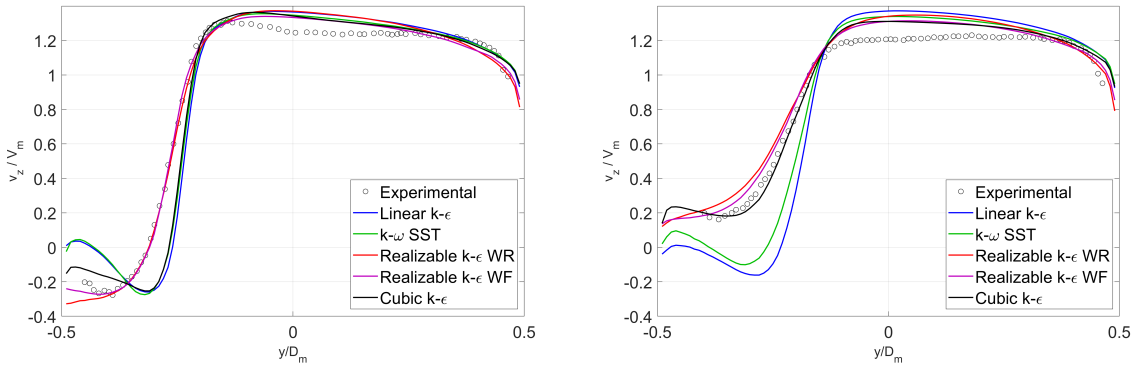

(a) $z = 0.5D_m$ (b) $z = 1D_m$

Figure 4.5: Calculated and experimental normalized streamwise velocity profiles

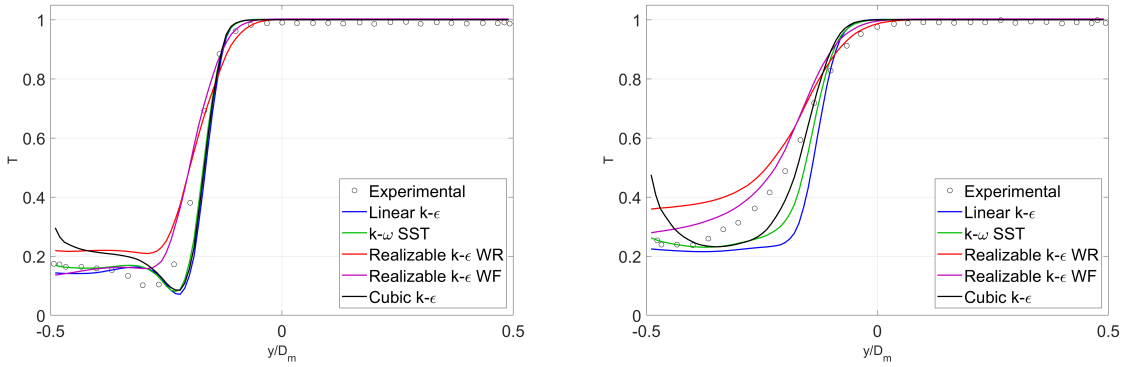

(a) $z = 0.5D_m$ (b) $z = 1D_m$

Figure 4.6: Calculated and experimental normalized temperature profiles

Analysing the trends shown in 4.5, it can be observed that the realizable $k-\epsilon$ simulations predict the trend better than the other models at the $0.5D_m$ downstream location, for the near-wall separation region (y/D_m = -0.25 to -0.5). Likewise, the cubic $k-\epsilon$ model shows the best agreement with the experimental values of the WALTON Facility for the separation region at the $1D_m$ downstream location. Both the linear $k-\epsilon$ model and the $k-\omega$ SST model over-predict the recirculation as seen in Figure 4.5 (more negative values of v_z for a larger wall-normal distance) at $1D_m$ downstream, while at $0.5D_m$ they indicate that the recirculation takes place further away from the wall but with the same intensity (at y/D_m = -0.3) with a small stagnation zone at the wall. This stagnation zone at the wall for $0.5D_m$ downstream is also seen in the cubic $k-\epsilon$ model profile. This is odd behaviour since the $k-\omega$ SST model is expected to show the best prediction in the presence of streamline curvature and separation regions. All models seem to over-predict the streamwise velocity values slightly in the middle of the channel (y/D_m = -0.2 to +0.2) compared to the experimental case, indicating the inability to accurately model the anisotropic turbulence associated with the 3D mixing phenomenon taking place here.

The temperature plots in Figure 4.6 show that at the $0.5D_m$ location, the realizable $k-\epsilon$ models over-predict the temperature fields in the separation region due to lesser recirculation, but the wall-function case shows good agreement with the experiment closer to the wall (y/D_m = -0.35 to -0.5). The other three models show a similar trend to the experiment in the separation zone here, albeit with the trough in the temperature values coming slightly further away from the wall, due to the stagnation seen in the behaviour of the streamwise velocity profiles. For the $1D_m$ location, the realizable models again over-predict the temperatures in the separation region (y/D_m = -0.25 to -0.5) and even at the wall, while the other three models under-predict these values because of the stronger recirculation observed. However, at and very close to the wall (y/D_m = -0.5), the $k-\omega$ SST model follows the experimental values

very well, with the linear $k-\epsilon$ model close as well. However, at and very close to the wall, the cubic $k-\epsilon$ model over-predicts the temperature values significantly. The profiles in the mixing region (y/D_m = -0.2 to +0.2) also vary according to the strength of the recirculation, i.e. stronger recirculation implies lower temperatures due to more mixing (also observed as lower streamwise values in this region) in the linear $k-\epsilon$ and $k-\omega$ SST models, while weaker recirculation gives higher temperatures because of less mixing as seen in the realizable $k-\epsilon$ models. Curiously, the cubic $k-\epsilon$ model predicts a weaker recirculation at $1D_m$ but also shows stronger mixing.

It is seen that none of the models agree in similar fashion with the experimental values in all four plots. Therefore, based on the knowledge from the literature survey and the general intrinsic properties of the turbulence models, it was thus decided to use the $k-\omega$ SST-Menter turbulence model for the entire RANS phase of the thesis.

4.2. Junction Corner Shape Calibration

From the literature analysed, it is seen that the junction corners used in reference experimental cases is either a sharp corner, or a corner with a radius of curvature $r_c = 18mm$. Sharp corners cause numerical cell connectivity issues at the corner (having 2 cells only at the corner) leading to numerical dissipation issues, and do not cause a physical flow connection between them at the interface. Therefore, sharp junction corners can present a stringent mesh requirement at the corner for a DNS calculation, increasing the total mesh size. Additionally, the small mesh elements at the corner may lead to high Courant numbers, resulting in smaller time-step size. Hence, the corners are made rounded to mitigate these numerical dissipation issues and computational time penalty. Thus, a calibration is first performed for the corner shape to check what is the maximum radius of curvature of the corner shape in the T-junction geometry that can be used to replace a sharp corner geometry while accurately reproducing the fundamental turbulence and thermal mixing phenomena.

The geometry to be used from this phase of the RANS calibration study is based on the Fatherino facility 3.1 experimental geometry. The diameters of both the main and branch pipes in this geometry are $0.054m$, while the inlet and branch pipes are of length 3D. The length of the outlet pipe is taken as 16D. The geometry is presented below.

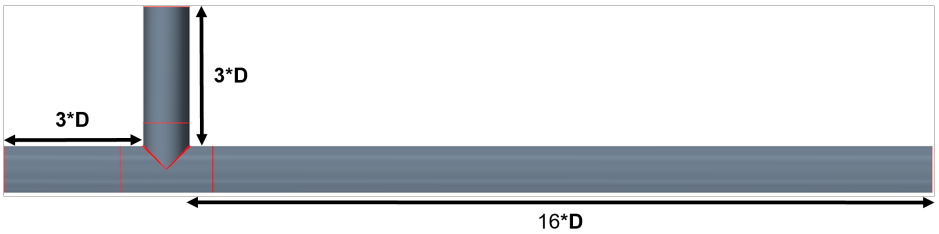

Figure 4.7: Geometry of the T-junction configuration used in the RANS simulations

From the turbulence model sensitivity study conducted previously, it was determined that the $k-\omega$ SST Menter turbulence model in Star-CCM+ will be used in the simulations. The Reynolds number at the inlet and the branch pipes are set as 11700, corresponding to the friction Reynolds number $Re_\tau = 360$ for pipe flows, while the Prandtl number is Pr = 1. The temperature of the fluid in the main pipe is 300K, and in the branch pipe is 315K. The mesh used involved unstructured polyhedral cells for the cells in the bulk region with a size of 0.001m, while a boundary layer mesher (prism layer mesh in Star-CCM+) was used to resolve the regions near the wall in order to better resolve the momentum and heat transfer close to the wall. The mesh statistics are presented in Table 4.2 below.

Table 4.2: Mesh statistics of the boundary layer mesh implemented in the corner shape calibration

	Number of Layers	Prism Layer Stretching	First Layer Size	Last Layer Size	Total Thickness	Average Wall y+
Wall-resolved boundary layer	12	1.289	6e-05	0.001	0.00425	0.771

A few sample images of the mesh created are shown below for 3D geometries using a sharp junction corner and a corner with radius r_c = 4mm.

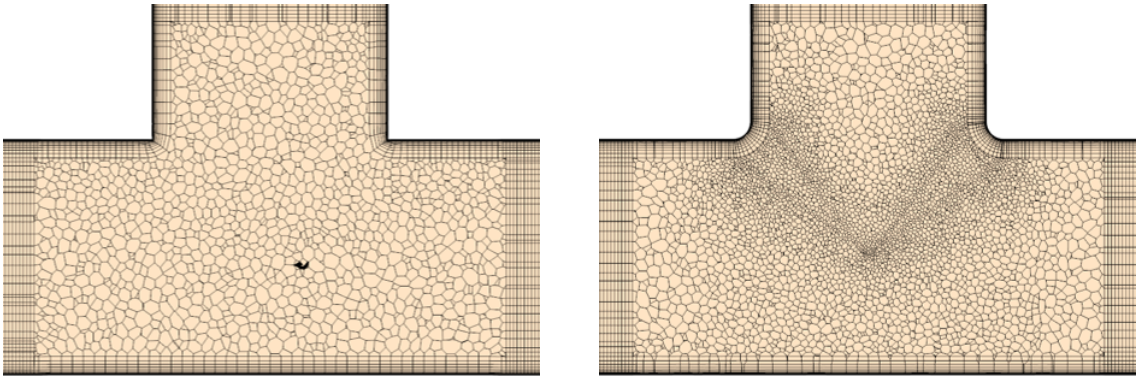

(a) Sharp corner mesh (b) $r_c = 4mm$ corner mesh

Figure 4.8: Images of the 3D geometry mesh created

The inlet, branch, and outlet regions are then meshed using an extruded mesh which is extruded from the polyhedral mesh in the junction region. Simulations are performed using different corner radii ranging from r_c = 1mm to 18mm (r_c/D = 0.02 to 0.33) taken from the geometries of the experimental facilities found in the literature. It should be noted that smaller values of corner radii would result in a significant increase in DNS mesh sizes, and are thus not investigated here.

4.2.1. 2D Simulations

Corner shape calibration was first done using 2D simulations to find the limit of flow unsteadiness shown by rounded corners. The corner radii used were r_c = sharp, 2, 4, 6, 8, 12 and 18mm. The streamwise velocity and temperature contours of the 2D simulations conducted are shown below in Figures 4.9 and 4.10.

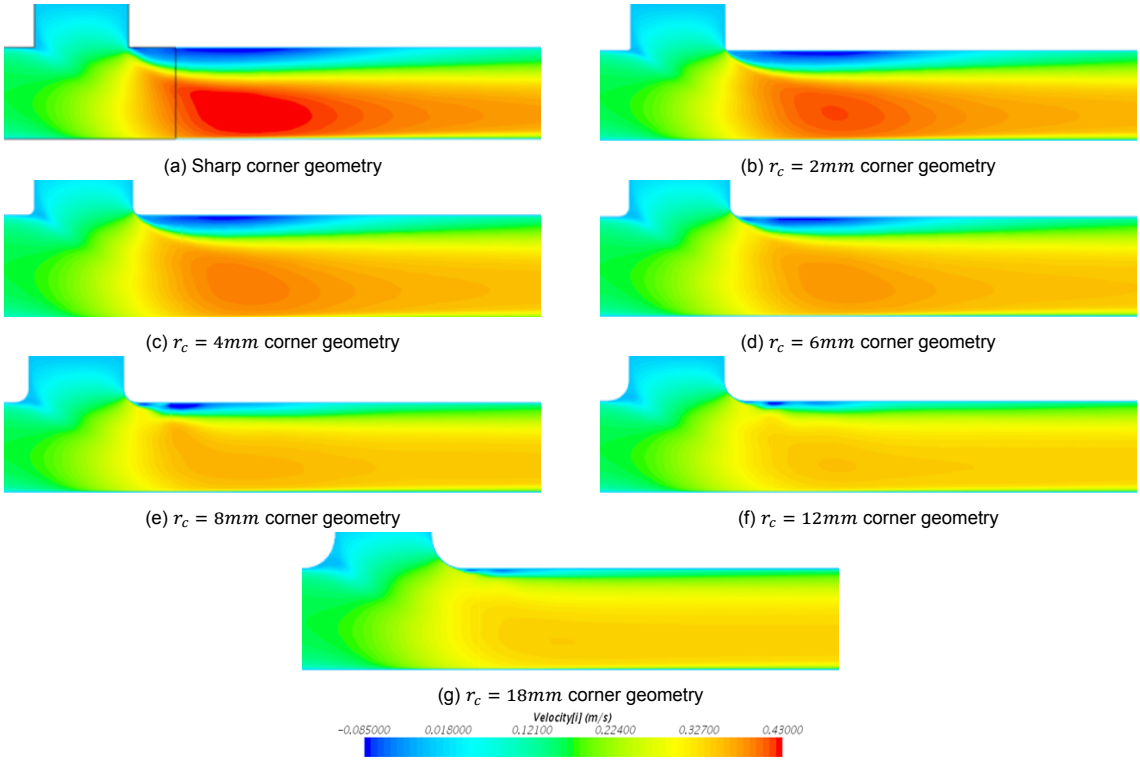

(a) Sharp corner geometry

(b) $r_c = 2mm$ corner geometry

(c) $r_c = 4mm$ corner geometry

(d) $r_c = 6mm$ corner geometry

(e) $r_c = 8mm$ corner geometry

(f) $r_c = 12mm$ corner geometry

(g) $r_c = 18mm$ corner geometry

Figure 4.9: Streamwise velocity contour plots of the 2D corner shape calibration simulations

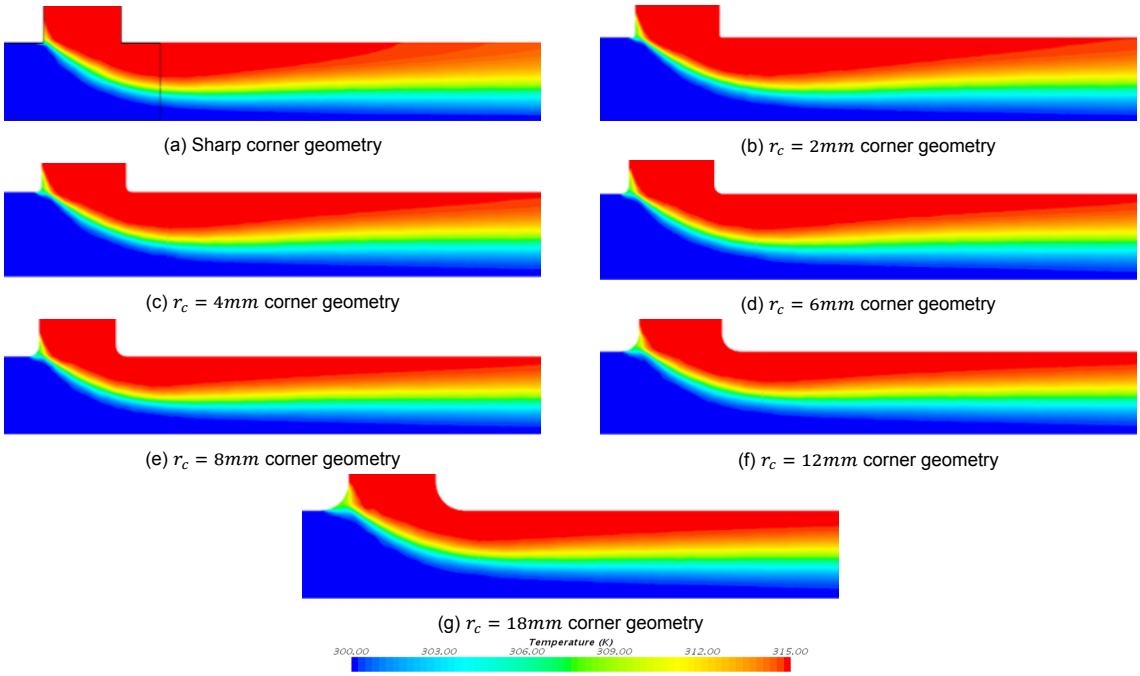

(a) Sharp corner geometry

(b) $r_c = 2mm$ corner geometry

(c) $r_c = 4mm$ corner geometry

(d) $r_c = 6mm$ corner geometry

(e) $r_c = 8mm$ corner geometry

(f) $r_c = 12mm$ corner geometry

(g) $r_c = 18mm$ corner geometry

Figure 4.10: Temperature contour plots of the 2D corner shape calibration simulations

A stronger recirculation region is observed in the sharp corner case compared to the other corner cases in Figure 4.9. There is a small stagnation point found on the upstream corner (left) of the junction which increases with the radius of the corner. The radius of the corner affects the size of the recirculation zone downstream of the junction. The larger curvature allows the fluid to flow more smoothly, reducing the gradient formed and therefore also the separation that would occur at the junction. The velocity monitors that were set-up for different downstream locations in the outlet pipe showed fluctuations in

the velocity profiles closer to the junction (at the recirculation zone) for all cases with $r_c \geq$ 6mm the R = 6mm case. This implied that 2D simulations were unable to give a converging steady-state solution for these geometries. From these 2D simulations, simulations with r_c up to 4mm show similar flow behavior to the sharp corner.

4.2.2. 3D Simulations

The 2D simulations show that the r_c = 4mm case is the maximum the corner radius can be while showing similarities in the flow features with the sharp corner case. 3D simulations are now carried out for corner radii r_c = 1mm, 2mm and 4mm and compared to a sharp corner 3D simulation to analyse the temperature and streamwise velocity contours. These contours are presented below.

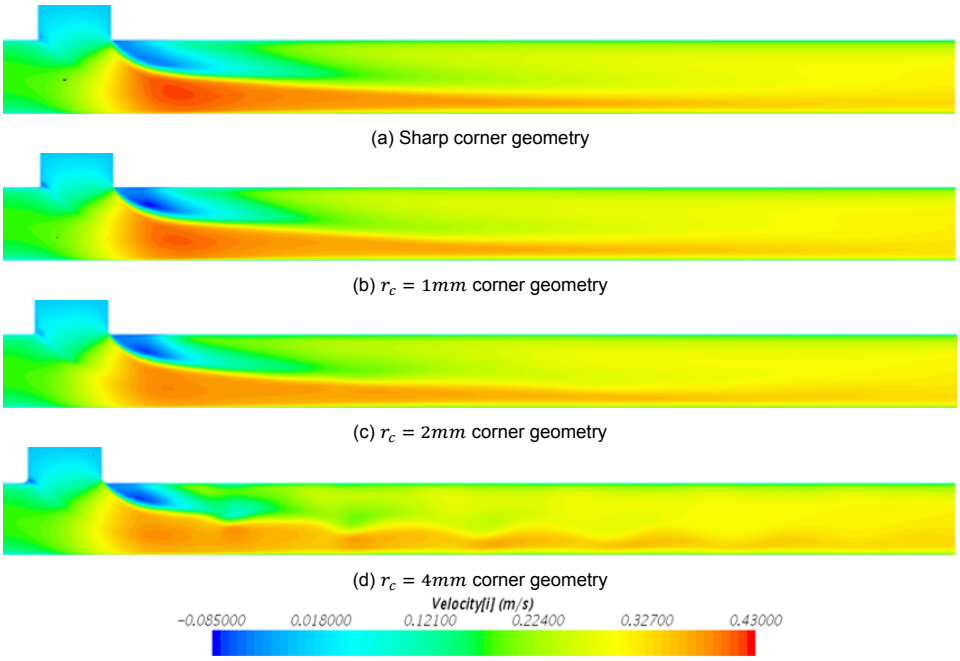

(a) Sharp corner geometry

(b) $r_c = 1mm$ corner geometry

(c) $r_c = 2mm$ corner geometry

(d) $r_c = 4mm$ corner geometry

Figure 4.11: Streamwise velocity contour plots of the 3D corner shape calibration simulations

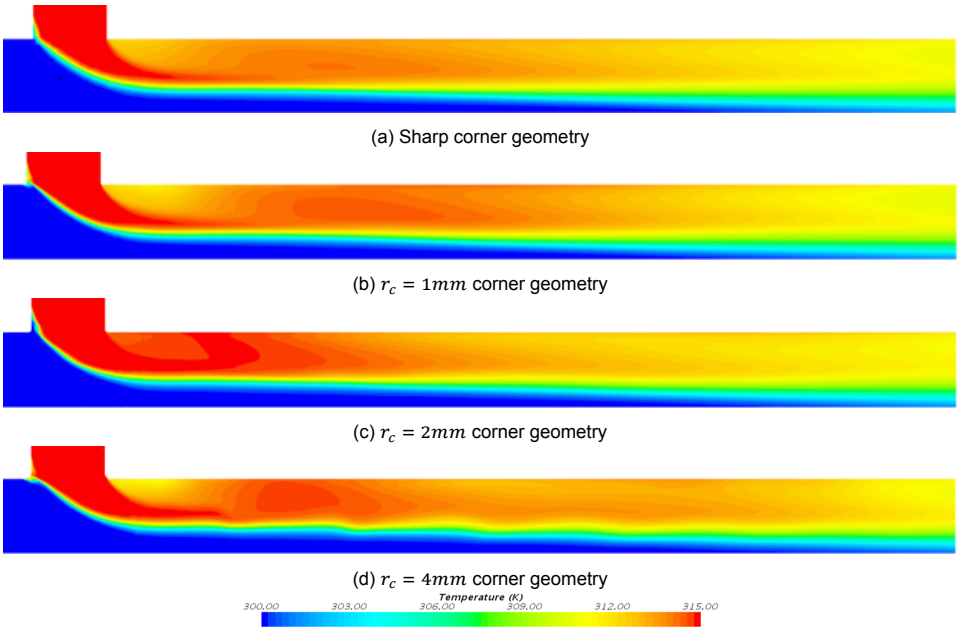

(a) Sharp corner geometry

(b) $r_c = 1mm$ corner geometry

(c) $r_c = 2mm$ corner geometry

(d) $r_c = 4mm$ corner geometry

Figure 4.12: Temperature contour plots of the 3D corner shape calibration simulations

The corner radius does not seem to influence the upstream stagnation zone in 3D simulations as much as they did in the 2D simulations, and are smaller in the 3D simulations. The separation region strength decreases slightly with an increase in the curvature radius. The strength of the mixing increases with an increase in corner curvature, shown by the decrease in the streamwise velocity values in the middle of the pipe downstream of the junction (mixing is 3D). Additionally, the 3D simulation monitors set up showed that the 4mm case is characterized by unstable/fluctuating behavior at downstream locations close to the wall. There were smaller fluctuations in the monitors of the 2mm case as well. These fluctuations were not seen in the corresponding 2D simulation. For this reason, the use of 2D simulations do not predict well the important flow mixing and recirculation phenomena that need to be studied. It is observed that the corner radius of r_c = 1mm and 2mm (r_c/D = 0.02 and 0.04) resulted in a reasonable depiction of the phenomena observed in sharp corner geometry. At higher radii of curvatures, the flow appears to exhibit transient features. Thus, a radius of r_c = 1mm (r_c/D = 0.02) is selected for next RANS simulations and the UDNS case set up.

4.3. Reynolds Scaling Tests

Experimental reference cases contain information for the T-junction mixing phenomena which are run at high values of Reynolds numbers, values that make it too expensive to reproducing numerically. To combat this computational time cost, an investigation is made into the scaling down of the Reynolds numbers, ensuring that the fundamental turbulence and thermal mixing flow features of a T-junction that are observed at higher Reynolds numbers are similar to those at lower, computationally-feasible values. To perform this scaling test, RANS simulations are conducted at values of Re = 20000, 40000 and 60000 (corresponding to values used in the Fatherino experimental facility mentioned in Table 3.1), and also at values of Re = 5300, 9100 and 11700 (corresponding to friction Reynolds numbers of Re_τ = 180, 290 and 360), which are commonly found in reference numerical databases of pipe flows [33]. An additional case was also run at Re = 30000, for the purposes of this study. Here, the Reynolds numbers are based on the diameter of the pipe ($0.054m$), and the bulk velocity at the inlet and the branch pipes (u_b); $Re = u_b D/\nu$ and $Re_\tau = u_\tau D/\nu$.

The geometry used in the simulations consisted of a 18D outlet pipe length from the center of the junction, while the inlet and branch pipes were 3D in length not including the recycling inlet length. The mesh implemented was based on the meshing scheme of Mesh 2 from the mesh sensitivity study presented later (Section 4.5). The salient parameters of the meshes implemented in the different simulations are tabulated below in Table 4.3.

Table 4.3: Mesh parameters for the meshes used in the Reynolds scaling

Reynolds Number	**5300**	**9100**	**11700**	**20000**	**30000**	**40000**	**60000**
Bulk Size	0.001	0.0008	0.00067	0.000475	0.00045	0.0004	0.00035
Boundary Layer Mesh							
First cell size, a_0	1.19E-04	7.45E-05	0.00006	3.75E-05	2.64E-05	2.05E-05	1.44E-05
Last cell size, a_n	0.001	0.0008	0.00067	0.000475	0.00045	0.0004	0.00035
Number of Prism Layers, n	10	13	16	22	23	23	25
Prism Layer Stretching, r	1.271	1.210	1.170	1.124	1.139	1.146	1.143
Prism Layer Thicnkess, S_n	0.00425	0.00425	0.00425	0.004	0.0035	0.003	0.0027
Total Number of Cells	1499350	2866608	4421894	10481874	12430230	15848176	22050415

The following figures show the meshes of the different simulations at the junction region.

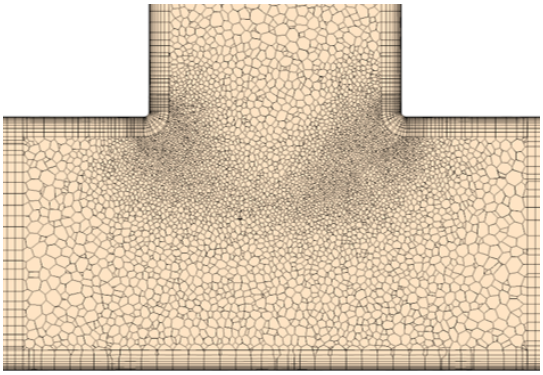

(a) Reynolds number = 5300

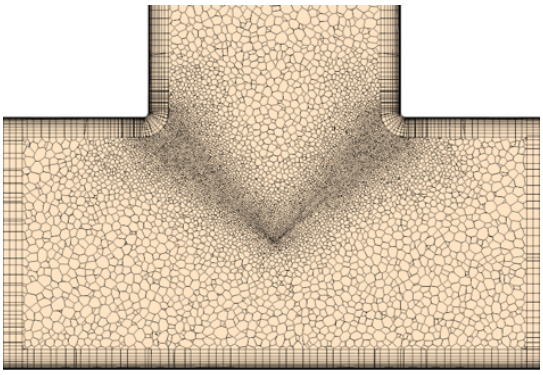

(b) Reynolds number = 9100

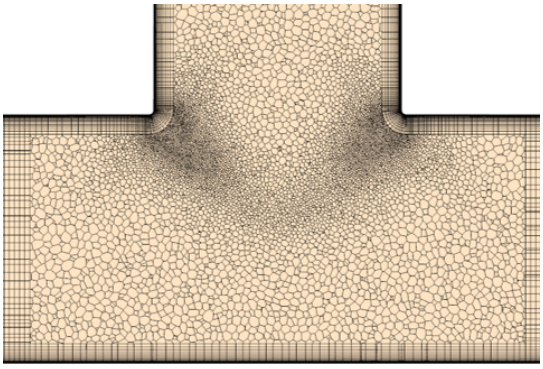

(c) Reynolds number = 11700

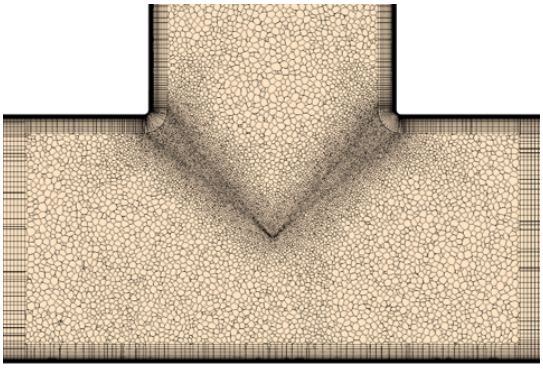

(d) Reynolds number = 20000

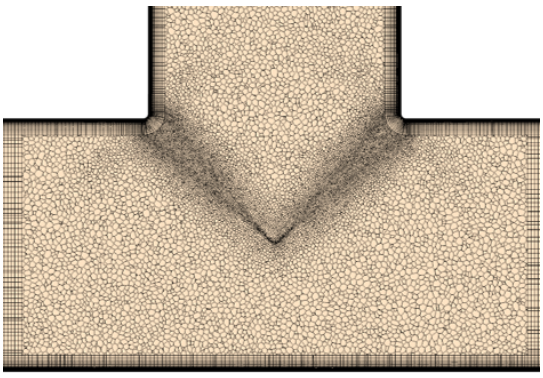

(e) Reynolds number = 30000

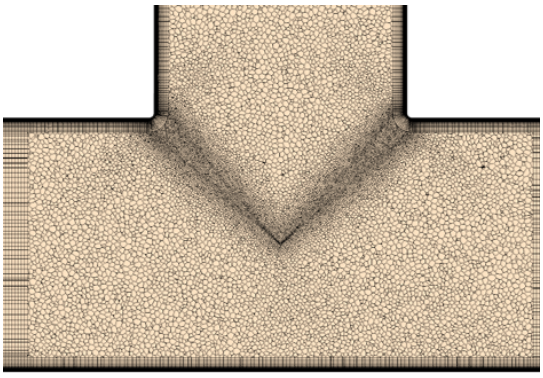

(f) Reynolds number = 40000

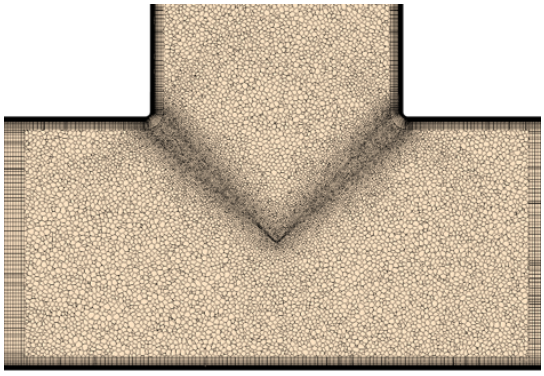

(g) Reynolds number = 60000

Figure 4.13: Mesh images for the Reynolds Scaling Simulations

All simulations converged properly and yielded steady-state solutions without any fluctuations in the monitors set up. The contours of the streamwise velocity component and the temperature fields are extracted from the simulation and presented below in Figures 4.14 and 4.15 below. The contours are taken only until 12D downstream of the junction, as beyond this location, major changes are not expected. These contours give a qualitative view of the respective fields across the different Reynolds numbers. Analysing these plots shows that the general trend of the contours look similar across the simulations. There seem to be no discernible differences beyond a slight decrease in intensity of the streamwise velocity in the mixing region (middle of the pipe downstream of the junction, the red regions in the contour plots reduce in intensity) with an increase in the Reynolds number. The recirculation zone on the top wall of the outlet pipe immediately downstream of the junction shows a similar intensity in all the contour plots. In the temperature contour plots, there is also no discernible differences across the simulations. However, a qualitative analysis of the contours on its own cannot give a full picture of the ability to scale down the Reynolds number for a T-junction thermal mixing simulation. A quantitative view is also needed to establish trends and make a good judgement.

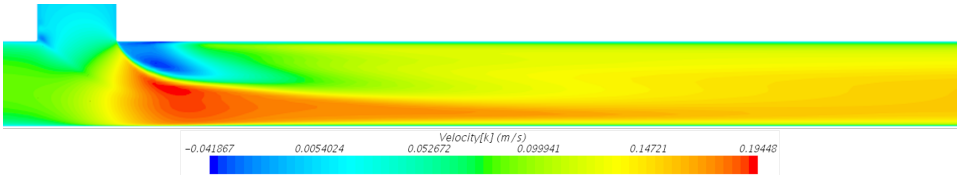

(a) Reynolds number = 5300

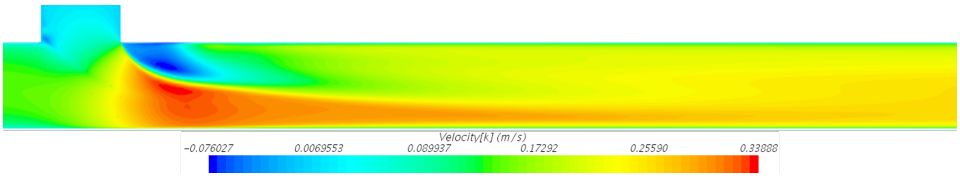

(b) Reynolds number = 9100

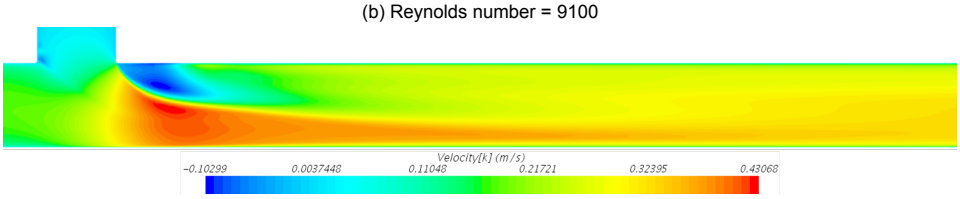

(c) Reynolds number = 11700

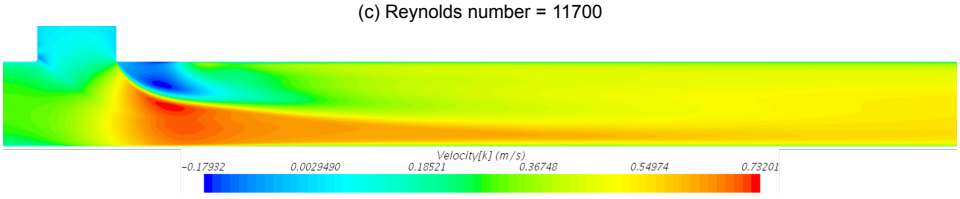

(d) Reynolds number = 20000

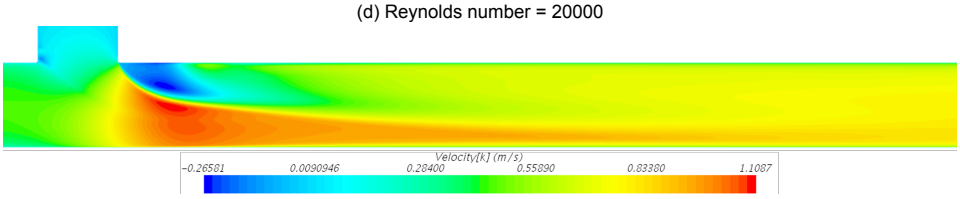

(e) Reynolds number = 30000

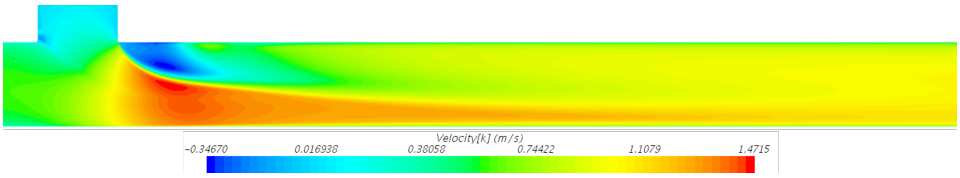

(f) Reynolds number = 40000

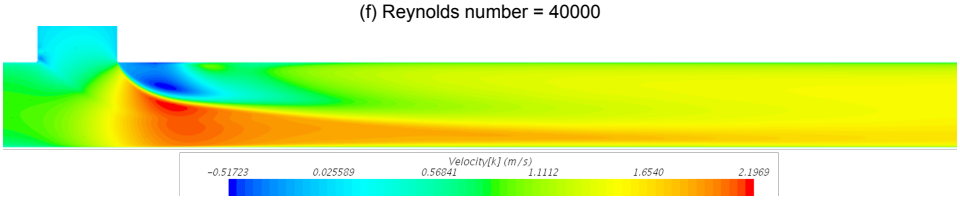

(g) Reynolds number = 60000

Figure 4.14: Contours of the streamwise velocity component (u_z)

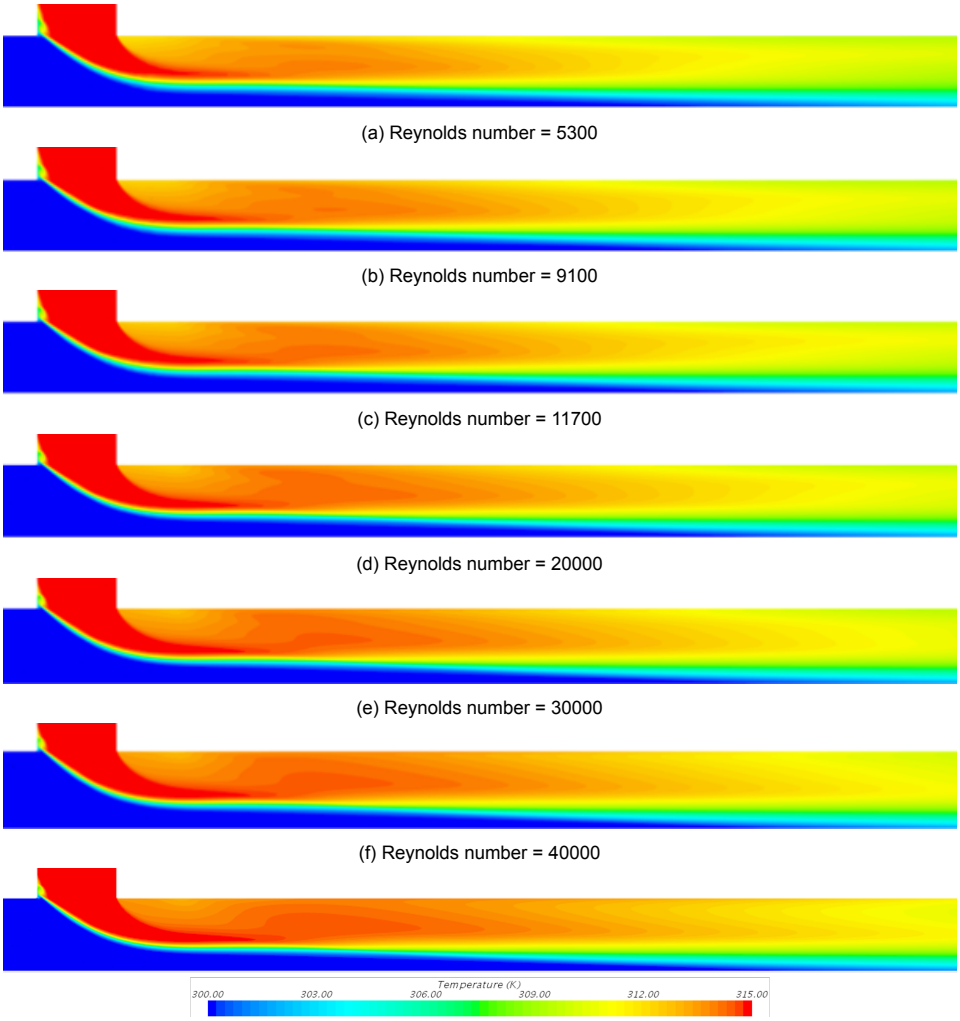

(a) Reynolds number = 5300

(b) Reynolds number = 9100

(c) Reynolds number = 11700

(d) Reynolds number = 20000

(e) Reynolds number = 30000

(f) Reynolds number = 40000

(g) Reynolds number = 60000

Figure 4.15: Contours of the temperature field (T)

As observed from the qualitative analysis of the contour plots of the streamwise velocity and temperature fields, a supplementary quantitative view of these fields is necessary to firmly make conclusions for this Reynolds scaling test. Therefore, as part of this quantitative analysis, the streamwise velocity and temperature field values were taken at multiple locations downstream of the junction, and the results were plotted together with the data taken at corresponding locations from the other simulations. However, the field values have to be normalized for the comparison since the simulations are run at different Reynolds numbers. The normalization for the streamwise velocity and temperature fields are done as stated below:

$$U^* = \frac{u_z}{u_{bulk}} \tag{4.1}$$

$$T^* = \frac{(T - T_{low})}{(T_{high} - T_{low})} \tag{4.2}$$

Here, the velocity is normalized with u_{bulk}, which is the value of the bulk velocity in the outlet pipe (the bulk velocity is the average flow velocity over a cross-section). The temperature is normalized between zero and unity, where $T_{high} = 315K$ and $T_{low} = 300K$ are the fluid temperatures at the branch and main inlet pipes respectively. The profiles at each location were taken from a line probe traversing from the bottom wall of the outlet pipe (y/D = -0.5) to the top wall of the outlet pipe (y/D = +0.5), moving through the diameter of the radial cross-sections at 0.5D, 1D, 2D, 4D, 8D and 11D distances downstream of the T-junction center. The resulting normalized comparative profiles for the streamwise velocity and temperature fields are shown below in Figures 4.16 and 4.17.

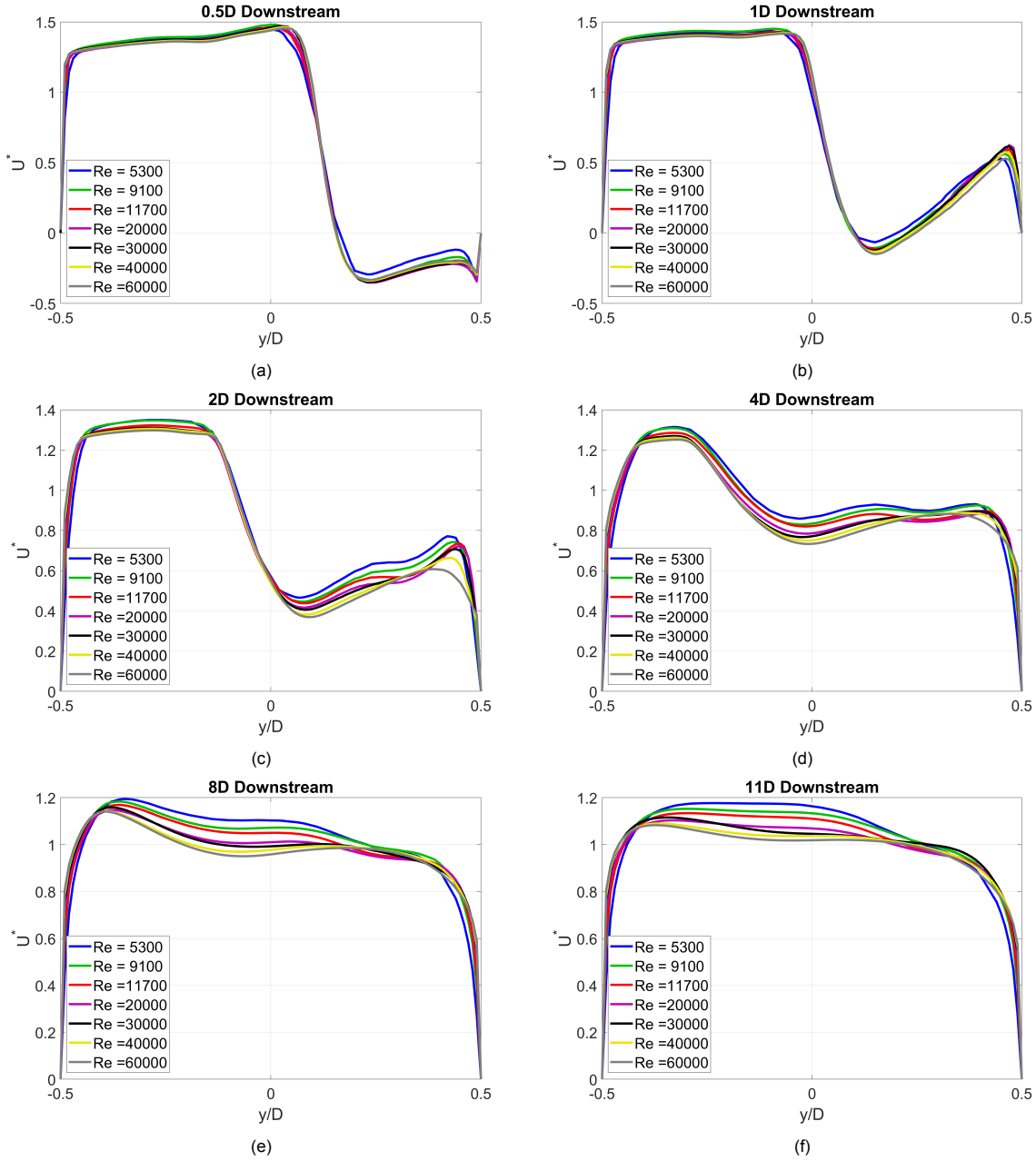

Figure 4.16: Normalized Streamwise velocity (U^*) comparative plots

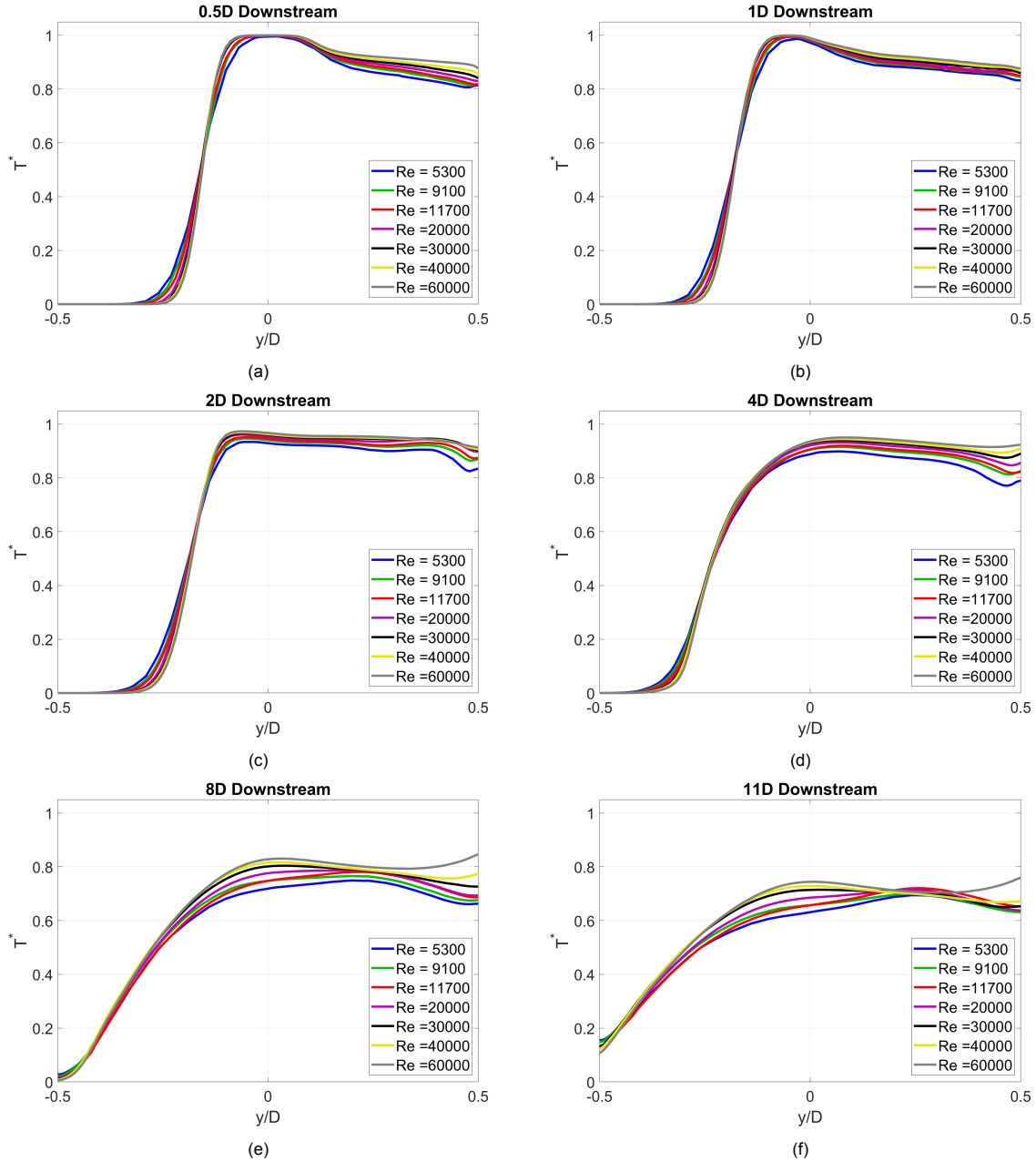

Figure 4.17: Normalized Temperature ($T*$) comparative plots

The quantitative plots offer a much deeper insight into the differences across the simulations, although the magnitude of the differences are not too high. In general, it can be noted that the strength of the 3-D mixing phenomenon increases slightly with an increase in the Reynolds number of the flow. As the Reynolds number increases, the streamwise velocity values show a decreasing trend in the mid-channel region (-0.2 y/D to +0.2 y/D) at 2D, 4D, 8D and 11D downstream locations (Figures 4.16c-4.16f). Since these are the locations where a majority of the fluid mixing is expected to take place, and since mixing is a 3-D phenomenon, it results in decreased streamwise velocity values. Additionally, the strength of the recirculation/separation zone (+0.2 y/D to +0.5 y/D) seems to increase with Reynolds numbers as well as the streamwise velocity values are decreasing, when moving downstream of the junction from 0.5D to 2D (Figures 4.16a-4.16c).

Looking at the normalized temperature profiles across the simulations, the temperature at the top wall (+0.4 y/D to +0.5 y/D) increases with an increase in the Reynolds number for almost all the locations

except 11D (Figures 4.17a-4.17e). This could be explained by the stronger separation zone caused by increasing Reynolds number, leading to lesser mixing allowing temperatures to stay higher in these areas. A curious behaviour is seen in the temperature plot at the 11D downstream position (Figure 4.17f), where a slightly increased value of temperature is seen approximately between 0.25D and 0.3D for Re = 5300, 9100, and 11700 compared to the other cases. This implies that there is a relatively larger amount of mixing here possibly due to the less intense separation zone upstream causing the flow to begin ”re-attaching” to the top wall unlike in the higher Reynolds number cases. For the mid-channel region (-0.2 y/D to +0.2 y/D), the effects of greater mixing (also corroborated by the streamwise velocity plots) leads to increasing temperature values here since the hot fluid enters from the branch pipe.

An extremely fine analysis into the plots reveal marginal differences in both the flow and thermal fields in and around the upper wall of the outlet pipe. However, the general phenomena of flow separation, recirculation and thermal mixing in the outlet pipe are observed and show great similarity between all the Reynolds number cases simulated. Therefore, it can be concluded that the scaling of the Reynolds number from experimental values down to computationally less expensive values is feasible, which can then be implemented in a DNS calculation. An inlet Reynolds number of Re = 5300 ($Re_\tau = 180$) is chosen for the UDNS case set up for this purpose.

4.4. Pipe Length Optimization

Now that it is known that the Reynolds number of the simulations can be scaled down from the high values found in the reference experimental cases (Table 3.1) to lower, more feasible values for computational simulations, such as Re = 5300, 9100, 11700 corresponding to pipe flow friction Reynolds numbers Re_τ = 180, 290, 360 respectively, the geometry to be used for the proof-of-concept under-resolved DNS test case needs to be finalised. For a fully-developed flow to be produced and used at the inlets of the geometry, a recirculating region of additional length equal to 5 times the diameter of the pipe is required (5D) [34]. These recirculating regions, once fully developed, are input on to the inlet faces of both the branch and main inlets of the T-junction geometry. An optimization study on the pipe lengths of both the inlets, and also the outlet of the T-junction is performed.

For the inlet and the branch pipes, this is done to ensure that the flow development from the inlet region does not affect the thermal mixing in the junction. To check how far upstream from the junction we have to go to notice a significant difference in the flow fields, the radial line profiles of these fields at multiple upstream positions are compared and the difference between the values is quantified after normalization. This is done for both the main inlet and branch pipes. For the outlet pipe length, the length is finalized based on whether the pressure outlet has a significant effect on the profiles at locations upstream of the outlet. This also shows us how far downstream of the junction do the effects of the T-junction’s turbulent mixing propagate. The Reynolds number used in the simulations is 11700. The meshing strategy implemented for the geometry follows that of Mesh 2, which is discussed later in the report in Section 4.5. This mesh uses boundary layer cells near the walls to control the wall cell size and its growth into the bulk, while the bulk cells comprise polyhedral cells in the junction region, transforming into directed mesh cells (Star-CCM+ setting) in the inlet pipes and outlet. A close-up of this mesh in the junction region is shown below in Figure 4.18.

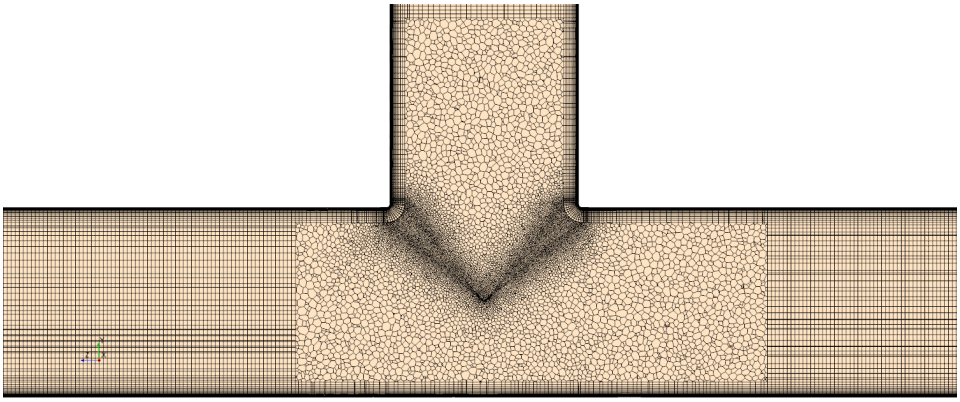

Figure 4.18: Mesh at the junction for Pipe Length Determination studies, implemented using the Mesh 2 strategy

4.4.1. Inlet Length Optimization

To carry out the inlet length optimization study, a T-junction geometry with a length of 6D upstream from the junction (excluding recycling length) was created for both the main and branch pipes. The profiles (line profile running as a diameter from the top wall to the bottom wall at the radial cross-section at each location) of the streamwise velocity (u_z), turbulence kinetic energy, and turbulent viscosity fields were compared at different locations upstream of the junction. Figures 4.19a-4.19c show the profiles of the three fields at the different upstream locations. It can be seen that the difference between the 0D profile and the rest of the profiles is very discernible, followed by the 0.5D profile showing a very small difference. This can be attributed to the upstream effects caused by the mixing of the flows in the junction which is closest to these 2 locations. However, the other upstream positions show profiles that overlap completely. which is also seen in the relative difference values tabulated.

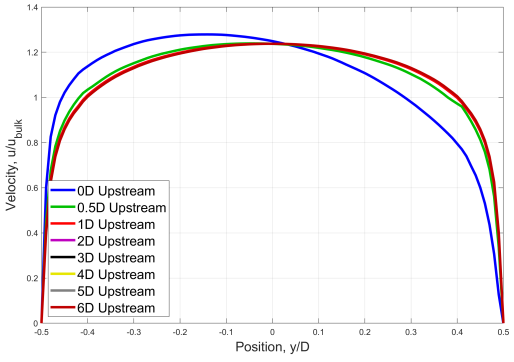

(a) Streamwise Velocity profile comparison

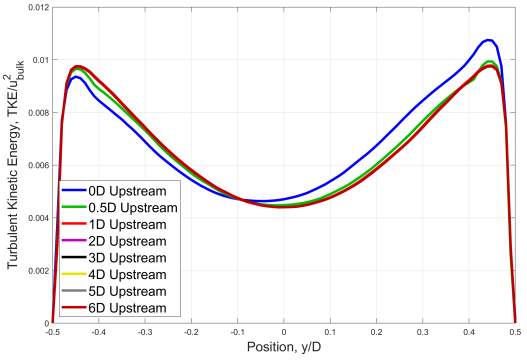

(b) Turbulence Kinetic Energy profile comparison

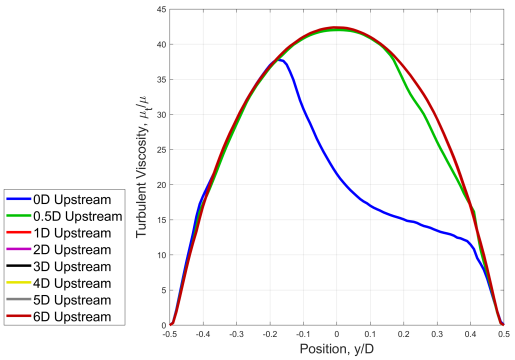

(c) Turbulent Viscosity profile comparison

Figure 4.19: Profile comparisons between upstream locations for the inlet pipe

The difference in the profiles of the fields at each upstream location were compared to the profile at 6D upstream (just at the start of the inlet, after the recycling length ends) and expressed as the relative error between them, in percentages. The values expressed in the table are effectively the relative difference in the area under each plot with respect to the plot for the 6D upstream location for each field. These values can be seen below in Table 4.4 below:

Table 4.4: Relative difference (as %) with respect to the profile at 6D upstream - Inlet pipe

	Upstream Location						
Field	**0D**	**0.5D**	**1D**	**2D**	**3D**	**4D**	**5D**
Streamwise Velocity	9.91	1.95	0.41	1.7×10^{-2}	1.2×10^{-3}	8.3×10^{-4}	7.5×10^{-4}
Turbulence Kinetic Energy	8.73	2.08	0.4	0.02	3.2×10^{-3}	2.2×10^{-3}	1.4×10^{-3}
Turbulent Viscosity	33.98	2.69	0.16	4.3×10^{-3}	1.8×10^{-3}	1.5×10^{-3}	1×10^{-3}

Figure 4.20 shows the percentage change in the three flow fields at different upstream locations in the inlet, plotted using the values displayed in Table 4.4. An analysis into the figures above and the one below combined with the values presented in the table above, an inlet length of 2D upstream from the junction seems to be adequate enough to ensure that there is no interference by the flow development from the recycling inlet region on the thermal mixing in the junction. A margin of safety is added to this length, giving rise to a final optimized total inlet length of 3D, excluding the separate recycling length.

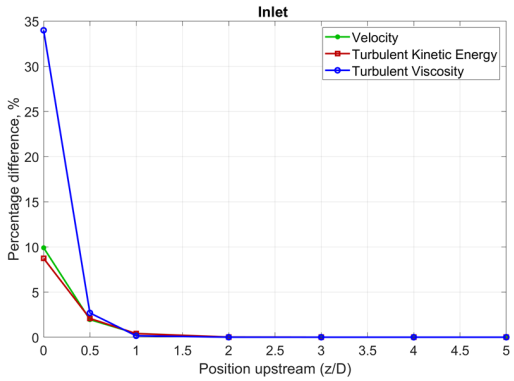

Figure 4.20: Comparative profile differences at different upstream positions for the inlet pipe

4.4.2. Branch Length Optimization

Similar to the inlet length optimization process, a 6D upstream length branch geometry was simulated (excluding recycling length). Again, the profiles of the streamwise velocity (u_y), turbulence kinetic energy, and turbulent viscosity fields were compared at different locations upstream of the junction and are shown in Figures 4.21a-4.21c. The 0D profile shows a significant difference to the rest of the profiles as expected, due to its proximity to the junction. The 0.5D profile behaves similarly to the inlet pipe profile as well, although the turbulent viscosity at this upstream location in the branch pipe (Figure 4.21c) shows a far greater deviation than the corresponding profile in the inlet pipe (Figure 4.19c). This lack of similarity between the inlet and branch profiles for a similar upstream distance (0D, 0.5D) is because the mixing of the flows at the junction induces a different effect on the branch pipe, where the fluid flowing in the -y direction in the branch pipe gets sucked by and mixes with the +z flow from the main inlet, joining to flow towards the outlet. The other upstream profiles overlap completely with each other.

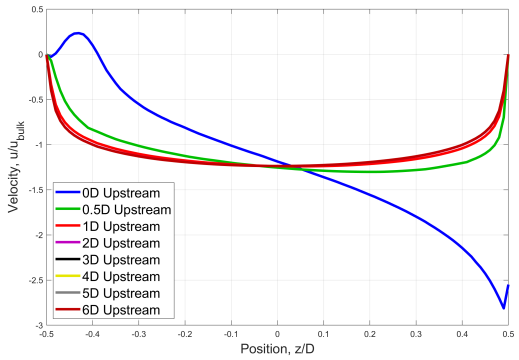

(a) Streamwise Velocity profile comparison

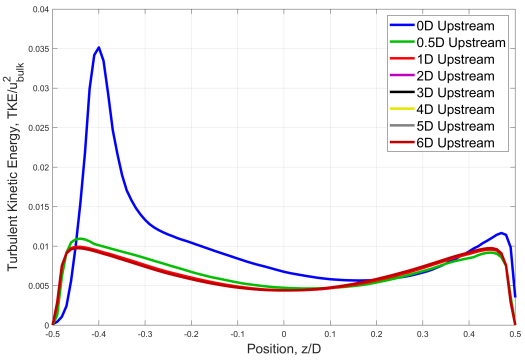

(b) Turbulence Kinetic Energy profile comparison

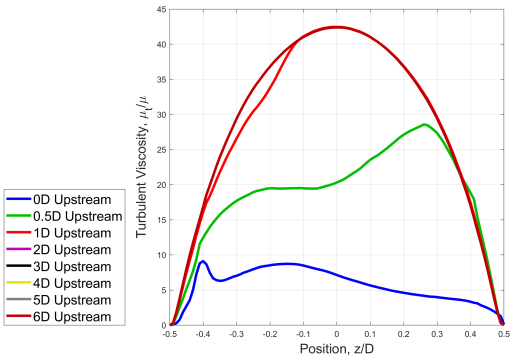

(c) Turbulent Viscosity profile comparison

Figure 4.21: Profile comparisons between upstream locations for the branch pipe

Again, the difference in the profiles of the fields at each upstream location were compared to the profile at 6D upstream and expressed as the relative error between them, in percentages. These values can be seen below in Table 4.4 below. It confirms what was seen visually in the profile comparison plots above, where the profiles show significant differences up until 1D upstream, beyond which the values are negligible.

Table 4.5: Relative difference (as %) with respect to the profile at 6D upstream - Branch pipe

	Upstream Location						
Field	**0D**	**0.5D**	**1D**	**2D**	**3D**	**4D**	**5D**
Streamwise Velocity	54.56	11	2.29	0.1	7.66×10^{-3}	3.69×10^{-3}	3.52×10^{-3}
Turbulence Kinetic Energy	61.22	9.77	2.31	0.1	4.36×10^{-3}	2.29×10^{-4}	5.35×10^{-5}
Turbulent Viscosity	80.6	37.24	2.66	0.027	1.17×10^{-3}	5.02×10^{-5}	2.14×10^{-6}

The percentage change in the three flow fields at different upstream locations in the branch pipe are plotted using the values displayed in Table 4.4 and shown in Figure 4.22). The figure and the tabulated values confirm that for the branch pipe, a length of 2D upstream from the junction does the trick when it comes to avoiding any interference on the thermal mixing in the junction by the flow development from the recycling inlet. A 1D margin of safety is added again, leading to a final optimized total branch pipe length of 3D (excluding the separate recycling length), just like in the main inlet pipe case.

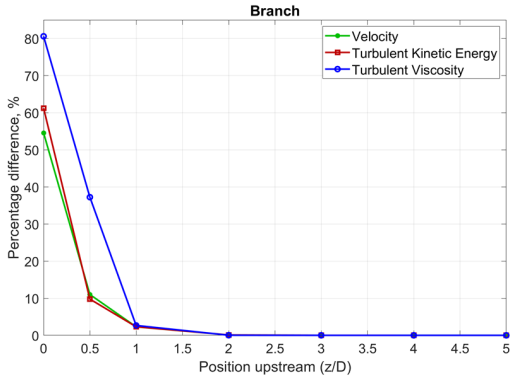

Figure 4.22: Comparative profile differences (percentage) at different upstream positions for the branch pipe

4.4.3. Outlet Length Optimization

To study the extent of influence of the junction mixing downstream of the junction, multiple simulations were carried out, using different outlet lengths such as 12D, 13D, 14D, 15D and 16D downstream of the junction. The inlet and branch lengths were taken as 6D upstream from the junction, as was determined by the studies carried out previously. The differences in the fields of streamwise velocity u_z, temperature and turbulence kinetic energy at 4 locations downstream of the T-junction were compared for each simulation with respect to the corresponding values of the 16D outlet length simulation. These locations were 8D, 10D, 11D and 12D downstream.
Figures 4.23-4.25 show the profiles of the three fields for the four outlet length simulations run at the locations 8D, 10D and 12D downstream of the junction. It can be seen that the difference in the profiles is extremely negligible, which will also justified by the values shown in the relative error table presented later.

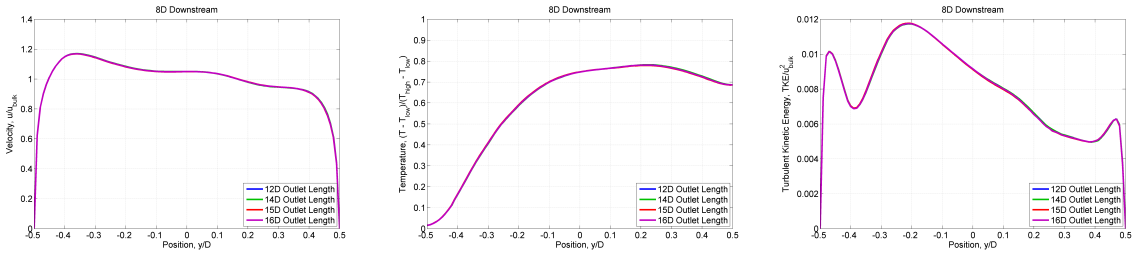

(a) Streamwise Velocity (b) Temperature (c) Turbulence Kinetic Energy

Figure 4.23: Profile comparisons between simulations at the 8D downstream location

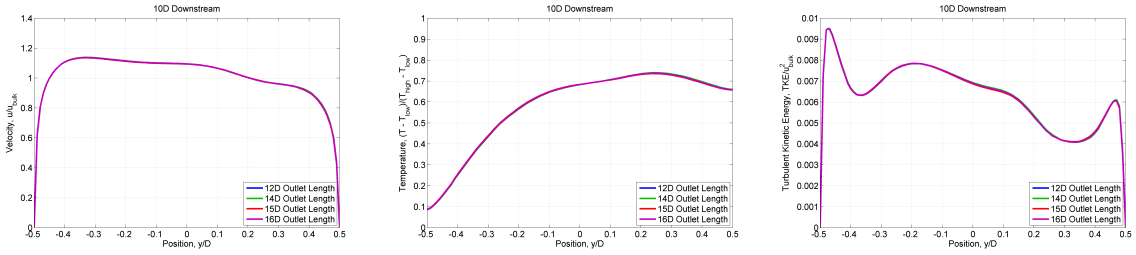

(a) Streamwise Velocity (b) Temperature (c) Turbulence Kinetic Energy

Figure 4.24: Profile comparisons between simulations at the 10D downstream location

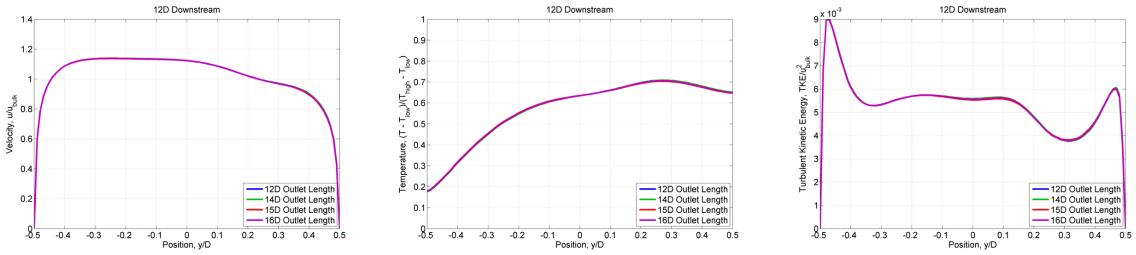

(a) Streamwise Velocity (b) Temperature (c) Turbulence Kinetic Energy

Figure 4.25: Profile comparisons between simulations at the 12D downstream location

The difference between the values of the fields at each downstream location was expressed as the relative error between the corresponding values of the simulations, in percentages. The relative error expressed in the tables is effectively the relative difference in the area under each plot with respect to the plot for the 16D outlet length simulation. These values are shown for the three fields, between the 12D outlet and the 16D outlet simulation below in Table 4.6. The relative errors for the 14D and 15D outlet simulations with respect to the 16D outlet simulation are not presented here for the sake of brevity but are presented in the Appendix A.1.

Table 4.6: Downstream field profile relative difference with respect to the 16D outlet simulation (as %)

12D Outlet Simulation	**Downstream Location**			
Field	**8D**	**10D**	**11D**	**12D**
Streamwise Velocity	0.1296	0.1099	0.1057	0.1059
Temperature	0.0061	0.0086	0.0095	0.0102
Turbulence Kinetic Energy	0.3154	0.3458	0.3416	0.3435

The figure below (Figure 4.26) shows the percentage change in the flow characteristics at different downstream locations in the outlet between the 12D and 16D outlet simulations. Analysing the figure

and the tabulated values presented above, it can be concluded that an outlet length of 12D downstream from the junction is sufficient enough to observe important flow development due to the thermal mixing of the fluids at the junction, while not being influenced by the pressure outlet boundary at the end of the outlet pipe. To add a margin of safety, an additional length of 1D was considered bringing the total outlet length to 13D.

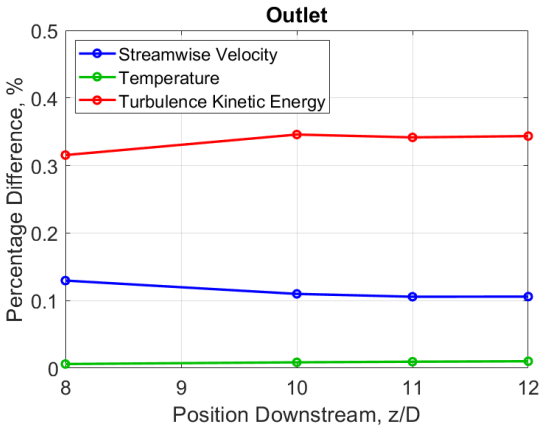

Figure 4.26: Comparative profile differences (percentage) at different downstream positions for the outlet pipe

Therefore, from the results of the pipe length optimization study, it can be concluded that the inlet and branch pipes need to be of length **3D** (not including the separate recycling inlet lengths), and the outlet pipe has to be of length **13D**. The computational domain of the UDNS calculation will be made using these geometrical parameters.

4.5. Mesh Sensitivity Study

A mesh sensitivity study is performed to ensure that the solution is devoid of any uncertainties arising from the domain discretization, while making sure that the cell sizes were not too small, which could lead to an unnecessary increase in computational effort. The mesh sensitivity study involved iterations with the previous studies conducted above, to ensure an optimum mesh scheme was used for all the simulations conducted. The simulation was carried out using a geometry with a junction corner radius of curvature r_c =1mm, with inlet and branch pipe lengths of 3D (not including the recycling inlets), and an outlet pipe length of 16D. The Reynolds number of the simulations is Re = 11700. 5 meshes were considered for this sensitivity study, named Mesh 1 (finest) to Mesh 5 (coarsest). All the meshes used a boundary layer (prism layer in Star-CCM+) mesh, which can be manipulated to set the wall cell size according to the expected wall y+ value (based on the Reynolds number of the simulation). A prism layer stretching factor is used to control the growth of the boundary layer mesh and ensure a smooth transition to the bulk cells. The bulk cells were polyhedral cells in the junction region, while further upstream and downstream along the inlet, branch and outlet pipe regions, a directed mesh (Star-CCM+ terminology) was implemented which mapped the polyhedral mesh cells at the junction and extruded them through the length of the pipes.

The mesh parameters were modified from the values of the baseline mesh, Mesh 3. Mesh 1 has finer bulk cells (by a magnitude of 1.5) and corresponding boundary layer mesh. Mesh 2 uses only a finer bulk mesh (by a magnitude of 1.5). Mesh 4 and Mesh 5 are coarser meshes in the bulk region alone by magnitudes of 1.5 and 2.5 respectively. The salient parameters of the meshes implemented in the different simulations are tabulated below in Table 4.7.

Table 4.7: Mesh parameters for the meshes used in the Mesh Sensitivity Study

	1	2	3	4	5
Bulk Size	0.0005	0.00067	0.001	0.0015	0.0025
Boundary Layer Mesh					
First cell size, a_0 [m]	0.00003	0.00006	0.00006	0.00006	0.00006
Last cell size, a_n [m]	0.0005	0.000666667	0.001	0.0015	0.0025
Number of Prism Layers, n	24	16	12	9	5
Prism Layer Stretching, r	1.125	1.169	1.289	1.524	2.394
Prism Layer Thicnkess, S_n [m]	0.00425	0.00425	0.00425	0.00425	0.00425
Total Number of Cells	10212467	4421894	1778552	652805	252028

The following figures show the different meshes at the junction region.

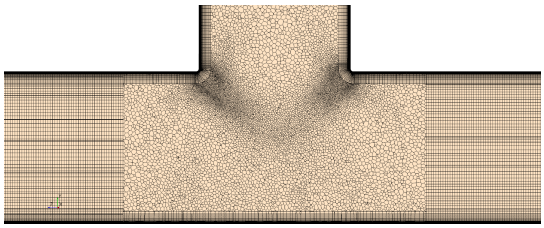

(a) Mesh 1

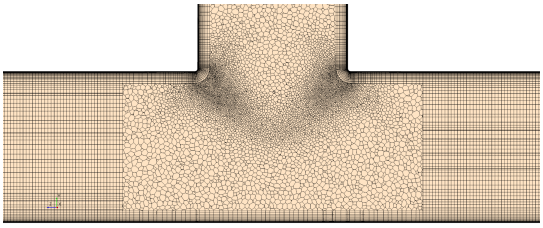

(b) Mesh 2

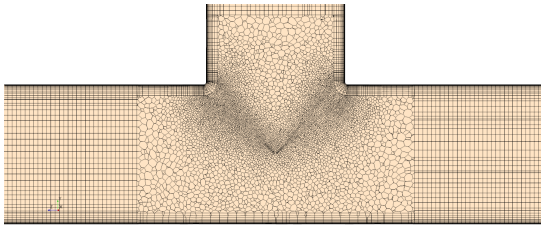

(c) Mesh 3

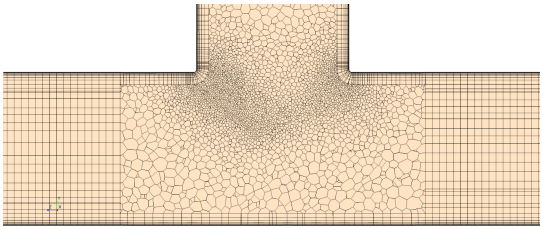

(d) Mesh 4

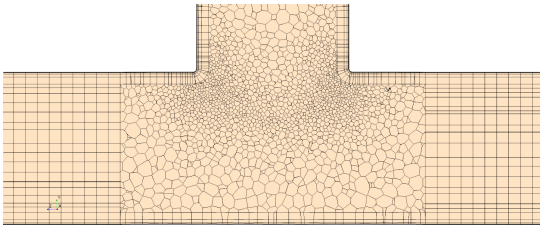

(e) Mesh 5

Figure 4.27: Mesh images for the Mesh Sensitivity Study

All 5 meshes were run as RANS simulations with the $k-\omega$ SST-Menter turbulence model. Additionally, Mesh 2 and Mesh 3 were also run as URANS simulations. The simulations were run until steady-state or the fluctuations in the monitors (if any) became periodic. Similar to the Reynolds scaling test done before, a quantitative comparison of the streamwise velocity, temperature, and additionally, the turbulence kinetic energy fields were taken at multiple locations downstream of the junction, and the results were plotted for the 7 cases together. The field values were normalized again for the comparison. The normalization for the turbulence kinetic energy is as stated below:

$$TKE_{normalized} = \frac{TKE}{u_{bulk}^2} \tag{4.3}$$

with u_{bulk} being the value of the bulk velocity in the outlet pipe. The profiles were once again taken at 0.5D, 1D, 2D, 4D, 8D and 11D distances downstream of the T-junction center. The resulting normalized comparative profiles for the streamwise velocity, temperature and turbulence kinetic energy fields are shown below in Figure 4.28 for the 0.5D downstream location. The profile comparison figures for the other downstream locations are not presented here, but can be found in Appendix A.2.

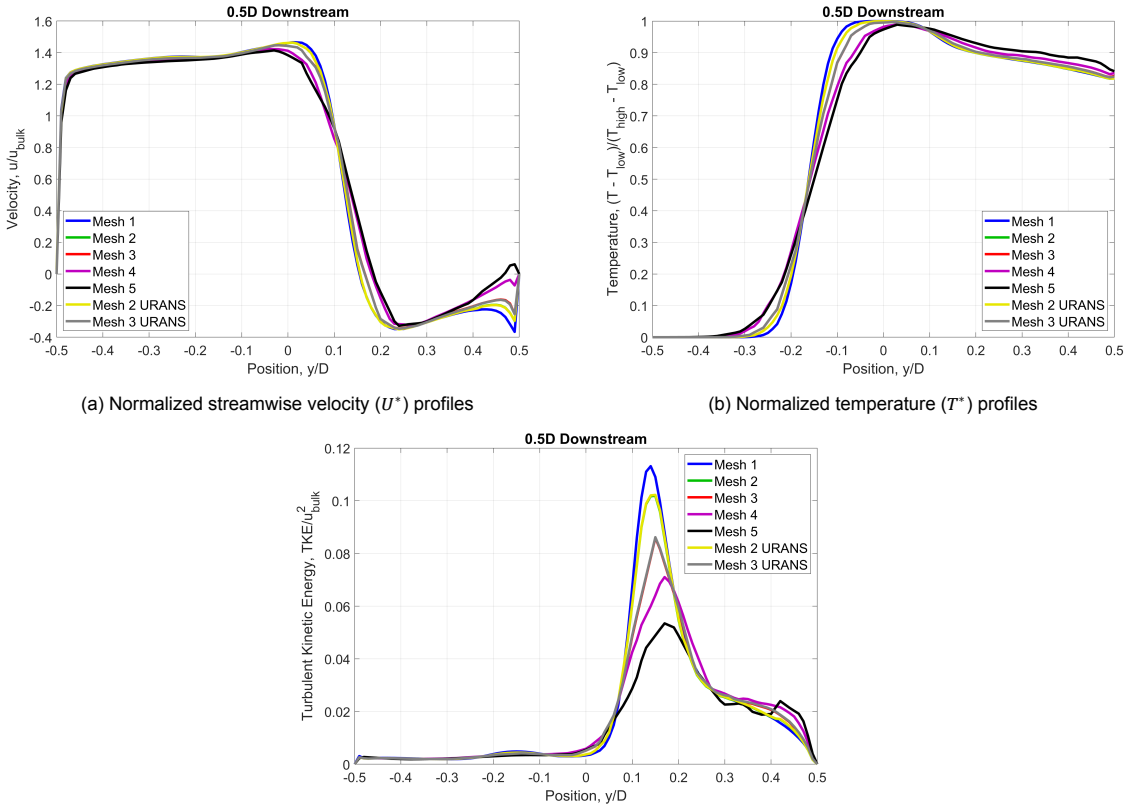

(a) Normalized streamwise velocity (U^*) profiles

(b) Normalized temperature (T^*) profiles

(c) Normalized turbulence kinetic energy profiles

Figure 4.28: Profile comparison plots at 0.5D downstream

To compare the performances of the meshes with respect to each other, and make a selection on which mesh is most suitable for the RANS simulations, it is not necessary to analyse these profile comparison plots in detail. Instead, the relative difference (errors) between the profiles of each mesh at each location were compared to the finest mesh, in this case, Mesh 1, and expressed as a percentage value. The relative difference between two profiles is essentially the difference in area under the graph of the two profiles. Therefore, these relative differences or errors, between each mesh case run with respect to the finest mesh were computed for the three fields and tabulated below in Tables 4.8-4.10.

Table 4.8: Relative difference (error in percentage) of streamwise velocity profiles with respect to Mesh 1

	ϵ_{1-2}	ϵ_{1-3}	ϵ_{1-4}	ϵ_{1-5}	$\epsilon_{1-2URANS}$	$\epsilon_{1-3URANS}$
0.5D	1.21	3.50	8.59	10.37	1.19	3.41
1D	0.78	2.89	6.80	9.89	0.76	2.73
2D	0.43	2.48	3.76	4.85	0.43	1.78
4D	0.31	2.65	3.10	3.78	0.29	1.85
8D	0.20	2.66	3.16	3.14	0.20	2.27
11D	0.22	2.20	2.79	2.90	0.22	2.17

Table 4.9: Relative difference (error in percentage) of temperature profiles with respect to Mesh 1

	ϵ_{1-2}	ϵ_{1-3}	ϵ_{1-4}	ϵ_{1-5}	$\epsilon_{1-2URANS}$	$\epsilon_{1-3URANS}$
0.5D	0.028	0.072	0.156	0.214	0.029	0.072
1D	0.026	0.065	0.143	0.182	0.026	0.066
2D	0.018	0.062	0.112	0.139	0.017	0.055
4D	0.014	0.039	0.062	0.111	0.013	0.034
8D	0.022	0.131	0.145	0.122	0.022	0.097
11D	0.026	0.162	0.175	0.174	0.026	0.154

Table 4.10: Relative difference (error in percentage) of turbulence kinetic energy profiles with respect to Mesh 1

	ϵ_{1-2}	ϵ_{1-3}	ϵ_{1-4}	ϵ_{1-5}	$\epsilon_{1-2URANS}$	$\epsilon_{1-3URANS}$
0.5D	5.52	16.38	26.11	33.56	5.33	16.54
1D	5.95	17.19	33.70	42.90	5.65	16.24
2D	3.33	18.14	26.04	30.83	3.08	14.78
4D	1.56	11.94	19.79	27.09	1.45	9.92
8D	1.53	10.09	12.40	14.73	1.52	7.82
11D	2.09	12.36	15.37	18.32	2.09	11.43

Judging by the values displayed in Tables 4.8 and 4.9, all meshes were close to or within 10% of the values of Mesh 1 for both streamwise velocity and temperature fields at all locations. However, when looking at the values for the turbulence kinetic energy, only mesh 2 shows differences that are less than 10% for all locations. In fact, Mesh 2 shows less than 6% deviation for turbulence kinetic energy at every location considered, which is highly satisfactory. Moreover, these differences stay consistent when considering the URANS simulation values of Mesh 2 as well. The scheme of Mesh 2 will therefore be implemented hereafter in all other tests.

4.6. Kolmogorov Scales and DNS Calibration Requisites

Having completed the calibration of the corner shape, established that the Reynolds number of the simulations can be scaled down, and optimized the length of the inlet and outlet pipes, it is required to extract the parameters that can help build the mesh for a DNS case. These parameters include the Kolmogorov length and time-scales, as well as the wall Y+ values estimated by the the RANS simulations. The relation for the Kolmogorov scales are given below. The Kolmogorov length-scale η_k is given by:

$$\eta_k = \left(\frac{\nu^3}{\epsilon}\right)^{\frac{1}{4}} \tag{4.4}$$

where ν is the kinematic viscosity, and ϵ is the rate of dissipation of the turbulence kinetic energy. Similarly, the Kolmogorov time-scale is then given by:

$$\tau_k = \frac{\eta_k^2}{\nu} = \left(\frac{\nu}{\epsilon}\right)^{\frac{1}{2}} \tag{4.5}$$

These values are extracted from the simulations run at Reynolds numbers 5300, 9100, and 11700. Since these simulations employed the $k-\omega$ SST Menter turbulence mode, an additional field function was needed to convert the predicted value of specific turbulence dissipation, ω to the dissipation rate ϵ, the relation between which is given as:

$$\omega = \frac{\epsilon}{k} \tag{4.6}$$

where k is the turbulence kinetic energy. The lowest values of the Kolmogorov length-scales are found in the regions near the upper wall immediately downstream of the junction where the highest turbulence dissipation occurs, which are then extracted and presented below in Table 4.11. The DNS target bulk cell size is approximated as 5 times the Kolmogorov length-scale values [1] extracted from the simulations.

Table 4.11: RANS Predicted Kolmogorov Length and Time Scales

Reynolds Number	**Predicted Kolmogorov Length-Scale (η_k) [m]**	**Target DNS Bulk Cell Size ($5 \times \eta_k$) [m]**	**Predicted Kolmogorov Time-Scale (τ_k) [s]**
5300	4.0×10^{-5}	2.0×10^{-4}	2.39×10^{-3}
9100	2.4×10^{-5}	1.2×10^{-4}	8.59×10^{-4}
11700	2.0×10^{-5}	1.0×10^{-4}	5.96×10^{-4}

To estimate the wall cell sizes that would be needed for the DNS mesh, the wall Y+ contours of the simulations were analysed, and the DNS wall cell size is calibrated using the maximum Y+ value found at the junction corner. The following figures show the wall Y+ contours for the Reynolds number = 5300 and 9100 simulations.

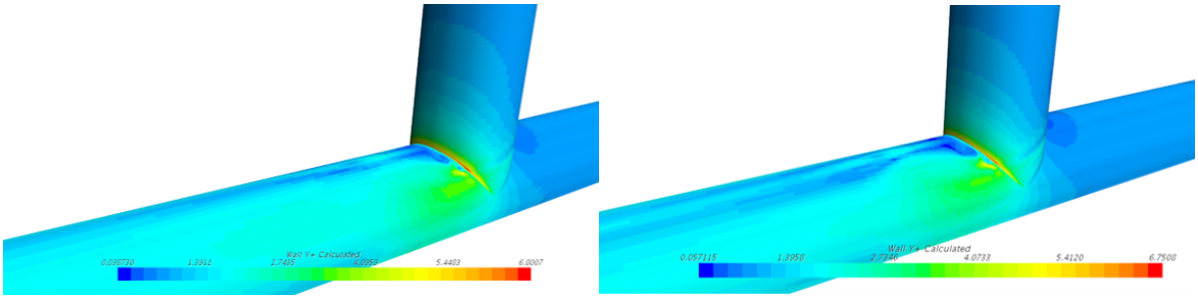

(a) Reynolds number = 5300

(b) Reynolds number = 9100

Figure 4.29: Wall Y+ contour plots to estimate DNS wall cell sizes

Table 4.12 below shows the extracted wall y+ values, along with the RANS first cell size used (known from the mesh parameters of the boundary layer mesh). Dividing these values gives the estimated wall cell size that would be needed to attain a wall y+ value. However, the target DNS wall cell size is calculated for a maximum wall y+ value of 0.8.

Table 4.12: DNS Mesh Wall Statistics

Reynolds Number	**RANS First Cell Size [m]**	**RANS Max. Wall Y+ at junction corner**	**Target DNS Wall Cell Size based on corner [m]**
5300	1.19×10^{-4}	6.8007	1.40×10^{-5}
9100	7.45×10^{-5}	6.7508	8.83×10^{-6}
11700	6×10^{-5}	6.5457	7.34×10^{-6}

The values that were calculated for the UDNS mesh and presented in the tables above were based on simulations run using a T-junction with pipes of diameter $0.054m$. For the UDNS case however, these values need to be normalized with the diameter of the pipes. The normalization for the Kolmogorov

length-scale and time-scale is given by:

$$\eta_k^* = \frac{\eta_k}{D_h} \tag{4.7}$$

$$\tau_k^* = \frac{\tau_k U_b}{D_h} \tag{4.8}$$

where $D_h = 0.054m$, is the diameter of the pipe, and U_b is the bulk velocity in the outlet pipe. The normalized values are tabulated below in Table 4.13.

Table 4.13: Calibrated values to be used in the UDNS calculation

Reynolds Number Re_b	**Friction Reynolds Number** Re_τ	**Normalized Kolmogorov length-scale** η_k^*	**Normalized DNS bulk cell size** $5 \times \eta_k^*$	**Normalized DNS wall cell size based on corner** Δ_1^*	**Normalized Kolmogorov time-scale** τ_k^*
5300	180	7.41×10^{-4}	3.7×10^{-3}	2.59×10^{-4}	5.83×10^{-3}
9100	290	4.4×10^{-4}	2.22×10^{-3}	1.63×10^{-4}	3.60×10^{-3}
11700	360	3.7×10^{-4}	1.85×10^{-3}	1.36×10^{-4}	3.21×10^{-3}

The normalized values of the DNS bulk cell size, along with the DNS wall cell size based on the corner wall Y+ are the two required parameters to set up the mesh for the UDNS test case. The setup of this UDNS case is explained in detail in the next chapter.

4.7. Additional RANS Simulations

The UDNS test case and the lined-up fully-resolved DNS is planned using Nek5000 [31], a fast and scalable high-order spectral-element code for CFD. Within the architecture of the code, it is possible to run a single calculation of the flow field with a given Reynolds number and implement multiple passive scalar fields with it. The passive scalars could involve different boundary conditions for the walls of the geometry, and also different Prandtl numbers. Additional RANS simulations were run to illustrate the simulations which are to be performed using DNS. The RANS simulations run for the Reynolds scaling tests involved the use of iso-flux (adiabatic) thermal wall boundary conditions. These simulations were run at a Prandtl number, Pr = 1. The results for the Re = 11700 simulation of this type is therefore already available. To add to these results, another simulation was created with the same geometry and meshing scheme (Mesh 2), with the boundary conditions now set as iso-temperature (constant temperature) on the walls. The temperature of the inlet and outlet walls were set at 300K, while the branch pipe wall was set to a temperature of 315K. This simulation was run at a Prandtl number Pr = 1 as well. Additionally, both the iso-flux and iso-temperature boundary condition cases were also run at a lower Prandtl number, Pr = 0.025, to analyse the sensitivity of the different fields to thermal diffusion. The Prandtl number is effectively the ratio of momentum diffusivity to thermal diffusivity, a Prandtl number greater than 1 implies lesser sensitivity between the thermal field to thermal diffusion, in comparison to the sensitivity between the velocity and molecular viscosity [17], and vice versa.

All four simulations reached a steady-state solution. The velocity field for all the four simulations mentioned above remain exactly the same, since the Prandtl number and the thermal boundary conditions would only manifest differences in the temperature fields. The streamwise velocity component contour for the simulations is shown below in Figure 4.30.

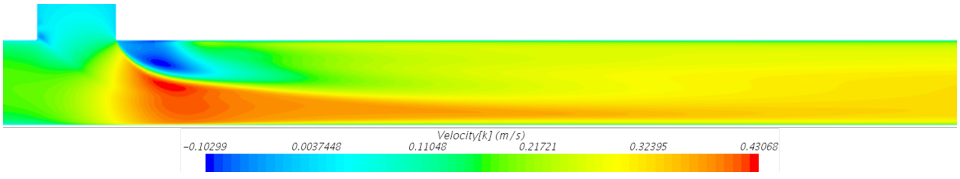

Figure 4.30: Streamwise velocity (u_z) contour for Reynolds number = 11700

The contour plots of the temperature field of the four simulations are presented below in Figure 4.31.

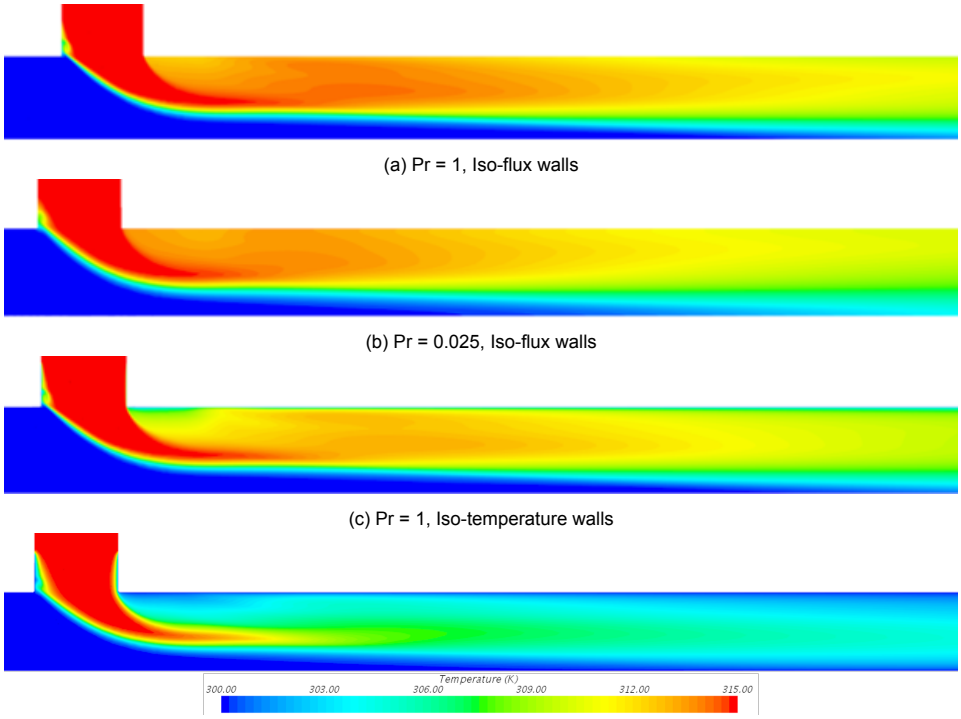

(a) Pr = 1, Iso-flux walls

(b) Pr = 0.025, Iso-flux walls

(c) Pr = 1, Iso-temperature walls

(d) Pr = 0.025, Iso-temperature walls

Figure 4.31: Temperature contours of the four simulations run

The temperature values at the walls are only slightly different when comparing the iso-flux boundary condition cases for the two different Prandtl numbers (Figures 4.31a and 4.31b). The diffusion of the temperature field seems discernibly higher in the lower Prandtl number case, as is expected. For the iso-temperature cases, temperatures in the near wall region are driven down due to the forcing of the boundary condition. The effect of the change in the Prandtl number can be seen more more clearly comparing Figures 4.31c and 4.31d, where due to the higher impact of thermal diffusion of the temperature, the lower Prandtl number case shows much lower temperatures in the outlet pipe region.

Quantitative profile comparison plots are also made for the normalized streamwise velocity and normalized temperature fields of the four simulations at 6 downstream locations, as done previously in the Reynolds scaling section. The velocity comparative plots are exactly the same for each downstream location, and are therefore not presented here, but can be found in the Appendix A.3. The temperature comparative plots are presented in Figure 4.32 below.

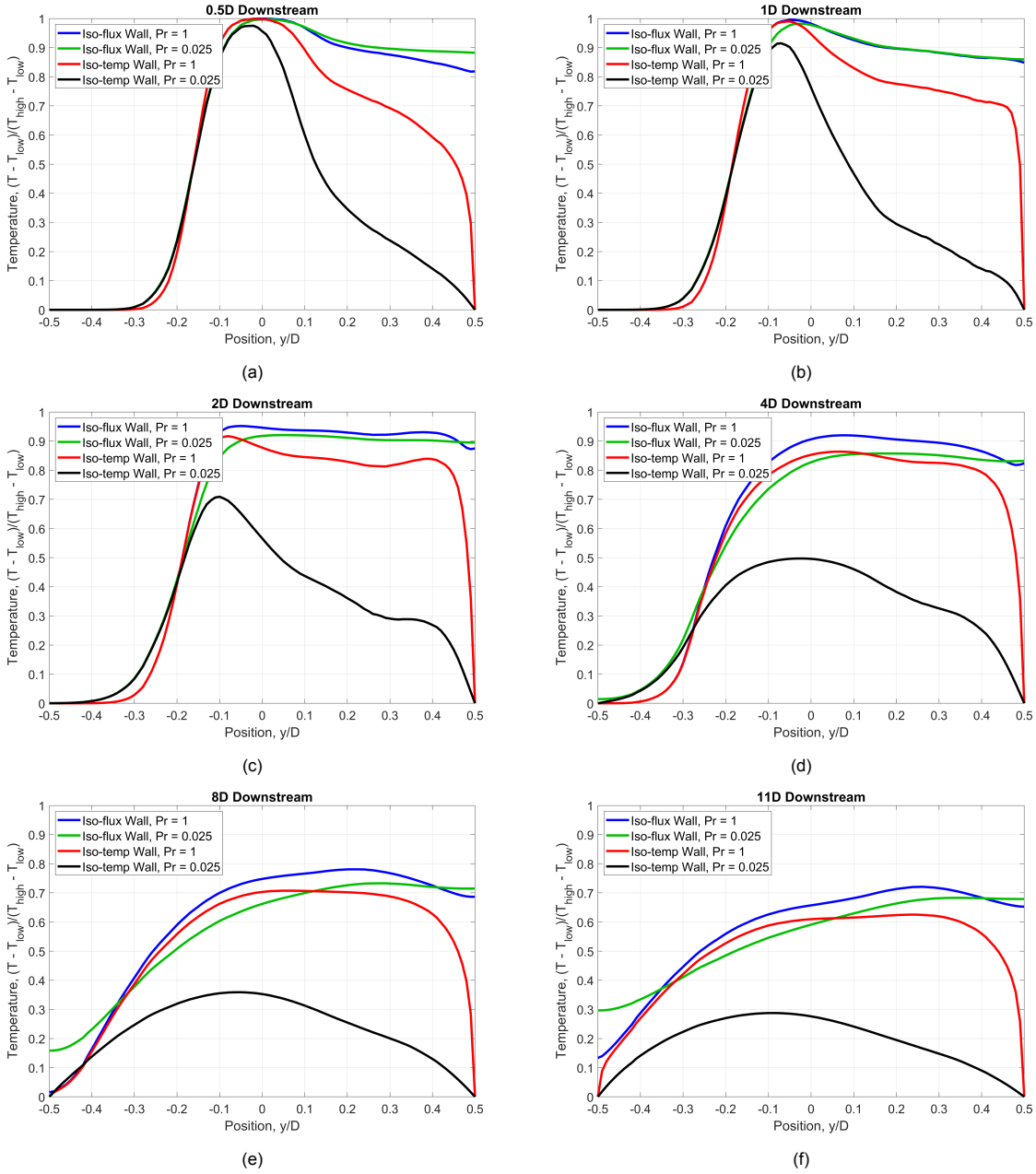

Figure 4.32: Normalized Temperature (T^*) comparative plots

The Pr = 1 iso-flux case shows a reduced value of temperature closer to the upper wall (+0.2 y/D to +0.5 y/D) at 0.5D downstream (Figure 4.32a). However, for all the other locations, the lower Prandtl simulations predict lower temperature values through the pipe as expected, since lower Prandtl number cases show greater sensitivity to thermal diffusivity. As the upper wall is approached (+0.5 y/D), the temperatures of the iso-temperature cases are driven down as mentioned before to the prescribed boundary condition value of 300K ($T^* = 0$). Curiously, the temperature at the upper wall for the Pr = 1 case is always lower than that of the Pr = 0.025 case for the iso-flux conditions. Similar plots were made with the results of the UDNS case, but these are not discussed and only shown in the Appendix A.3.

5

Proof-of-Concept Under-Resolved DNS

An under-resolved DNS (UDNS) calculation is performed to demonstrate the case set up. The simulation is performed using the spectral-element code Nek5000 [31]. A spectral element method combines the generality of the finite element method with the accuracy of spectral techniques for the numerical solution of the incompressible Navier-Stokes equations [35]. Nek5000 employs the Gauss-Lobatto-Legendre polynomial expansion along each spatial direction. The velocity and the pressure fields are represented by the same polynomial degree spatial discretization (i.e., $P_N - P_N$ formulation). In order to avoid spurious pressure modes of the pressure-velocity collocated scheme, Nek5000 employs a high-order splitting approach [36] that has shown high order accuracy in time and minimal mass conservation errors. The code offers a method of characteristics (OIFS) for time-advancement scheme whereby the calculations can run at CFL numbers higher than unity without loss in accuracy ([32], [37]). The present UDNS utilizes this scheme in third-order accuracy to keep CFL $\leq$ 2, which corresponds to a non-dimensional time-step of Δt^+ 0.006 (where $\Delta t^+ = \Delta t u_\tau^2/\nu$).

5.1. Case set up

As stated previously in Section 4.3, an inlet Reynolds number of Re = 5300 ($Re_\tau = 180$) is chosen for the present DNS case set up. The inlet and branch pipe lengths are 8D in length, which include a length of 5D recirculating region [34]. An outlet length of 13D is selected. The outflow is modelled with a turbulent outflow boundary condition, while the walls are modelled as no-slip. Six temperature scalars are included as passive scalars in the calculation. The six scalars model iso-temperature (Dirichlet boundary condition), iso-flux (Neumann boundary condition) and mixed wall conditions (Robin boundary condition), each for a Prandtl number of 1.0 and 0.025. The results of the calibration study completed previously above form the basis of the case setup of the UDNS case. The wall friction and Kolmogorov length scale estimates from RANS determine the mesh requirements for the bulk and near-wall regions. It should be noted that in the present meshing strategy (which is based on the estimates for the mixing region) maps the cross-section with the same number and size of cells in both the inlet and outlet regions. Further discussion on the spatial resolution in these regions is carried out later. Figure 5.1 represents the case set up described.

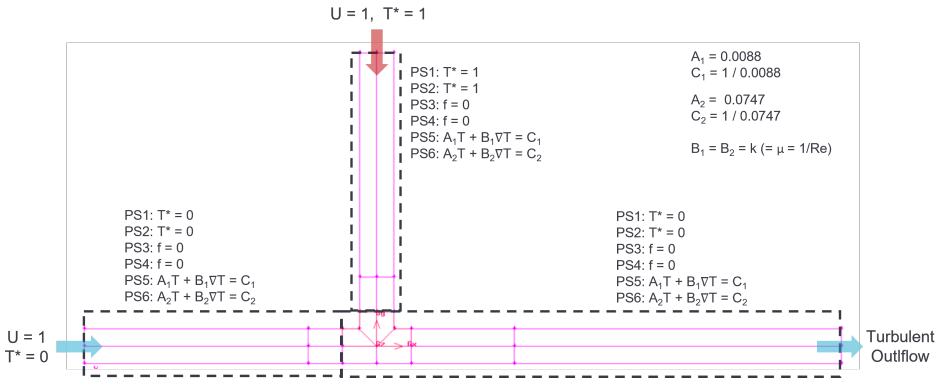

Figure 5.1: UDNS case geometry and boundary conditions

The domain is mapped with a macro-element grid size of 270480, which meets the fully-resolved DNS requirements at a spatial discretization of polynomial order of N = 9. However, the scope of the thesis limits the computation to be performed at a polynomial order of N = 3. This gives a total of 17.3×10^6 degrees-of-freedom. At this discretization, the maximum wall y+ in the inlet, outlet and junction regions are estimated to be 0.7, 1.5 and 5.7, respectively. The bulk resolution is estimated to be roughly 13.5 wall units. Table 5.1 shows the mesh estimates based on the RANS results. The discretization across the pipe cross-section is illustrated in Figure 5.2.

Table 5.1: DNS Mesh resolution estimates from RANS

	Macro-elements	**N =3**	**N = 5**	**N = 7**	**N = 9**
Total Size	270 480	7.30 M	33.81 M	92.77 M	197.2 M
Wall cell size	0.0056 D	0.0019 D	0.0011 D	0.0008 D	0.0006 D
Max wall y+ Inlet Legs	-	0.68	0.40	0.29	0.23
Max wall y+ Outlet leg	-	1.5	0.89	0.29	0.23
Max wall y+ Junction corner	-	5.7	3.4	2.5	1.9
Bulk cell size	0.052 D	0.0173 D	0.0104 D	0.0074 D	0.0058 D
(in terms of η_k)	-	~23.4 η_k	~14.0 η_k	~10.0 η_k	~7.8 η_k
Δy_1^+	-	13.7	8.3	5.9	4.6

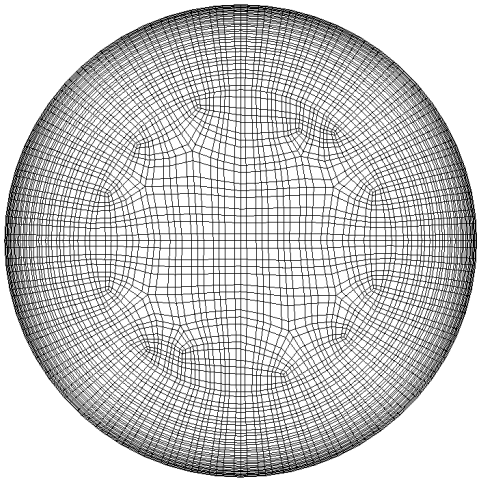

Figure 5.2: Pipe Discretization for the UDNS calculation

Inclusion of CHT with solid walls in DNS amounts to large computational costs due to the slow statistical convergence of the thermal fields in the solid region. Flageul et al [29] has shown that a Robin (mixed)

wall boundary condition is able to mimic CHT. As shown previously in Section 3.4, in order to select the parameter set in the present calculation, separate channel flow DNS calculations at $Re_\tau = 180$ were performed in-house with iso-flux and iso-temperature boundary conditions. It is estimated that ratio A^2/B^2 is equal to approximately 612.4 and 27.3 for Prandtl numbers 1 and 0.025, respectively. The value of coefficient B is kept equal to the thermal conductivity of the scalar, k $(= \mu C_p/Pr)$. This gives coefficient values for A, B and C as A = 0.0088, C = 1/0.0088, for the Pr = 1 scalar, and A = 0.0747, C = 1/0.0747, for the Pr = 0.025 scalar. The value of B is the same for both scalars and is equal to B = k (= μ = 1/Re).

5.2. UDNS Results

Figure 5.3a presents the wall friction velocity history plot for the inlet, branch and outlet legs and Figure 5.3b presents the integral wall heat flux history plot of the two iso-temperature scalars. The flow transient is observed to be characterized by initial period of flow development period, followed by a quasi-steady state. In the present UDNS, the statistical time-averaging calculation is started at $t^* = 100$, after the flow reached a fully-developed state (where $t^* = tU_b/D$, and U_b is the bulk velocity of the inlet).

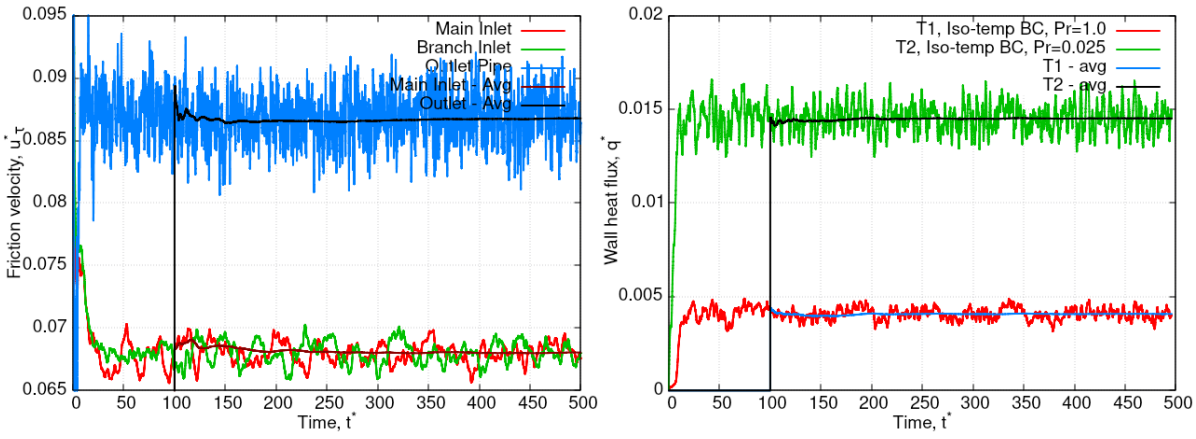

(a) Wall friction velocity history plot

(b) Wall heat flux history plot of the two iso-temperature scalars

Figure 5.3: History plots for the UDNS Calculation with time-averaging values plotted

The time-averaged statistical convergence is estimated by comparing the percentage change between mean and r.m.s. statistics sampled after an averaging period of $\Delta t^* = 350$ and 400. Figure 5.4 illustrates this percentage change for the different quantities at different locations in the domain. It is shown that percentage change for mean and r.m.s. quantities is below 0.5% and 1.0%, respectively, at all locations. This is considered to be sufficiently converged for the present scope. Thus, the results presented hereafter correspond to time-averaging period of $\Delta t^* = 400$ (or $\Delta t^+ \approx 2500$). It should be noted that higher-order statistics are not assessed, as the low spatial resolution is likely to result in these statistics not converging at all. PS1-6 are the six temperature 'passive scalars' – (in order) iso-temperature condition (Pr = 1.0 and Pr = 0.025), iso-flux condition (Pr = 1.0 and Pr = 0.025), and the mixed condition (Pr = 1.0 and Pr = 0.025).

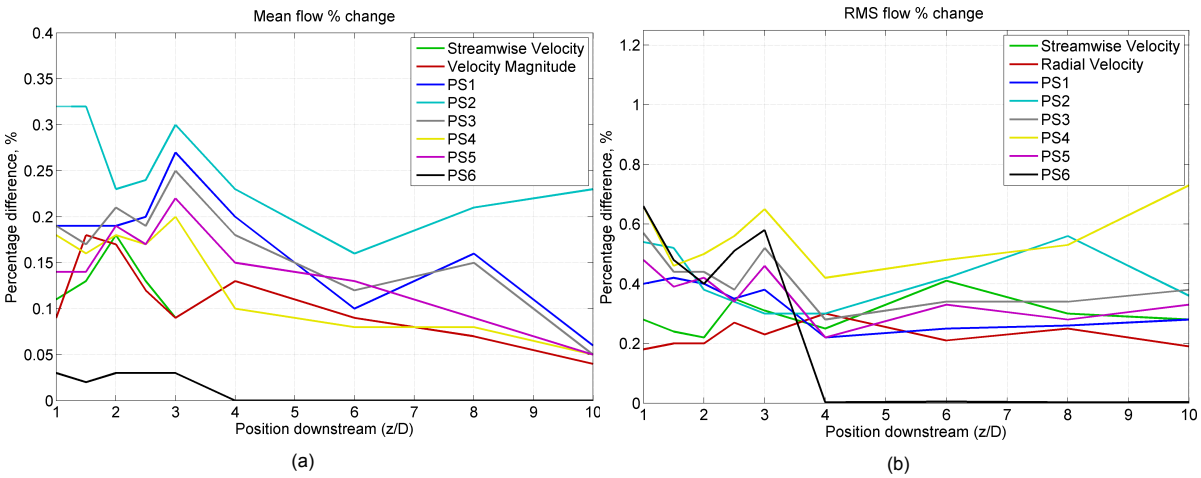

(a) (b)

Figure 5.4: Difference in time-averaged Mean and RMS quantities between statistics at $\Delta t^* = 350$ and $\Delta t^* = 400$

The statistical quantities for the present UDNS calculation are presented next. The contour plots of the time-averaged mean velocity magnitude and mean axial velocity are presented in Figure 5.5. The time-averaged r.m.s values of the (u_z) and (u_y) components of velocity are presented in Figure 5.6. The contour plots clearly show the well-defined recirculation region immediately downstream of the junction at the upper wall, characterized by the low values of mean streamwise velocity corresponding to the region of high magnitude of the r.m.s quantities. The higher mean values of the streamwise velocity below the recirculation region are representative of the mixing of the flows in the middle of the pipe. It is observed that there is pixelation in the r.m.s contours of the results of this UDNS case. This is attributed to the physics not being captured because of the inadequate resolution offered by the present spatial discretization of the lower polynomial order.

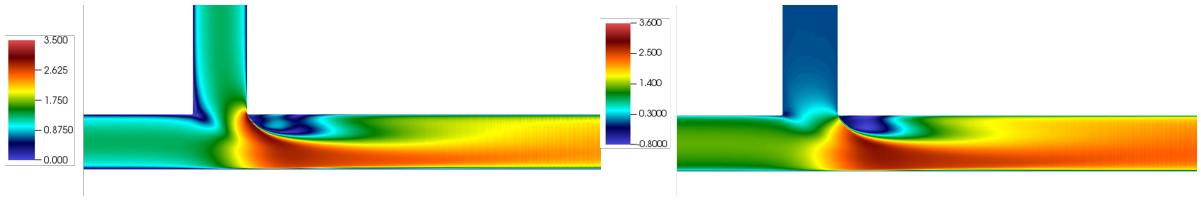

(a) Velocity magnitude (b) u_z

Figure 5.5: Mean velocity contours

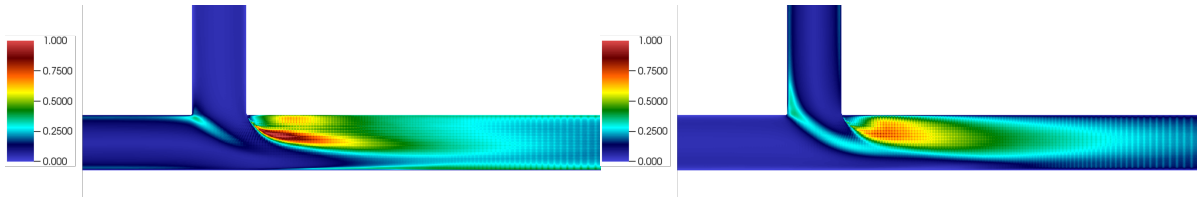

(a) u_z (b) u_y

Figure 5.6: RMS contours of velocity components

The instantaneous velocity magnitude plot is presented below in Figure 5.7.

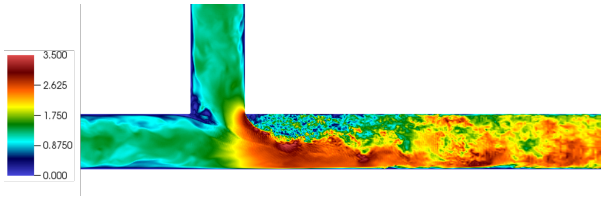

Figure 5.7: Instantaneous velocity magnitude contour

For the sake of brevity, the detailed statistics of only two temperature scalars are presented below. The rest of the scalar contours will be presented in the Appendix A.4. The instantaneous, mean and r.m.s. fluctuating component of the temperature scalars with the iso-temperature boundary conditions (PS1 and PS2) are presented in Figures 5.8 - 5.10, respectively. Following the velocity contours, a clear mixing region can be seen in the middle of the channel downstream of the T-junction. There is a stark contrast between the contours of the two scalars, due to the different Prandtl numbers used. The Prandtl number being the ratio of the momentum diffusivity to the thermal diffusivity of the fluid concerned, implies that a lower value would show an increased diffusion of temperature through the same flow field. This can be observed in the contour plots as well – the high Prandtl number scalar shows a larger region with higher temperature values at the top half of pipe; whereas in the low Prandtl scalar, the temperature looks to have diffused very close to the start of the mixing at the junction. The r.m.s contours of the high Prandtl number scalar further validate that the spatial discretization used needs to be further resolved to capture the physics of the thermal field for this case, although the discretization seems to be fine for the lower Prandtl number case as is expected.

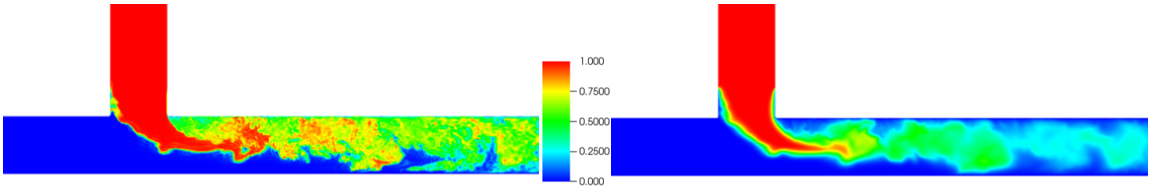

(a) High Prandtl number (b) Low Prandtl number

Figure 5.8: Instantaneous temperature contours for the iso-temperature scalars

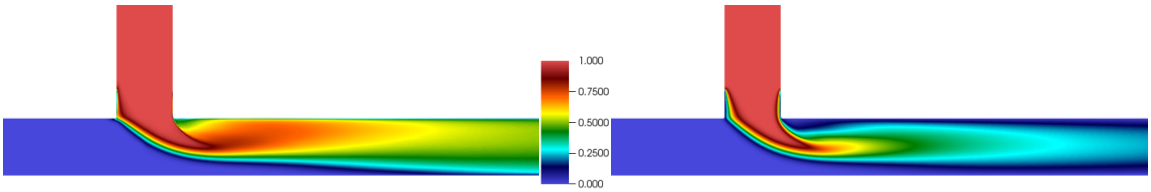

(a) High Prandtl number (b) Low Prandtl number

Figure 5.9: Time-averaged mean temperature contours for the iso-temperature scalars

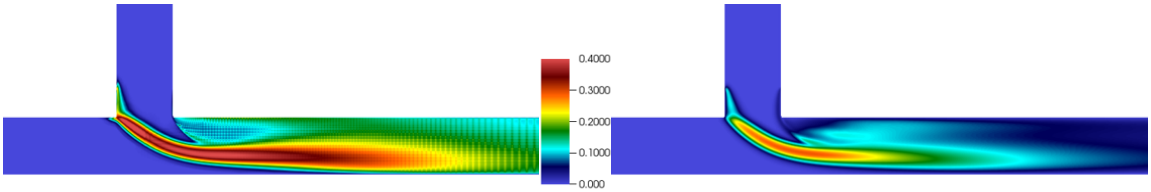

(a) High Prandtl number (b) Low Prandtl number

Figure 5.10: Time-averaged RMS temperature contours for the iso-temperature scalars

As stated previously, the coefficients of the Robin (mixed) boundary condition are estimated from separate channel flow DNS simulations at $Re_\tau = 180$ in order to mimic the condition of CHT. The fluctuating component of the temperature scalars are affected directly with boundary condition coefficients. Thus, it is expected that only the r.m.s. fluctuating component of these scalars mimic the CHT condition. On the other hand, the absolute value of the scalar has little significance. Figure 5.11 presents the contour plots of the r.m.s. fluctuating component of these scalars. Further analyses is required to determine if the employed Robin boundary faithfully represents the CHT condition.

Confirming the use of Robin boundary to replace CHT appears to be a difficult task. Sample DNS calculations may be performed for CHT in channel flow geometry as reference, in order to compare the results for equivalent Robin boundary condition therein. Alternatively, if the turbulent temperature flux model is employed in RANS in combination with CHT with solid walls for the present geometry, the RANS-predicted temperature variance field may be used to compare the magnitude of r.m.s. temperature calculated in the present UDNS. The capabilities and limitations of the Robin boundary condition need to be assessed before implementing the same in the final DNS calculation.

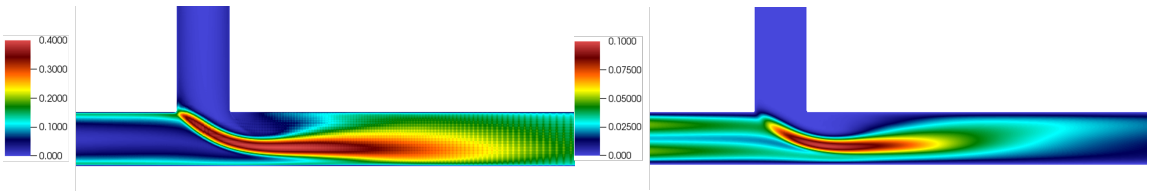

(a) High Prandtl number (b) Low Prandtl number

Figure 5.11: Time-averaged RMS temperature contours for the Robin boundary condition scalars

5.2.1. Calibration for the fully-resolved DNS

The estimates for the mesh requirements for the final DNS are re-assessed using the present UDNS results. The recommended cell size for fully resolving physics of turbulent flow is $\Delta \approx \pi\eta_k$ [1]. The estimated Kolmogorov length-scales for the present results are calculated from the dissipation of turbulent kinetic energy as $\eta_k = \left(\frac{\nu^3}{\epsilon}\right)^{\frac{1}{4}}$, where ν and ϵ are the kinematic viscosity and turbulent kinetic energy dissipation, respectively. Figure 5.12 presents the local spatial discretization normalized by η_k. It is seen that the maximum value of this quantity reaches approximately 13 in the mixing zone. Interpolating from the present discretization, polynomial order of N = 9 should reduce this value to roughly 4, which can be considered to be a fully-resolving discretization. Figure 5.13 shows the contour of the Kolmogorov length scales in the calculation. Comparing the value tabulated in Table 4.13 (7.41×10^{-4}) to the contour values, specifically in the region immediately downstream of the T-junction near the upper wall where the Kolmogorov length scales are the smallest, a good agreement can be observed between them. The UDNS results prove that the RANS estimates on Kolmogorov length scales were reasonably accurate.

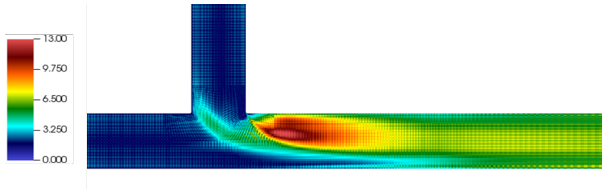

Figure 5.12: Contour plot of the local spatial discretization normalized by Kolmogorov length scales

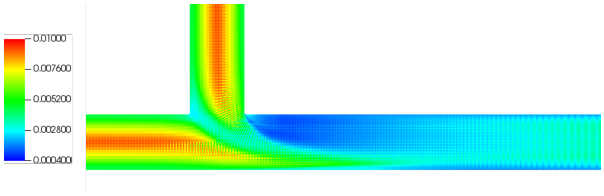

Figure 5.13: Contour plot of the Kolmogorov length scales

The results of Figure 5.12 however imply that the value of the local spatial discretization normalized by η_k when interpolated to a polynomial order of N = 9 reduces to < 1 in the upstream inlet regions and to ≈ 2 in the downstream outlet region. This is an unnecessary 'over-resolution' of those regions compared to the local flow physics. A different meshing strategy may be investigated whereby different number of cells and cell sizes can be mapped across the cross-section along the length of a pipe. With this strategy, the macro-element distribution may be adapted to the local flow requirements, in order to save computational requirement of the final DNS.

The wall friction velocity time history plot in Figure 5.3a indicates that the friction velocities attain time-averaged values that can be used to calculate the wall y+ values on the walls of the main inlet and outlet pipes. The time-averaged values of the friction velocity u_τ^* are $\approx$ 0.068 and 0.087 for the main inlet and outlet pipe respectively. This gives average wall y+ values of 0.685 for the main inlet and 0.876 for the outlet pipes (where y+ = $u_\tau \rho y/\mu$, value of y taken from Table 5.1). These average values are also inline with what was predicted by RANS, therefore showing that RANS offers a reasonable estimation.

Further, the distribution of CFL numbers based on local instantaneous velocities is presented in Figure 5.14. The mesh discretization at the polynomial order of N = 3 can also be seen. As stated previously, time-stepping in the present calculation is regulated by a maximum CFL of 2. It is seen that this maximum value appears in only a few cells at the junction corner. The maximum allowed time-step appears to be limited due to only these few cells. Thus, a further optimization of the mesh is also recommended for the final DNS in order to ease this bottle-neck condition at the junction corner.

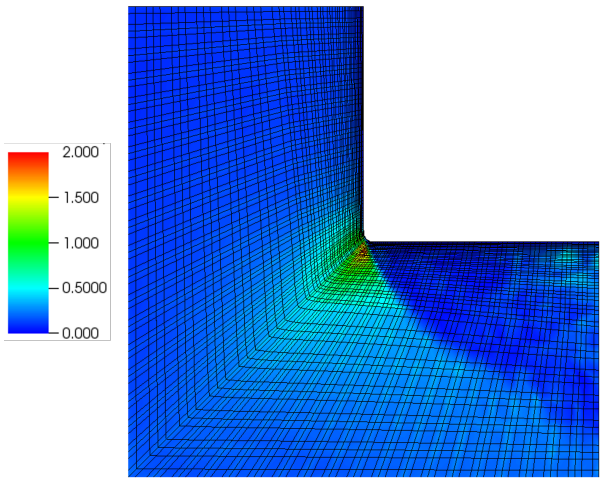

Figure 5.14: Distribution of CFL numbers at the junction corner

Based on the results presented above, it can be concluded that the RANS results provided a reasonable estimation for the wall cell sizes and the Kolmogorov length scales with which the UDNS mesh can be created. It was also seen that these parameters when interpolated to a fully-resolved DNS case (N =9), would provide a satisfactory domain discretization to observe the fully resolving physics of turbulent flow. The UDNS calculation also suggests that the time-averaging calculations that need to be implemented for the fully-resolved DNS should be initiated at close to t^+ = 600 ($\approx t^*$ = 100), when the flow is expected to have reached a fully-developed state. However, it is also recommended that

the wall friction velocity and wall heat flux values be monitored to ensure that the flow has indeed completed its flow development period and attained a quasi-steady state. It may be that for the fully-resolved calculation, the friction velocity and heat flux values may show a different trend to what is seen above. For the period of time-averaging required, it is seen that statistical convergence can be expected around $\Delta t^+ = 2100$ ($\approx \Delta t^* = 350$) after the commencement of the time-averaging statistical calculations. This is because there is very little change in the mean and r.m.s quantities between this point and at an averaging time of $\Delta t^+ = 2500$ ($\approx \Delta t^* = 400$). These assessments are not based on higher-order statistics however, since the spatial resolution of the UDNS conducted will probably not lead to a convergence of these statistics anyway. Therefore, for the fully-resolved DNS, the convergence must be estimated based on not only the relative change in the mean and r.m.s quantities between two different averaging periods, but also the change in higher-order statistics like the skewness and flatness of velocities.

6

Conclusions

The thesis aimed to design a DNS calculation of the flow and heat transfer involved in the thermal mixing of a T-junction using RANS CFD simulations. The work done highlights a path to calibrating expensive DNS calculations using relatively cheap RANS simulations, saving a significant amount of time and effort in the process. Additionally, a benchmark DNS database can also be simulated based on the results of this thesis that can act to aid the validation of momentum and heat flux turbulence models and even other T-junction simulations.

To begin this calibration using RANS simulations, the turbulence model to be employed for the simulations was investigated. The literature survey showed that the $k-\epsilon$ and the $k-\omega$ models were the most frequently used turbulence models for the T-junction simulations. However, this needed to be validated before use in the thesis, and hence the performance of the Lien Linear low Reynolds standard $k-\epsilon$ model, the Lien Cubic low Reynolds standard $k-\epsilon$ model, the Realizable $k-\epsilon$ model and the $k-\omega$ SST-Menter model were compared for the T-junction thermal mixing in Section 4.1 of Chapter 4. The $k-\omega$ SST-Menter model was chosen to be the final turbulence model to be implemented in all the RANS simulations thereafter.

Research Question (1a) was answered in Chapter 4, Section 4.2. Here, the literature survey showed that either a sharp corner, or a corner of radius of curvature $r_c = 18mm$ are commonly used in reference experimental cases. Using this to establish a range for the corner shape calibration, 2D simulations, followed by 3D simulations, were used to narrow the range and compare the behaviour of the prominent flow features in the T-junction mixing, such as the recirculation zone and the mixing regions. It was concluded that a corner radius of r = 1mm, or $r_c/D = 0.02$ was the maximum value that could still reproduce the important phenomena in the sharp corner T-junction satisfactorily. This calibration was done in order to eliminate the numerical dissipation effects caused by the domain discretization of a sharp corner geometry in DNS cases, thereby reducing the mesh requirements at the corner and simplifying its implementation.

The motivation for Research Question (1b) was based on the observation from the literature survey that experimental reference cases in facilities like the WALTON facility were run at high Reynolds numbers like Re = 40000 and 60000. These Reynolds numbers are computationally extremely expensive for DNS calculations, especially for the complex T-junction mixing phenomena. The purpose of the Reynolds scaling tests was therefore to analyse whether the turbulence and mixing phenomena observed at the higher Reynolds numbers corresponding to experimental facilities is reproducible at lower Reynolds number values commonly used in DNS cases of pipe flows, and therefore answer Research Question (1b). From Section 4.3 of Chapter 4 it was concluded that Re = 5300, 9100 ad 11700 corresponding to Re_τ = 180, 290, and 360, did indeed show good agreement with the higher Reynolds number cases, proving that the scaling was indeed feasible. A Reynolds number of 5300 (Re_τ = 180) was selected to be used in the DNS calculation based on computational cost concerns.

Research Question (1c) required that the geometry to be used for the DNS calculation had inlet and outlet lengths that were sufficiently large to prevent any interference on the mixing going on at the junction. This entails that the flow development from the inlets does not affect the thermal mixing downstream in the junction, while for the outlet pipe, the effect of the pressure outlet boundary on the junction had to be minimised, while making sure that the entire downstream influence of the mixing was captured. This was done in Section 4.4 of Chapter 4, where pipe length optimization studies were run for the inlet, branch and outlet pipes. The final lengths of the inlet and branch pipes were 3D, excluding the recycling inlet lengths needed. The outlet pipe was determined to be 13D in length from the junction. All lengths included a margin of safety. To answer Research Question (1d), a mesh sensitivity study was conducted in Chapter 4, Section 4.5 with a few iterations along with the studies mentioned above, to ensure that the discretization of the domain did not yield any uncertainties.

Chapter 4 Section 4.6 involved part of the answer to the Research Question (1e). Here, to aid the set up of the DNS mesh, the cell size at the wall, the maximum wall y+ values and the Kolmogorov length scales were extracted from the Re = 5300, 9100 and 11700 RANS simulations. A few additional RANS simulations were also run in Chapter 4 Section 4.7 to illustrate the passive scalar calculations which are to be performed using the DNS since the DNS can incorporate the calculation of multiple passive scalars within the same simulation. This section involved RANS simulations which used iso-flux and iso-temperature wall thermal boundary conditions, and were run at two different Prandtl numbers, Pr = 1 and Pr = 0.025.

These sections together answer completely all but one of the sub-questions (Research Question (1e)) of Research Question (1). Chapter 5 Section 5.2 showed that the RANS results provided a reasonable estimation for the wall cell sizes and the Kolmogorov length scales with which the DNS mesh can be created, thereby completing the answer to Research Question (1e).

Research Question (2) was then looked at and answered by the work shown in Chapter 5 Section 5.2 as well. For Research Question (2a), the UDNS calculation suggested that the time-averaging calculations to capture transient features of the problem should be commenced at close to t^+ = 600 ($\approx t^*$ = 100), when the flow is expected to have reached a fully-developed state. Along with this, it is also prudent to monitor the wall friction velocity and wall heat flux values to double check that the flow has indeed fully-developed (quasi-steady state). Additionally, for the time-averaging period required, statistical convergence is observed around Δt^+ = 2100 ($\approx \Delta t^*$ = 350) from the start of the time-averaging statistical calculations.

The answer to Research Question (2b) was found in the values of the Kolmogorov length scales and wall friction velocity of the UDNS case. It was concluded that these parameters when interpolated to a fully-resolved DNS case (N =9), would provide a satisfactory domain discretization to observe the fully resolving physics of turbulent flow. Therefore, the UDNS case supports that the estimations made from RANS can be implemented in a fully-resolved DNS and can fully capture the turbulent flow physics involved.

The distribution of CFL numbers (based on local instantaneous velocities) presented in Figure 5.14 of Chapter 5 Section 5.2 show that the maximum time-stepping regulated value of CFL = 2 only appears in a few cells at the junction corner. These cells thus limit the maximum allowed time-step by causing bottle-neck condition at the junction corner. This answers Research Question (2c).

The higher order statistics of the scalars alone mimic the CHT condition, since only the temperature scalar fluctuating component are affected directly by the boundary condition coefficients. To answer Research Question (2d) however, the present results are not enough to analyse the efficiency of the Robin boundary condition in mimicking a conjugate heat transfer condition. Confirming the use of Robin boundary to replace a CHT condition is not straightforward. The capabilities and limitations of the Robin boundary condition need to be assessed before being implemented in the final DNS calculation.

The results of the present UDNS can aid the setup of the fully-resolved DNS by providing insight into the required meshing parameters, time-averaging strategy, and also a partial image of the effectiveness

of a Robin boundary condition to mimic CHT. The results obtained from the fully-resolved DNS can then be used to validate RANS models and better understand the underlying physical phenomena of thermal mixing in the fluid and thermal fatigue in the solid walls. The fully-resolved DNS case can also be used as a reference benchmark for many other T-junction research projects.

6.1. Recommendations

These are a few of the recommendations that can be made based on the performance of the UDNS calculation that was run. This is not an exhaustive list but it does highlight a few of the key areas of concern, or where improvements can be made while setting up the final fully-resolved DNS.

- It is recommended to analyze the results for the mixed boundary condition in detail, in order to assess the capability and limitation of this condition. The implementation of the Robin boundary to mimic CHT requires additional sample DNS calculations for CHT in turbulent channel flow geometries, in order to compare the results and derive any savings in computational effort. Alternatively, a RANS based turbulent temperature flux model employed in combination with CHT with solid walls can mean a comparison between the RANS-predicted temperature variance fields and the magnitude of r.m.s. temperature from the present UDNS can be made.
- The UDNS discretization can lead to unnecessary ‘over-resolution’ in certain regions when interpolated for a fully-resolved DNS. The meshing strategy can be further optimized in the upstream and downstream regions from the junction, where this additional resolution is not needed. For example, a meshing strategy where the number of cells and size of cells is mapped according to the region along the length of the pipe can offer flexibility in adapting the macro-element distribution to the local flow requirements. The results would provide a significant saving in the computational time requirement of the final DNS.
- An optimization of the junction corner mesh is also recommended to ease the CFL requirement for the cells in the corner, since these are the cells responsible for the bottle-neck condition that limits the maximum allowed time-step. The benefits of this extend to the time-stepping, and computational cost reduction.
- To decide on the commencement of the time-averaging calculation, it has to be made sure that the flow has attained a quasi-steady state and is fully developed. In addition to the time-averaging strategy derived from the UDNS calculation, it is also recommended to monitor the wall friction velocity and wall heat flux values. This is because, for a fully-resolved calculation, the friction velocity and heat flux values may show a different trend to what was seen in the UDNS case.
- For the period of time-averaging required, it was seen from the UDNS case that statistical convergence can be expected at $\Delta t^+ = 2100$. However, since the spatial resolution of the UDNS conducted probably do not lead to a convergence of the higher-order statistics, these statistics could be not be used to determine the required time-averaging period. It is therefore recommended that for the fully-resolved DNS, the convergence of the solution must be estimated based on the relative change in higher-order statistics like the skewness and flatness of velocities, in addition to the mean and r.m.s quantities.

A

Appendix

A.1. Pipe Length Optimization

The relative errors for the three fields of the 12D, 14D and 15D outlet simulations with respect to the 16D outlet simulation are presented here as additional information to Section 4.4.

Table A.1: Downstream Streamwise Velocity profile relative differences with respect to the 16D outlet simulation (as %)

Streamwise Velocity	Downstream Location			
Simulation	**8D**	**10D**	**11D**	**12D**
12D Outlet	0.1296	0.1099	0.1057	0.1059
14D Outlet	0.1312	0.1139	0.1065	0.1079
15D Outlet	0.0756	0.0811	0.0859	0.0822

Table A.2: Temperature profile relative differences

Temperature	Downstream Location			
Simulation	**8D**	**10D**	**11D**	**12D**
12D Outlet	0.0061	0.0086	0.0095	0.0102
14D Outlet	0.0062	0.0087	0.0092	0.0101
15D Outlet	0.0068	0.0072	0.0074	0.0078

Table A.3: Turbulence Kinetic Energy profile relative differences

TKE	Downstream Location			
Simulation	**8D**	**10D**	**11D**	**12D**
12D Outlet	0.3154	0.3458	0.3416	0.3435
14D Outlet	0.3124	0.3596	0.3531	0.3359
15D Outlet	0.2548	0.2543	0.2932	0.3186

A.2. Mesh Sensitivity Study

The profiles of the normalized streamwise velocity, temperature and turbulence kinetic energy were taken at 0.5D, 1D, 2D, 4D, 8D and 11D distances downstream of the T-junction center. These are shown below for the 1D, 2D, 4D, 8D and 11D downstream locations.

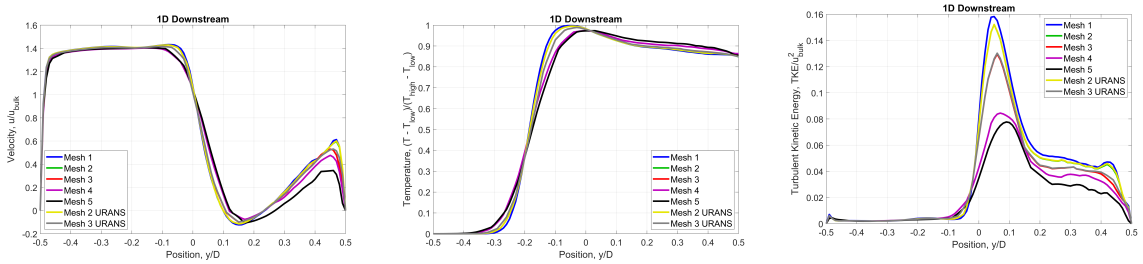

(a) Normalized streamwise velocity (U^*) profiles (b) Normalized temperature (T^*) profiles (c) Normalized turbulence kinetic energy profiles

Figure A.1: Profile comparison plots at 1D downstream

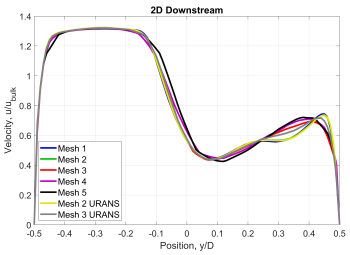

(a) Normalized streamwise velocity (U^*) profiles

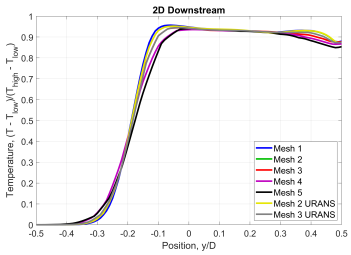

(b) Normalized temperature (T^*) profiles

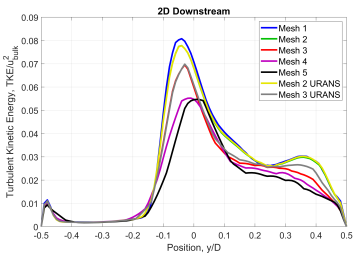

(c) Normalized turbulence kinetic energy profiles

Figure A.2: Profile comparison plots at 2D downstream

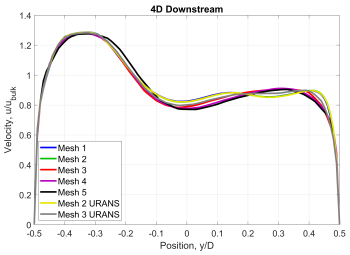

(a) Normalized streamwise velocity (U^*) profiles

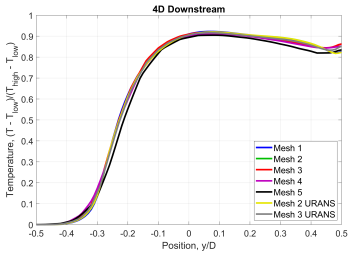

(b) Normalized temperature (T^*) profiles

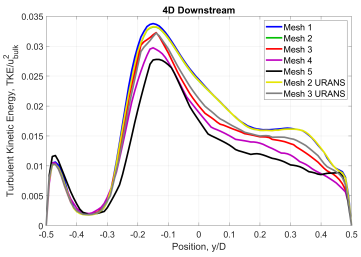

(c) Normalized turbulence kinetic energy profiles

Figure A.3: Profile comparison plots at 4D downstream

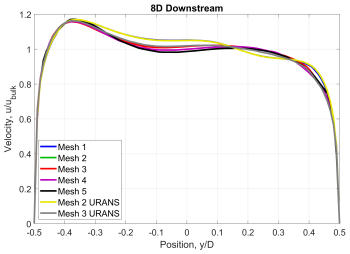

(a) Normalized streamwise velocity (U^*) profiles

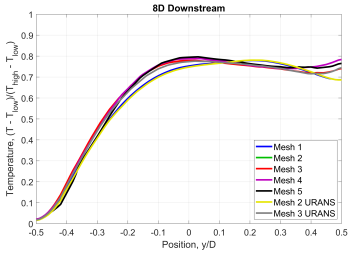

(b) Normalized temperature (T^*) profiles

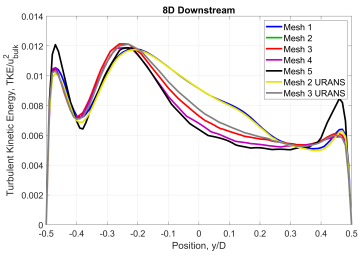

(c) Normalized turbulence kinetic energy profiles

Figure A.4: Profile comparison plots at 8D downstream

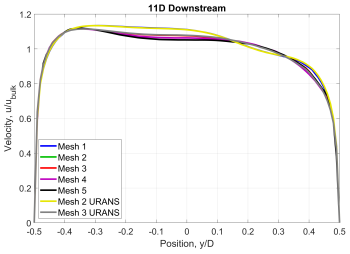

(a) Normalized streamwise velocity (U^*) profiles

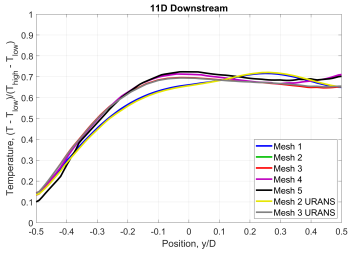

(b) Normalized temperature (T^*) profiles

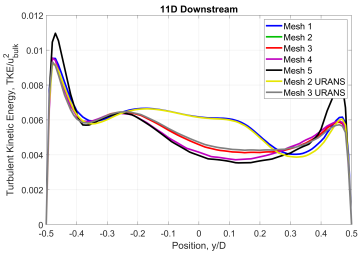

(c) Normalized turbulence kinetic energy profiles

Figure A.5: Profile comparison plots at 11D downstream

A.3. Additional RANS Simulations

Additional simulations were run using RANS at Prandtl numbers Pr = 0.025 and 1, using both the iso-flux and iso-temperature boundary conditions. The velocity comparative plots are presented below.

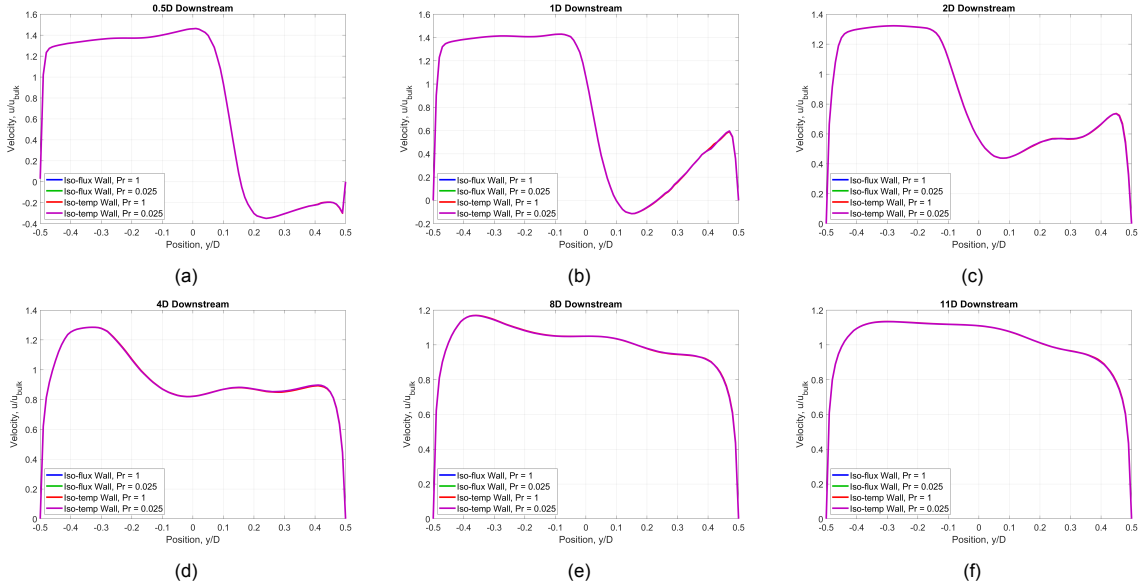

Figure A.6: Normalized streamwise velocity comparative plots

Quantitative profile comparison plots are also made for the time-averaged temperature fields of the first four passive scalars implemented in the UDNS calculation along with the normalized temperature fields of the four RANS simulations, at the 6 downstream locations. The temperature comparative plots are presented here. T1: Iso-temperature high Prandtl scalar, T2: Iso-temperature low Prandtl scalar, T3: Iso-flux high Prandtl scalar, T3: Iso-flux low Prandtl scalar.

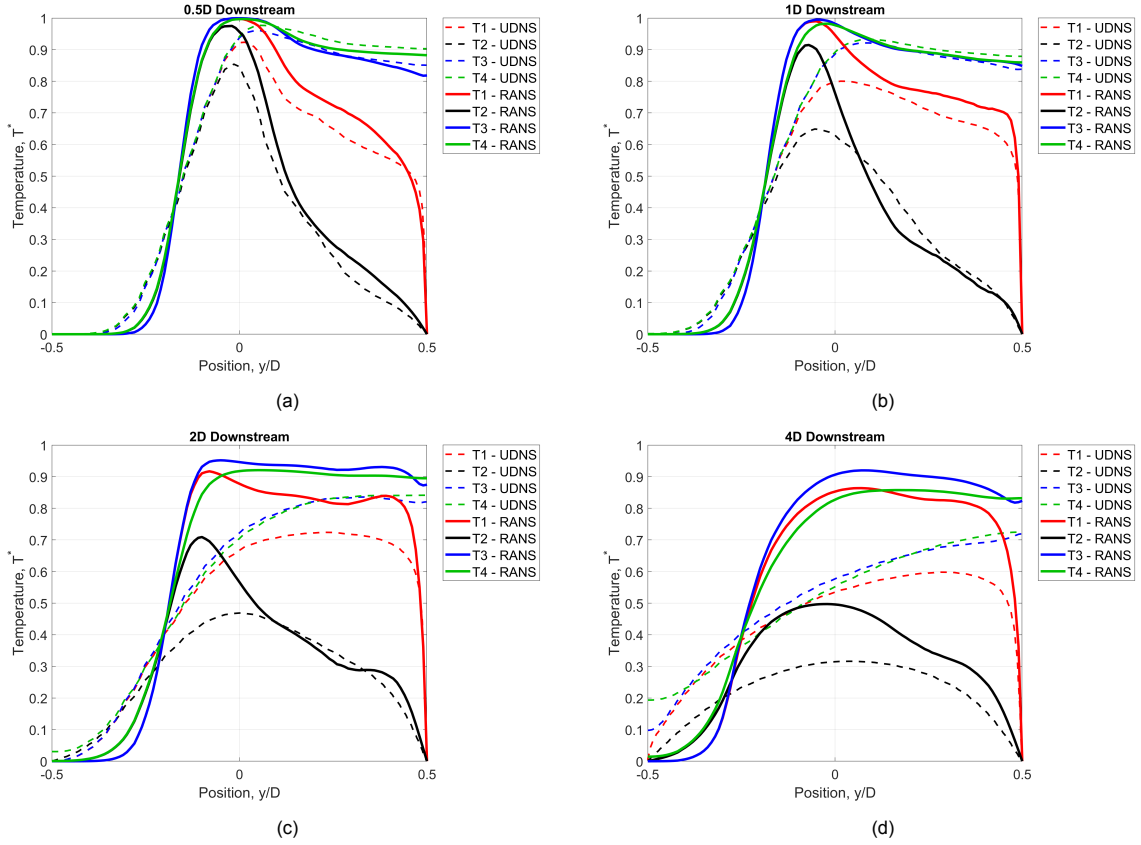

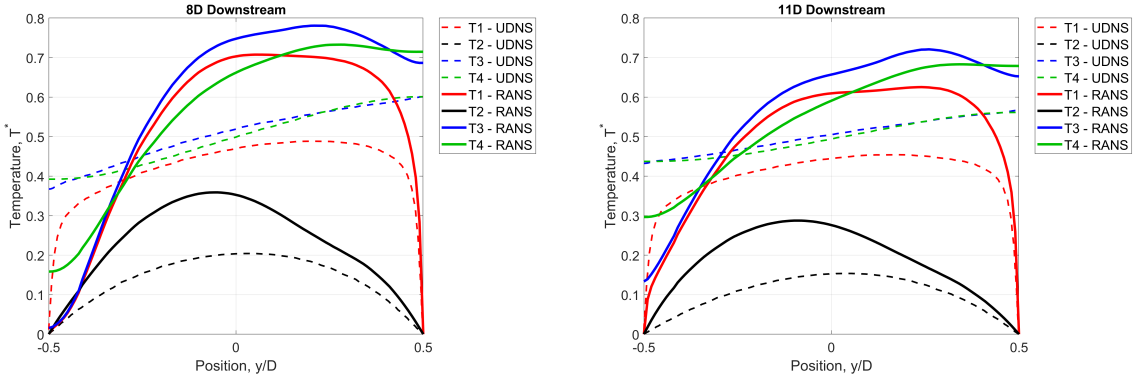

(e) (f)

Figure A.7: Normalized Temperature (T^*) comparative plots between UDNS and RANS

The profiles of the r.m.s. temperature fields of the first four scalars of the UDNS are also presented.

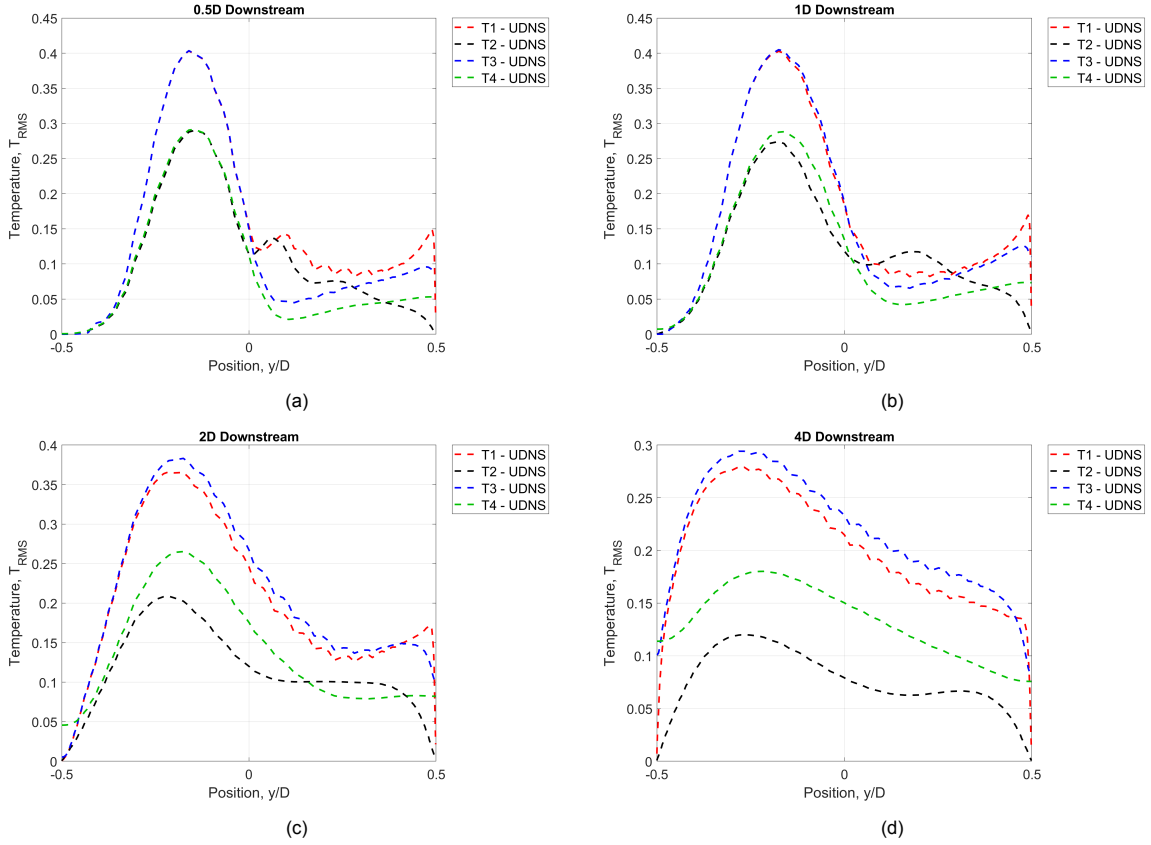

(a) (b)

(c) (d)

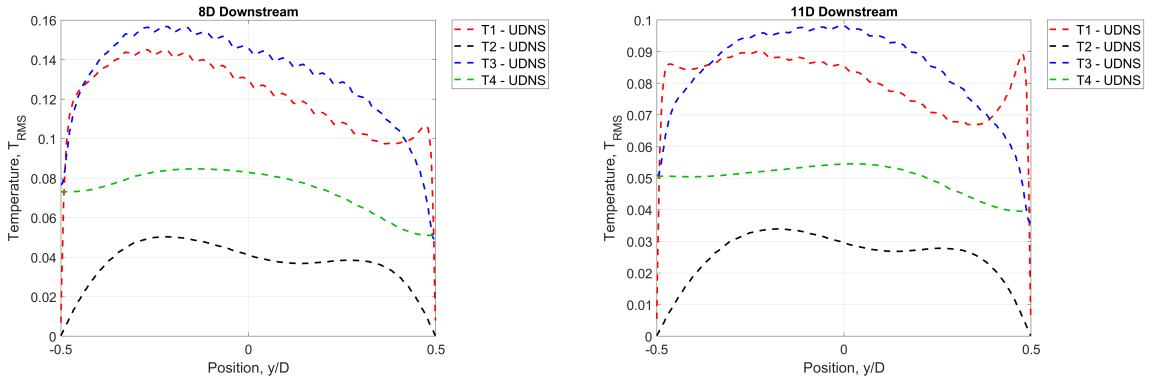

(e) (f)

Figure A.8: RMS Temperature comparative profiles of the UDNS

A.4. UDNS Contour Plots

The contour plots for the instantaneous, mean and r.m.s quantities of the velocity components and passive scalars that are not shown in Section 5.2 are presented below.

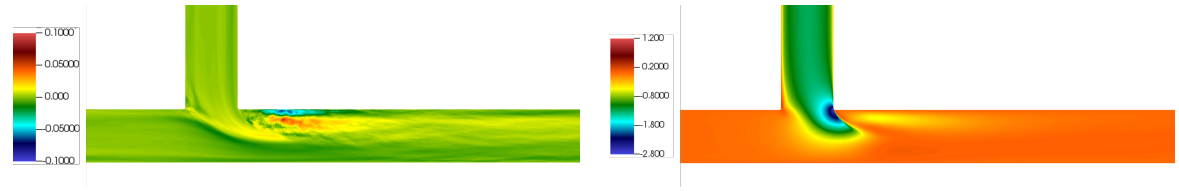

(a) u_x (b) u_y

Figure A.9: Mean velocity contours

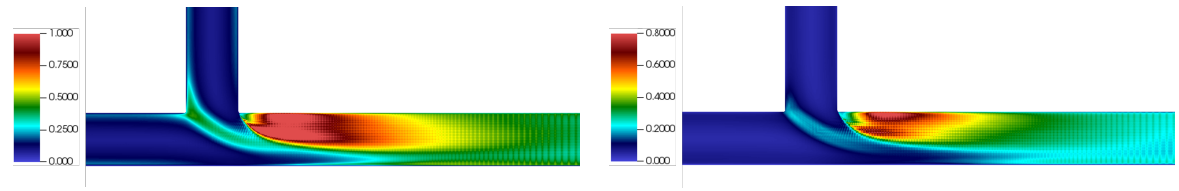

(a) Velocity magnitude (b) u_x

Figure A.10: RMS velocity contours

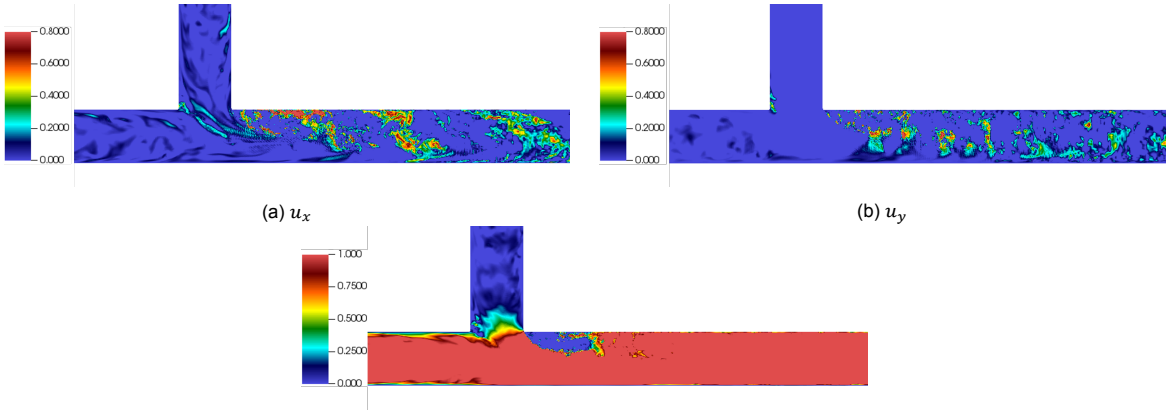

(a) u_x (b) u_y

(c) u_z

Figure A.11: Instantaneous velocity contours

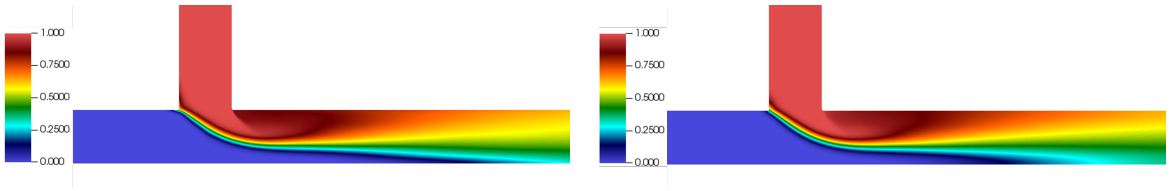

(a) High Prandtl number (b) Low Prandtl number

Figure A.12: Mean temperature contours for the iso-flux scalars

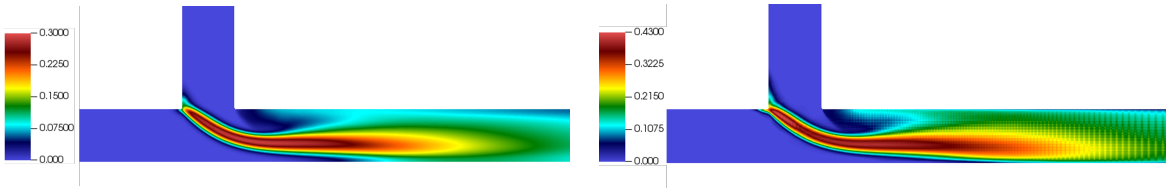

(a) High Prandtl number (b) Low Prandtl number

Figure A.13: RMS temperature contours for the iso-flux scalars

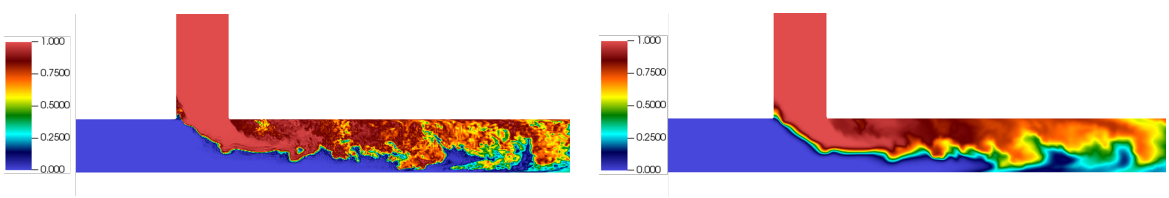

(a) High Prandtl number (b) Low Prandtl number

Figure A.14: Instantaneous temperature contours for the iso-flux scalars

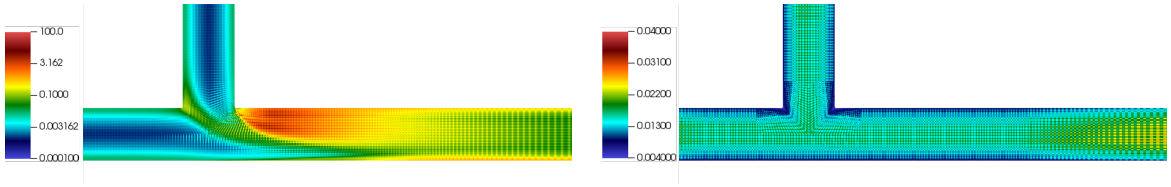

(a) Dissipation

(b) Local spatial discretization contours Δ

Figure A.15: Additional contours

Bibliography

[1] S.B. Pope. *Turbulent Flows*. Cambridge University Press, 2000. DOI: 10.1017/CBO9780511840531.

[2] B. Baldwin and H. Lomax. *Thin-layer approximation and algebraic model for separated turbulent flows*. 16th Aerospace Sciences Meeting, 1978. DOI: 10.2514/6.1978-257. URL: https://arc.aiaa.org/doi/abs/10.2514/6.1978-257.

[3] P. Spalart and S. Allmaras. *A one-equation turbulence model for aerodynamic flows*. 30th Aerospace Sciences Meeting and Exhibit, 1992. DOI: 10.2514/6.1992-439. URL: https://arc.aiaa.org/doi/abs/10.2514/6.1992-439.

[4] W.P Jones and B.E Launder. "The prediction of laminarization with a two-equation model of turbulence". In: *International Journal of Heat and Mass Transfer* 15.2 (1972), pp. 301–314. ISSN: 0017-9310. DOI: https://doi.org/10.1016/0017-9310(72)90076-2. URL: https://www.sciencedirect.com/science/article/pii/0017931072900762.

[5] David C. Wilcox. "Reassessment of the scale-determining equation for advanced turbulence models". In: *AIAA Journal* 26.11 (1988), pp. 1299–1310. DOI: 10.2514/3.10041. URL: https://doi.org/10.2514/3.10041.

[6] David C. Wilcox. "Formulation of the k-w Turbulence Model Revisited". In: *AIAA Journal* 46.11 (2008), pp. 2823–2838. DOI: 10.2514/1.36541. URL: https://doi.org/10.2514/1.36541.

[7] F. R. Menter. "Two-equation eddy-viscosity turbulence models for engineering applications". In: *AIAA Journal* 32.8 (1994), pp. 1598–1605. DOI: 10.2514/3.12149. eprint: https://doi.org/10.2514/3.12149. URL: https://doi.org/10.2514/3.12149.

[8] SIEMENS PLM Software. *STAR-CCM+ User's Guide v. 12.02*. 2017. URL: https://www.cd-adapco.com/products/starccm.

[9] F.S. Lien, W.L. Chen, and M.A. Leschziner. "Low-Reynolds-Number Eddy-Viscosity Modelling Based on Non-Linear Stress-Strain/Vorticity Relations". In: *Proc. 3rd Symp. On Engineering Turbulence Modelling and Measurements, Crete, Greece, May 27-29, 1996* (1996). URL: https://ci.nii.ac.jp/naid/10012300902/en/.

[10] T.J. Craft, B.E. Launder, and K. Suga. "Development and application of a cubic eddy-viscosity model of turbulence". In: *International Journal of Heat and Fluid Flow* 17.2 (1996), pp. 108–115. ISSN: 0142-727X. DOI: https://doi.org/10.1016/0142-727X(95)00079-6. URL: https://www.sciencedirect.com/science/article/pii/0142727X95000796.

[11] D. A. Johnson and L. S. King. "A mathematically simple turbulence closure model for attached and separated turbulent boundary layers". In: *AIAA Journal* 23.11 (1985), pp. 1684–1692. DOI: 10.2514/3.9152. URL: https://doi.org/10.2514/3.9152.

[12] S.T. Jayaraju, E.M.J. Komen, and E. Baglietto. "Suitability of wall-functions in Large Eddy Simulation for thermal fatigue in a T-junction". In: *Nuclear Engineering and Design* 240 (2010), pp. 2544–2554. ISSN: 0029-5493. URL: https://doi:10.1016/j.nucengdes.2010.05.026.

[13] B.L. Smith, J.H. Mahaffy, and K. Angele. "A CFD benchmarking exercise based on flow mixing in a T-junction". In: *Nuclear Engineering and Design* 264 (2013), pp. 80–88. ISSN: 0029-5493. URL: http://dx.doi.org/10.1016/j.nucengdes.2013.02.030.

[14] M. Aounallah et al. "RANS simulations of turbulent and thermal mixing in a T-junction". In: *MECHANIKA* 19(3) (2013), pp. 277–282. ISSN: 1392-1207. URL: http://dx.doi.org/10.5755/j01.mech.19.3.4663.

[15] A. Shams et al. *Synthesis Report of MOTHER Project*. Nuclear Research and Consultancy Group, Forsmark NPP, Vattenfall R & D.

[16] M. Georgiou and M. V. Papalexandris. “Direct numerical simulation of turbulent heat transfer in a T-junction”. In: *Journal of Fluid Mechanics* 845 (2018), pp. 581–614. DOI: 10.1017/jfm.2018.256.

[17] R.J.A. Howard and E. Serre. “Large-eddy simulation in a mixing tee junction: High-order turbulent statistics analysis”. In: *International Journal of Heat and Fluid Flow* 51 (2015), pp. 65–77. ISSN: 0142-727X. URL: http://dx.doi.org/10.1016/j.ijheatfluidflow.2014.11.009.

[18] H. Kamide et al. “Study on mixing behavior in a tee piping and numerical analyses for evaluation of thermal striping”. In: *Nuclear Engineering and Design - NUCL ENG DES* 239 (Jan. 2009), pp. 58–67. DOI: 10.1016/j.nucengdes.2008.09.005.

[19] A. De Santis and A. Shams. “Assessment of different URANS models for the prediction of the unsteady thermal mixing in a T-junction”. In: *Annals of Nuclear Energy* 121 (2018), pp. 501–512. ISSN: 0306-4549. URL: https://doi.org/10.1016/j.anucene.2018.08.002.

[20] A. Nakamura et al. “Benchmark Simulation of Temperature Fluctuation Using CFD for the Evaluation of the Thermal Load in a T-Junction Pipe”. In: *Proc. of the 7th Korea-Japan Symposium on Nuclear Thermal Hydraulics and Safety (NTHAS-7)*. Nov. 2010.

[21] C.H. Lin and Y.M. Ferng. “Investigating thermal mixing and reverse flow characteristics in a T-junction using CFD methodology”. In: *Applied Thermal Engineering* 102 (2016), pp. 733–741. ISSN: 1359-4311. DOI: https://doi.org/10.1016/j.applthermaleng.2016.03.124. URL: https://www.sciencedirect.com/science/article/pii/S135943111630432X.

[22] F. Aulery et al. “Numerical simulations of sodium mixing in a T-junction”. In: *Applied Thermal Engineering* 37 (2012), pp. 38–43. ISSN: 1359-4311. DOI: https://doi.org/10.1016/j.applthermaleng.2011.12.044. URL: https://www.sciencedirect.com/science/article/pii/S1359431111007411.

[23] S. Qian, S. Kanamaru, and N. Kasahara. “High-accuracy CFD prediction methods for fluid and structure temperature fluctuations at T-junction for thermal fatigue evaluation”. In: *Nuclear Engineering and Design* 288 (July 2015). DOI: 10.1016/j.nucengdes.2015.04.006.

[24] T. Frank et al. “Simulation of turbulent and thermal mixing in T-junctions using URANS and scale-resolving turbulence models in ANSYS CFX”. In: *Nuclear Engineering and Design* 240 (Sept. 2010), pp. 2313–2328. DOI: 10.1016/j.nucengdes.2009.11.008.

[25] A. Shams et al. “Synthesis of a CFD benchmarking exercise for a T-junction with wall”. In: *Nuclear Engineering and Design* 330 (2018), pp. 199–216. ISSN: 0029-5493. DOI: https://doi.org/10.1016/j.nucengdes.2018.01.049. URL: https://www.sciencedirect.com/science/article/pii/S0029549318300669.

[26] C. Walker et al. “Steady-state RANS-simulations of the mixing in a T-junction”. In: *Nuclear Engineering and Design* 240 (2010), pp. 2107–2115. ISSN: 0029-5493. URL: https://doi:10.1016/j.nucengdes.2010.05.056.

[27] M. Annalisa et al. “Toward the prediction of Temperature Fluctuations by means of Steady RANS for the Estimation of Thermal Fatigue”. In: *The 13th International Topical Meeting on Nuclear Reactor Thermal Hydraulics (NURETH-13)* (Oct. 2).

[28] R. Bergant et al. “DNS of Turbulent Heat Transfer in Channel Flow With Heat Conduction in the Solid Wall”. In: *Journal of Heat Transfer* 123 (Oct. 2001). DOI: 10.1115/1.1389060.

[29] C. Flageul et al. “DNS of turbulent channel flow with conjugate heat transfer: Effect of thermal boundary conditions on the second moments and budgets”. In: *International Journal of Heat and Fluid Flow* 55 (2015), pp. 34–44. ISSN: 0142-727X. DOI: https://doi.org/10.1016/j.ijheatfluidflow.2015.07.009. URL: https://www.sciencedirect.com/science/article/pii/S0142727X15000910.

[30] C. Flageul et al. “DNS of turbulent channel flow: can we imitate conjugate heat-transfer with a Robin boundary condition?” In: *8th international symposium of Turbulence Heat and Mass Transfer*. Sarajevo, Bosnia and Herzegovina, Sept. 2015. URL: https://hal.archives-ouvertes.fr/hal-01323794/file/thmt_flageul_long_final.pdf.

[31] P.F. Fischer, J.W. Lottes, and S.G. Kerkemeier. *Nek5000 web page*. 2008. URL: https://nek5000.mcs.anl.gov.

[32] P.F. Fischer. *Implementation considerations for the OIFS/characteristics approach to convection problems web page*. URL: https://www.mcs.anl.gov/~fischer/Nek5000/oifs.pdf.

[33] Linne Flow Centre - KTH Royal Institute of Technology Sweden. *Simulation Data, FLOW Database web page*. 2019. URL: https://www.flow.kth.se/flow-database/simulation-data-1.791810.

[34] E. Komen et al. “Quasi-DNS capabilities of OpenFOAM for different mesh types”. In: *Computers & Fluids* 96 (2014), pp. 87–104. ISSN: 0045-7930. DOI: https://doi.org/10.1016/j.compfluid.2014.02.013. URL: https://www.sciencedirect.com/science/article/pii/S0045793014000760.

[35] A.T. Patera. “A spectral element method for fluid dynamics: Laminar flow in a channel expansion”. In: *Journal of Computational Physics* 54.3 (1984), pp. 468–488. ISSN: 0021-9991. DOI: https://doi.org/10.1016/0021-9991(84)90128-1. URL: https://www.sciencedirect.com/science/article/pii/0021999184901281.

[36] A.G. Tomboulides, J.C.Y. Lee, and S.A. Orszag. “Numerical simulation of low Mach number reactive flows”. In: *Journal of Scientific Computing* 12.2 (1997), pp. 139–167. ISSN: 1573-7691. DOI: 10.1023/A:1025669715376. URL: https://doi.org/10.1023/A:1025669715376.

[37] Y. Maday, A.T. Patera, and E.M. Romquist. “An Operator-integration-factor splitting method for time-dependent problems: Application to incompressible fluid flow”. In: *Journal of Scientific Computing* 5.4 (1990), pp. 263–292. ISSN: 1573-7691. DOI: 10.1007/BF01063118. URL: https://doi.org/10.1007/BF01063118.